UNIVERSIDADE
BEIRA INTERIOR

Structural Design of a Bobsleigh Cowling using FEA

(Versão Final Após Defesa)

Rodrigo Miguel Carvalho Filipe

Dissertação para obtenção do Grau de Mestre em
Engenharia Aeronáutica
(Mestrado Integrado)

Orientador: Prof. Doutor Pedro Vieira Gamboa

Janeiro de 2024

Declaração de Integridade

Eu, Rodrigo Miguel Carvalho Filipe, que abaixo assino, estudante com o número de inscrição 41106 de/o Mestrado Integrado em Engenharia Aeronáutica da Faculdade de Engenharia, declaro ter desenvolvido o presente trabalho e elaborado o presente texto em total consonância com o **Código de Integridades da Universidade da Beira Interior**.

Mais concretamente afirmo não ter incorrido em qualquer das variedades de Fraude Académica, e que aqui declaro conhecer, que em particular atendi à exigida referenciação de frases, extratos, imagens e outras formas de trabalho intelectual, e assumindo assim na íntegra as responsabilidades da autoria.

Universidade da Beira Interior, Covilhã 15/1/2024

Assinado por: **Rodrigo Miguel Carvalho Filipe**
Num. de Identificação: 14603476
Data: 2024.01.16 09:21:16+00'00'

(assinatura conforme Cartão de Cidadão ou preferencialmente
assinatura digital no documento original se naquele mesmo formato)

Acknowledgements

First and foremost, I extend my heartfelt gratitude to my thesis supervisor, Professor Pedro Gamboa, whose unwavering guidance, and insightful discussions that proved instrumental throughout this journey. Your availability to meet and discuss, along with your dedicated mentorship, has shaped the course of this work in immeasurable ways.

I also wish to express my sincere gratitude to all the people who generously shared their time and knowledge with me over the course of my five years at UBI.

Lastly, my deepest thanks go to my parents and brother for their unwavering support throughout these years. Their encouragement and belief in my aspirations have been the cornerstone of this journey. Without them, none of this would have been possible.

Resumo

A massa e as frequências naturais de um trenó para a competição de Bobsleigh são fatores críticos no seu desenvolvimento. A capacidade que a estrutura apresenta de absorver vibrações, apresentada em estruturas com frequências naturais mais elevadas, e a capacidade de ajuste do centro de gravidade do trenó, obtido através da redução da massa total deste, têm um impacto positivo significativo no desempenho do bobsleigh. Para o desenvolvimento da estrutura da carenagem dos trenós para esta competição, são comumente utilizados materiais compósitos, escolhidos pela sua alta resistência específica e facilidade de fabricação. A utilização correta deste tipo de materiais compósitos permite a minimização da massa total, permitindo o ajuste do centro de gravidade e aumentando as frequências naturais da estrutura, melhorando, assim, o desempenho do bobsleigh.

Esta dissertação descreve o desenvolvimento da estrutura da carenagem de um trenó para a competição de Bobsleigh utilizando materiais compósitos, recorrendo a Análises de Elementos Finitos. A motivação para este trabalho reside no desejo da Federação Portuguesa de Desportos de Inverno de participar nos Jogos Olímpicos de Inverno de 2026 na categoria de Bobsleigh, sem ter de depender de trenós emprestados. Para o desenvolvimento desta dissertação, a estrutura foi baseada na geometria obtida através de análises de Dinâmica dos Fluidos Computacional (CFD) e foi dividida em duas partes: uma parte frontal e uma parte traseira. Esta pesquisa visa contribuir para o avanço da tecnologia utilizada no desporto de Bobsleigh e aumentar a competitividade de Portugal nos Jogos Olímpicos de Inverno.

O desenvolvimento desta dissertação começou pela investigação das cargas às quais as estruturas estão sujeitas. De acordo com essa investigação, as principais cargas são cargas de elevadas acelerações, resultantes das forças centrífugas durante as curvas a alta velocidade; cargas de impacto, nos casos em que os trenós colidem com as paredes da pista; cargas de impulsão, aplicadas pelos atletas durante a fase de partida no início da corrida; e vibrações, através da realização de análises modais, para avaliar a capacidade de absorção de vibrações das estruturas. Essas cargas foram importadas para o *Ansys*, onde a estrutura do trenó foi testada.

Em seguida, testou-se o impacto que diferentes materiais podem ter no desenvolvimento da estrutura do trenó. Com este objetivo, foram testadas cinco fibras de carbono diferentes, quatro materiais diferentes para núcleo do laminado, e quatro diferentes processos de fabrico numa geometria preliminar. Estes resultados foram, então, comparados, de acordo com critérios como a disponibilidade desses materiais e processos de fabrico, e resultados que podem afetar o desempenho do trenó: Massa Total da estrutura e Frequências Naturais. Os resultados desta pesquisa mostraram que a escolha do material é crucial para o desenvolvimento estrutural e permitiram a seleção das três combinações de materiais mais adequadas ao caso em estudo.

As três combinações de materiais escolhidas na pesquisa anterior foram, de seguida, testadas na geometria final do trenó e comparadas com os mesmos critérios de disponibilidade e resultados que podem afetar o seu desempenho. Ao analisar os resultados obtidos com a geometria final, ficou claro que esta apresentava características estruturais diferentes quando comparada com a preliminar. Com os resultados destas análises com a geometria final, foi possível obter uma estrutura final utilizando uma combinação de fibra de carbono M35J, núcleo de favo de mel de aramida e fabrico por infusão. Para validar esses resultados, foi realizada uma análise de independência da malha. Com esta, foi possível concluir que a maioria dos resultados converge. No entanto, para alguns resultados, tal não acontece, pois não há convergência clara de resultados, sendo o tamanho e o refinamento da malha limitados pelo poder computacional disponível.

Tendo em mente todas as conclusões anteriores, foi possível desenvolver uma estrutura final com uma massa de 12.3 kg, capaz de suportar todas as cargas a que será submetida. Esta estrutura é apresentada em detalhes, sendo apresentados os diferentes laminados usados nas diferentes partes, estando ajustada à geometria atual do trenó, requerendo uma investigação adicional em caso de mudanças na geometria externa deste, já que diferentes geometrias resultam em características estruturais diferentes.

Palavras-chave

Bobsleigh, Materiais Compósitos, Análises de Elementos Finitos

Abstract

The total mass and natural frequencies are critical factors in bobsleigh design. The ability of the structure to absorb vibrations, achieved in structures with higher natural frequencies, and adjust the bobsleigh's center of gravity, achieved through reduced total mass, significantly impacts bobsleigh performance. Composite materials, chosen for their high specific strength and ease of manufacturing, are commonly used in the cowling structure of bobsleighs. Correct utilization of these composite materials can minimize total mass, enhancing center of gravity adjustment, and increase natural frequencies, thereby improving bobsleigh performance.

This dissertation describes the development of a cowling structure of a bobsleigh with composite materials, using Finite Element Analyses. The motivation for this work lies in the the Portuguese Winter Sports Federation's aspiration to participate in the 2026 Winter Olympics in the Bobsleigh event, without relying on borrowed bobsleighs. For the development of this dissertation, the structure was based on the outline geometry obtained through CFD analysis and design, divided into two parts: a front part and a rear part. This research endeavors to contribute to the advancement of bobsleigh technology and enhance Portugal's competitiveness in the Winter Olympics.

The development of this dissertation started by investigating the loading conditions to which the structures will be subject to. According to this investigation, the major loading conditions are high accelerations, as a result of the centrifugal forces during high-speed cornering; impact loads, for the cases where the bobsleighs hit the walls of the track; pushing loads, for loads applied by the athletes during the push-off phase in the beginning of the race; and modal analysis, to assess the vibration absorption capacity of the structures. This loads were imported into *Ansys*, where the bobsleigh structure was tested.

Subsequently, the dissertation continued by testing the impact different materials might have on the structure development. With this in mind, five different carbon fibers, four different core materials, and four different manufacturing processes were tested on a preliminary bobsleigh geometry. These results were then compared, considering factors such as the accessibility to these materials and manufacturing processes, and results that may impact the performance: Total Mass and Natural Frequencies. The results that arose from this research proved the material choice is critical for the structural development and allowed us to select the three material combinations most suited to the case at hand.

The three material combinations chosen in the previous research were then tested in the final bobsleigh geometry, and compared with the same criteria of accessibility and results that may affect the performance of the bobsleigh. By analyzing this final geometry, it was clear that it presented different structural characteristics when compared to the preliminary one. These analyses on the final geometry yielded a final structure using a

combination of M35J carbon fiber, Aramid Honeycomb core, and Infusion manufacturing. To validate these results, an analysis of mesh independence was made. With it, it was possible to conclude that there is convergence of most results. However, for some results, that cannot be said, as there is no clear convergence, being the mesh size and refinement limited by the available computational power.

Bearing all the previous conclusions in mind, it was possible to develop a final structure with a mass of 12.3 kg, capable of withstanding all the loads it will be subject to. This structure is presented in detail, with the different laminates used in the different parts and is adjusted just to the current geometry of the bobsleigh, requiring further investigation in case of changes made to the outer geometry of the bobsleigh, as different geometries yield different structural characteristics.

Keywords

Bobsleigh, Composite Materials, Design,Finite Element Analysis

Contents

List of Figures

List of Tables

Acronyms and Abbreviations

ACP	Ansys Composite PrepPost
CFD	Computational Fluid Dynamics
CFRPs	Carbon Fiber Reinforced Polymers
cog	center of gravity
FDI-Portugal	Portuguese Winter Sports Federation
FEA	Finite Element Analysis
IBSF	International Bobsleigh & Skeleton Federation
UBI	Universidade da Beira Interior

Nomenclature

E_1	Young's Modulus in direction 1
E_2	Young's Modulus in direction 2
E_3	Young's Modulus in direction 3
G_{12}	Shear Modulus in plane 1 2
G_{23}	Shear Modulus in plane 2 3
G_{31}	Shear Modulus in plane 3 1
N	Nominal value
ND	Non-dimensional value
t	Ply Layer Thickness
W	Criterion Weight
ρ	Density
ν_1	Poisson's Ratio in direction 1
ν_2	Poisson's Ratio in direction 2
ν_3	Poisson's Ratio in direction 3
$\sigma_{1_{tens}}$	Tensile Yield Strength in direction 1
$\sigma_{2_{tens}}$	Tensile Yield Strength in direction 2
$\sigma_{3_{tens}}$	Tensile Yield Strength in direction 3
$\sigma_{1_{comp}}$	Compressive Yield Strength in direction 1
$\sigma_{2_{comp}}$	Compressive Yield Strength in direction 2
$\sigma_{3_{comp}}$	Compressive Yield Strength in direction 3
σ_{12}	Shear Strength in direction plane 1 2
σ_{23}	Shear Strength in direction plane 2 3
σ_{31}	Shear Strength in direction plane 3 1

Chapter 1

Introduction

1.1 The Sport of Bobsleigh

Bobsleigh is a winter sport where a crew composed of 1, 2 or 4 athletes makes timed runs driving a gravity-powered sled down through a narrow, twisting, banked, iced track [1]. The origins of this sport can be traced back to the resort town of St. Moritz in Switzerland where, in the late 1800s, British tourists were using wooden sleds on the road to get down the hill [2]. Eventually, first racing sleds made of wood were replaced by steel sleds that came to be known as bobsleds, so named because of the way crews bobbed back and forth to increase their speed on the straightaways [3]. The first bobsleigh course was formed in 1870 to ensure the safety of pedestrians on the road, and in 1884 the first formal bobsleigh competition was held [2].

Today, bobsleigh is seen as the Formula 1 of winter Olympic sports and is divided into four competition classes: women's monobob, 2-woman, 2-man, and 4-man. The competition has two main phases: the push-off phase, i.e., the first 50 m where the athletes push the sled to about 40 km/h and then jump inside; and the drive, where the pilot navigates the sled down the remainder of the ice-covered track [2]. During the latter phase, bobsleigh speeds can reach up to 135 km/h and experience accelerations that can exceed 5 g [4, 5]. The speeds and accelerations experienced on a run depend on the track layout, which varies from one track to another. The track resembles a large ice chute, similar to a waterslide covered in ice [2].

1.1.1 The Sled

As explained before, throughout the years, the design and construction of bobsleighs have evolved in search of faster and more competitive sleds. Nowadays, this design is strictly regulated and is of interest to scientific and commercial institutions, such as *NASA* and some *NASCAR* teams, who have been closely involved in bobsleigh development for the USA Olympic teams. Another example includes the UK teams that have been relying on Formula 1 teams and aerospace companies, like *British Aerospace*, to develop their bobsleighs [6].

One example of a general shape of a bobsleigh can be seen in Figure 1.1. Just like in the example shown, each sled has a total of four highly polished runners, which are four steel blades under the sled, to create a low friction contact with the ice that are the only part of

the sled that makes contact with the ice surface during normal sliding conditions. These runners are then connected to the sled's structure, which can be divided into two parts: the frame and the cowling. On the one hand, the frame includes all the internal structures, such as the steering mechanism and the runners' support, and is made of steel as mandated by international rules. On the other hand, the cowling is the aerodynamic hull of the sled made of carbon fiber or glass fiber reinforced polymer [2, 7].

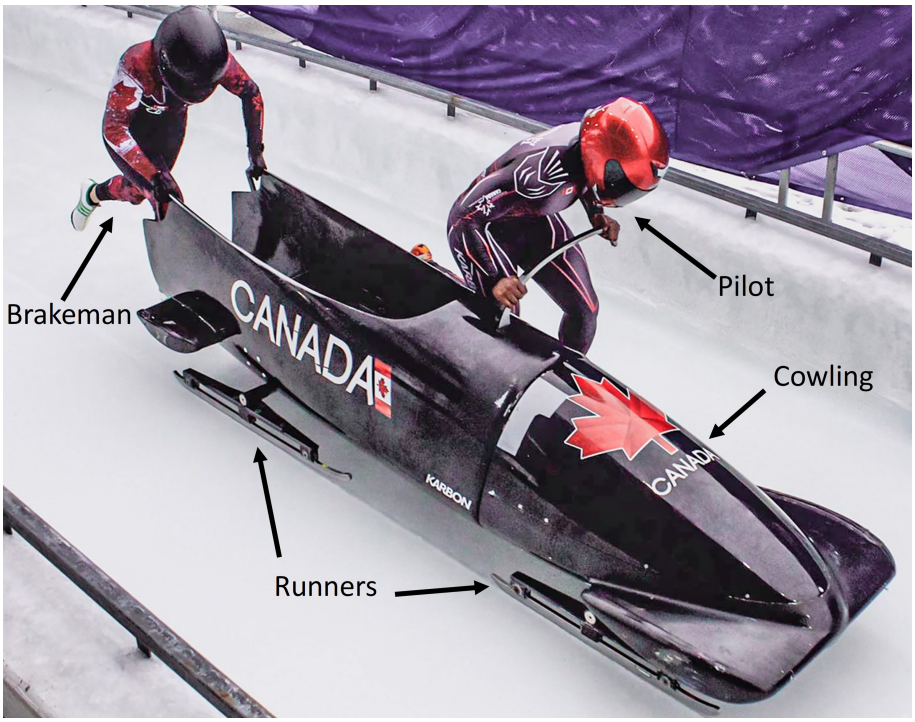

Figure 1.1: Photograph of a 2-woman sled with the pilot and the brakeman taken during a training session with Canada's National Team, adapted from [8].

Focusing solely on the cowling, it is divided into two parts, the front, and the rear, allowing the front part to rotate when entering and exiting corners. Furthermore, as can be seen in Figure 1.1, there are two front bumpers and two rear bumpers. These are responsible for preventing damage that may come from the sidewalls of the track while driving and may have some aerodynamic function [9, 4]. Furthermore, in the cowling, we can also find two push handles at the very end of the cowling and side push bars, used by the athletes on the push-off phase [4].

Finally, two of the most important rules every sled has to obey are the minimum and maximum mass rules. For these rules, the minimum mass is measured by weighing the sled, including the runners, but without the crew, whereas the maximum mass is measured including the sled, the runners, and the crew. For these, the mass limits are dependent on the race category and may be achieved with the help of ballast weight as shown in Table 1.1 [4].

Table 1.1: Mass limits for the different bobsleigh categories [4].

Category	Minimum Mass [kg]	Maximum Mass [kg]
2-man bobsleigh	170	390
4-man bobsleigh	210	630
women's monobob	163	248
2-woman bobsleigh	170	330

1.1.2 Portuguese History in Bobsleigh

When it comes to winter sports, Portugal has a relatively brief history, with only one appearance in an Olympic bobsleigh competition to its name. To do so, Portugal took three teams to the Calgary 1988 Olympics, with a total of 5 athletes, to take part in the two-man bobsleigh with two teams, and in the four-man bobsleigh competitions with one team [10]. Due to the small investment in winter sports, Portugal had to rely on borrowed bobsleighs to be able to compete. In the four-man competition, Portugal finished in the 25^{th} place out of 26 teams, whereas in the two-man competition, the only team to complete all the runs did so by finishing 34^{th} out of 41 teams[11, 12].

In an attempt to change the history in Winter Sports, the Portuguese Winter Sports Federation (*Federação de Desportos de Inverno de Portugal*, FDI-Portugal) set the goal of participating in the 2026 Winter Olympics in the Bobsleigh's event. In order to avoid having to to rely on borrowed bobsleighs, like in the past, FDI-Portugal set the goal to develop and produce the first ever bobsleigh completely developed in Portugal. With this in mind, the current thesis is part of the development of the said bobsleigh, and FDI-Portugal served as the first and main motivator to pursue this work of creating a competitive bobsleigh.

1.2 Motivation

Bobsleigh is a thrilling winter sport known for its speed and victories by the narrowest of margins. At the 1998 Olympics, the bronze medal was shared by the British and French teams, who finished within 0.01 seconds of each other (just 0.04% of the total time) over a six-kilometer distance. These razor-thin margins create intense pressure on teams to innovate and develop superior design solutions in order to gain a competitive edge, doing research in a wide range of areas [6].

Like in most sports, research in bobsleigh is generally undertaken to gain an advantage over competitors, resulting in most of the work being secretive. For this reason, most work developed goes unpublished [2]. Despite this, due to some research being developed in conjunction with universities, it is still possible to find work made in different areas.

Throughout the years, plenty of research has been made on aerodynamic performance, both through wind tunnel testing and Computational Fluid Dynamics (CFD) modeling, focusing on the reduction of drag, in an attempt to increase the bobsleigh's top speed. To

do so, there has been work done exploring the advantages of different cowling geometries [13], rearrangement of the crew positions and internal padding [14, 6], optimization of bumper shapes [9], and by studying the influence of the gap between the nose and rear cowling of a two-man bobsleigh [15].

Another way teams have been trying to reduce speed losses is by lowering friction coefficients on the runners. To achieve that, there is work focused on understanding the variation of ice friction coefficient at different temperature and pressure conditions [16, 17, 18, 19]. The results from these analyses are then used in research carried out to optimize the shape of runners [7, 2, 20].

Despite being proven that structural parameters can have an influence on the overall performance of the bobsleigh [1] as shown in Chapter 2, low to no research done in this area has been published. This lack of publicly available research led to the interest in the development of the cowling structure of a bobsleigh.

1.3 Objectives

The main objective of this thesis is to develop and the cowling structure of a bobsleigh with characteristics that would be able to create a competitive bobsleigh. To achieve this objective we need to complete several subtasks:

- Develop a database of materials, based on what is used in this sport, and what is used in similar sports;
- Develop a structure based on the outline geometry obtained through CFD analysis by Vasconcelos [21];
- Implement the geometry, the boundary conditions, and the different loads acting on the structure in a finite element analysis (FEA) software;
- Optimize the structure in order to achieve the one that is most suited to the current application, but is still able to withstand every load case without failure and without deformations that could lead to increased drag.

1.4 Thesis Outline

The current thesis consists of five chapters, including the current one, and the main topics in these are:

- Chapter 1 presents the motivation to the development of this thesis and the main objectives;

- Chapter 2 covers the literature review, which includes a presentation of similar work made in this area;
- Chapter 3 presents the structure of the sled and the different materials used in the development of the cowling, including the creation of a database of materials and their mechanical properties. Furthermore, in this chapter the different load conditions are presented, including the boundary conditions to be used in the FEA;
- Chapter 4 presents the obtained results, including the structure resulting from the design process;
- Chapter 5 includes the final conclusions and possible future work.

Chapter 2

Literature Review

This chapter provides an overview of related works and introduces key concepts for this thesis. A presentation of the loads the bobsleigh might face is held in the first place, followed by a discussion of similar works, including some terms and definitions associated with structural design and finite element analysis. Lastly, there is a presentation of materials that could be used in the development of the structure and how they could benefit the performance.

2.1 Related Work

Regarding the loads that act on the bobsleigh's structure, it is crucial to bear in mind that there is not extensive research conducted specifically to assess them. Instead, they are generally a byproduct of research conducted to gain a deeper understanding of other phenomena. The results from these analyses can be divided into different categories: accelerations that the structure will face throughout the race, forces during the push-off phase, and vibrations of the structure.

Concerning the accelerations that the bobsleigh might encounter, Schleinitz et al. [22], to develop a model for both longitudinal and lateral friction, created a bobspecific one-track model and a friction model to describe and simulate its vehicle dynamics. To do so, they started by measuring the vertical (z) and lateral (y) accelerations experienced by the vehicle on the Königssee track, as depicted in Figure 2.1. With these results, it was possible to observe maximum accelerations of 4.10 g and 1.13 g in the vertical and lateral directions, respectively.

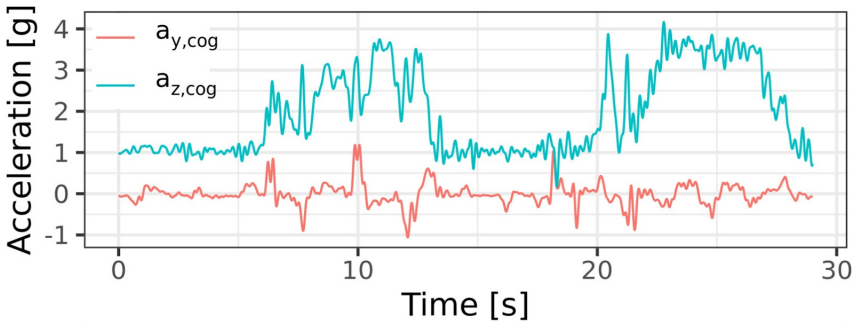

Figure 2.1: Vertical and lateral accelerations acting on the center of gravity as measured during a run on the track in Königssee [22].

Using the one-track and friction models developed, Schleinitz et al. [22] simulated runs down the Königssee track and calculated the lateral forces and vertical accelerations acting on the bobsleigh's center of gravity, as illustrated in Figures 2.2 and 2.3. With these measurements, it was possible to obtain a maximum lateral force of 5750 N, when the bobsleigh hits a wall of the track. Regarding vertical accelerations, there were measurements of up to 5.00 g.

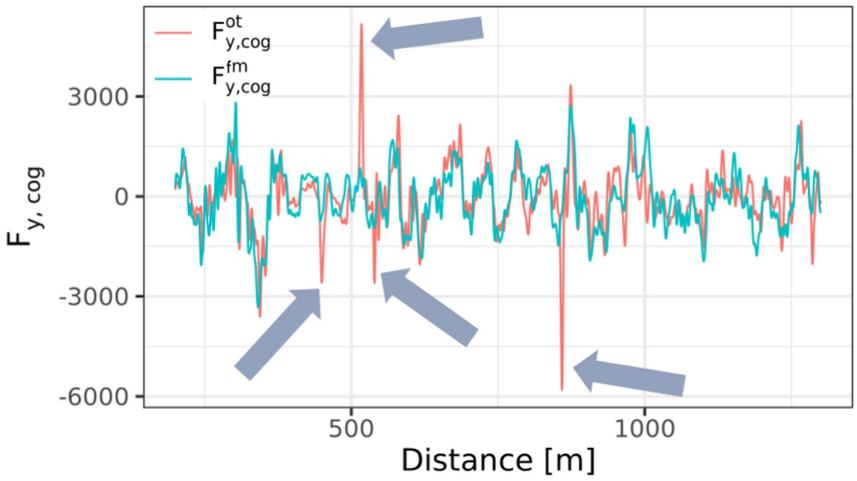

Figure 2.2: Lateral forces acting on the center of gravity using the one-track model ($F^{ot}_{y,cog}$) and the friction model ($F^{fm}_{y,cog}$) measured in the Königssee track. The arrows indicate places where the bobsled hit a wall [22].

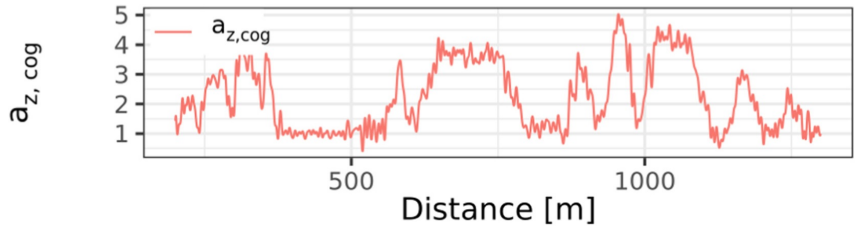

Figure 2.3: Vertical acceleration measured using the one-track model in the Königssee track [22].

Braghin et al. [23] focused on the development of a numerical model of a bobsleigh driver that aims at reproducing the driving behavior of real-world cup drivers and is basically made up of two steps: the identification of the trajectory that allows minimizing run time and the determination of the driver's inputs to exactly follow that trajectory. To do so, it was necessary to record the driver's inputs and the resulting trajectory on the Cesana Pariol Olympic track. As a result of these recordings, in Figure 2.4 the vertical acceleration of the rear frame of the bobsleigh measured along the vertical onboard axis versus the traveled distance is depicted. In this Figure, it can be seen that values of accelerations of up to 4.30 g were registered during the run.

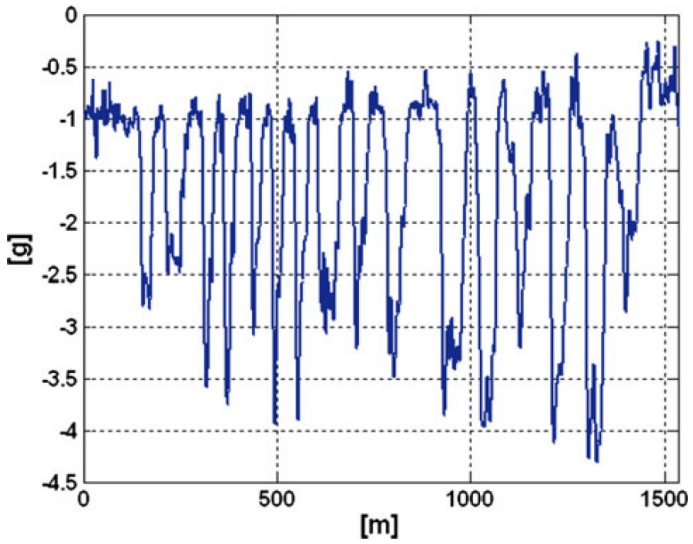

Figure 2.4: Experimental results: vertical acceleration of the rear frame of the bobsleigh (on-board reference) along Cesana Pariol Olympic track [23].

With regards to bobsleigh dynamics, Braghin et al. [24] presented the results of an experimental campaign carried out at the Cesana Pariol Olympic track with an instrumented two-man bobsleigh. This experimental research was carried out in order to objectively evaluate its performance and to set up a numerical model suitable for structural optimization purposes. During the tests, the bobsleigh was instrumented with an inertial gyroscopic platform to measure the vehicle dynamics, one optical sensor to measure the bobsleigh speed and sideslip angle, and one potentiometer to measure the steering angle imposed by the driver.

With this setup, the researchers managed to successfully measure the accelerations acting on the structure of the bobsleigh during a run along three axes: the x-axis is directed along the direction of motion, the y-axis is directed towards the left of the bobsleigh and the z-axis is upward-directed. In order to verify the reliability of the performed measurements, the accelerations measured have been respectively compared with the sum of the vertical, lateral, and longitudinal contact forces divided by the mass of the bobsleigh. As shown in Figures 2.5 through 2.7, they measured values of acceleration of up to 2.25 m/s^2 in the x direction, 8.19 m/s^2 in the y direction and 37 m/s^2 in the z direction. Comparison between forces (dashed lines) and acceleration (solid lines) measurements are reported in Figures 2.5, 2.6 and 2.7, respectively for x, y, and z directions [24].

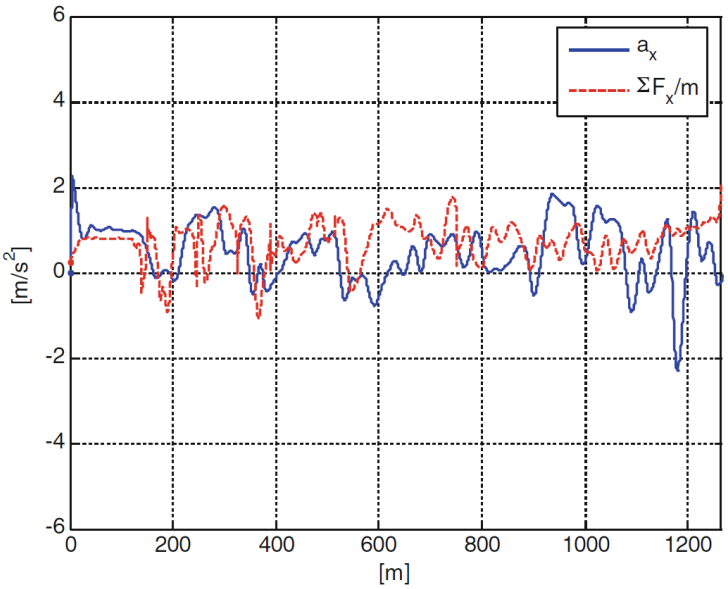

Figure 2.5: Comparison of the longitudinal equilibrium of a two-man bobsleigh for a run on the Cesana Pariol Olympic track [24].

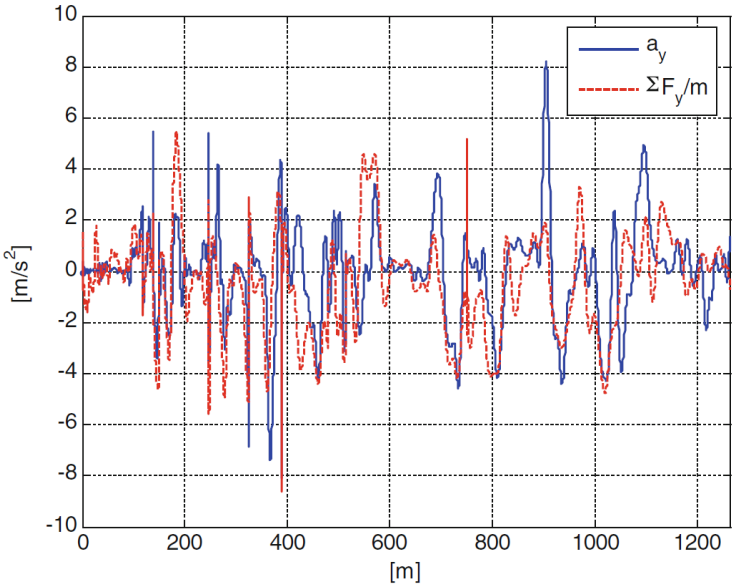

Figure 2.6: Comparison of the lateral equilibrium of a two-man bobsleigh for a run on the Cesana Pariol Olympic track [24].

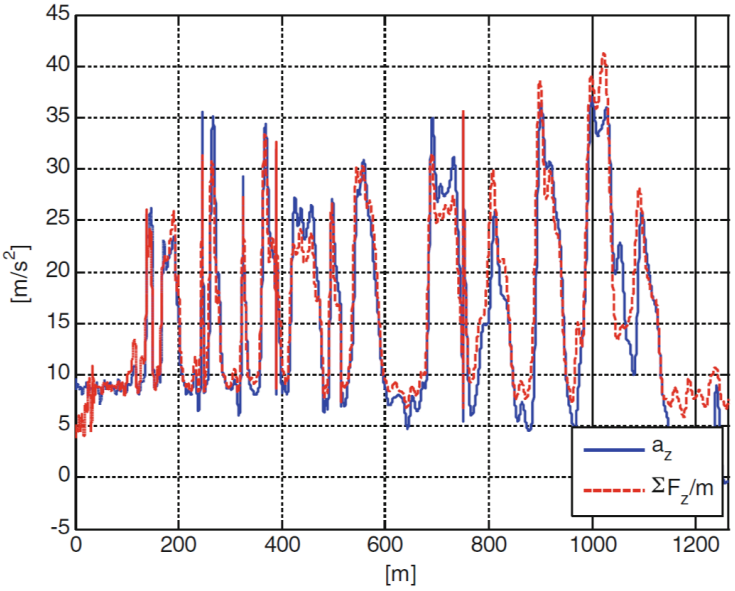

Figure 2.7: Comparison of the vertical equilibrium of a two-man bobsleigh for a run on the Cesana Pariol Olympic track [24].

Regarding the static loads, another important load to investigate is the load from the push-off phase, applied on the push handles and the push bars. As such, Lee et al. [25] developed a force measurement system to analyze the forces exerted by members of a two-person bobsled crew in two directions: the y-direction, directed along the direction of motion, and the vertical z-direction, upward-directed. The developed system comprised eight load cells, an encoder, four cameras, and a data acquisition device and was installed on a test sled. Two load cells were installed in each of the brakeman's push handles and the driver's side push bar and two load cells were located on each of the right and left ends of the push bar. The resulting loads applied on the driver's push bar are depicted in Figure 2.8, whereas the resulting loads applied on the brakeman's push handles are shown in Figure 2.9. During the push-off phase, there were recordings of loads of up to 860 N in the y direction and 800 N in the z direction for the driver and 2600 N in the y direction and -500 N in the z direction for the brakeman.

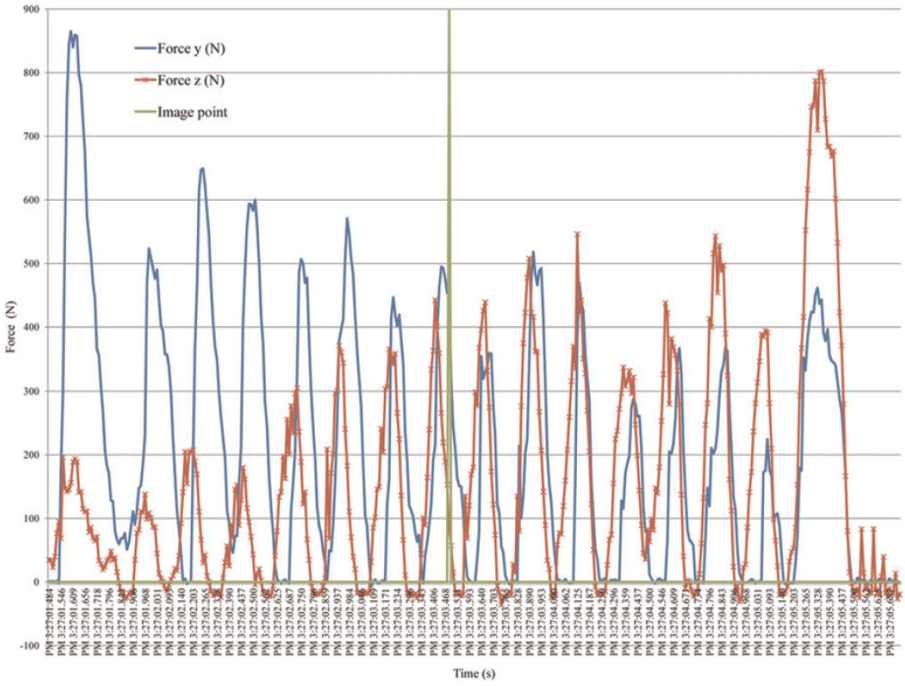

Figure 2.8: Driver's force data in y- and z-directions applied on the side push bar during the push-off phase [25].

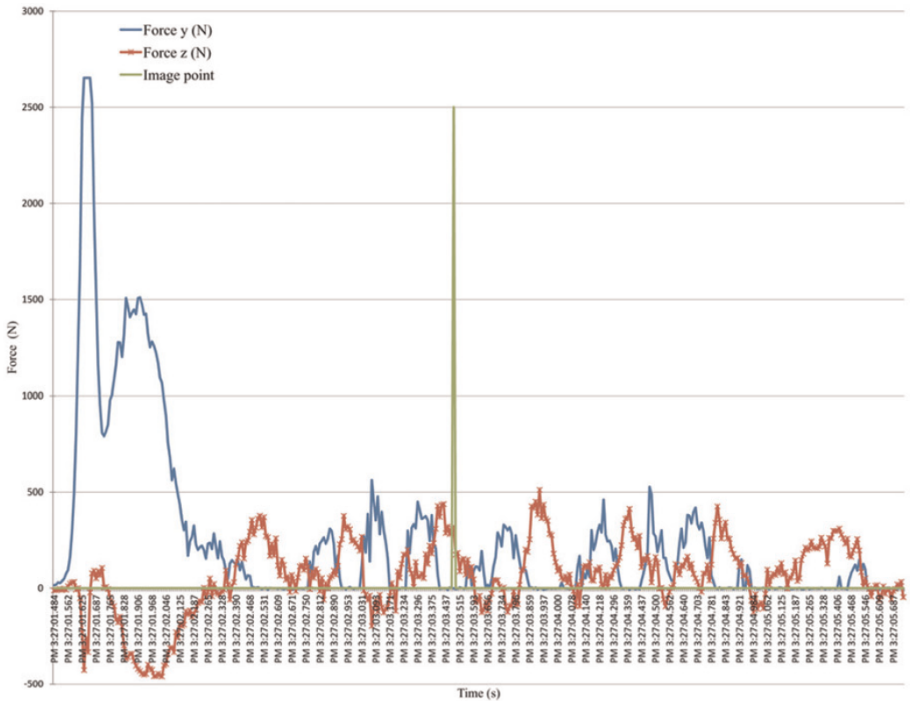

Figure 2.9: Brakeman's force data in y- and z-directions applied on the push handles during the push-off phase [25].

More recently, in an attempt to better understand how the push start affects the race and to be able to improve team performance, Onasch et al. [26] developed the instrumentation for a 4-man bobsled that allowed for measuring the propulsive forces of each athlete

during the bobsleigh push start. In a 4-man bobsleigh, considering there are 4 athletes, there are also 4 pushing places. These 4 places are: one push bar for the pilot, one push bar on the right for a second athlete, one push bar on the left for a third athlete and the push handles for the brakeman. While the pilot push bar and brakeman's push handles are equal to those in 2-man bobsleighs, the push bars for the second and third athletes are not present in a 2-man bobsleigh. However, the loads applied in them should be comparable to those on the pilot push-bar. The propulsive forces applied by each of the athletes are represented in Figure 2.10.

Analyzing the results presented in Figure 2.10, it is possible to see that the loads applied to push bars achieve a maximum of around -440 N regarding the vertical loads and a maximum of 800 N in horizontal load. Regarding the loads applied on the push handles, the loads on the vertical direction achieve values of up to -700 N, while on the horizontal direction achieve values of up to 565 N [26].

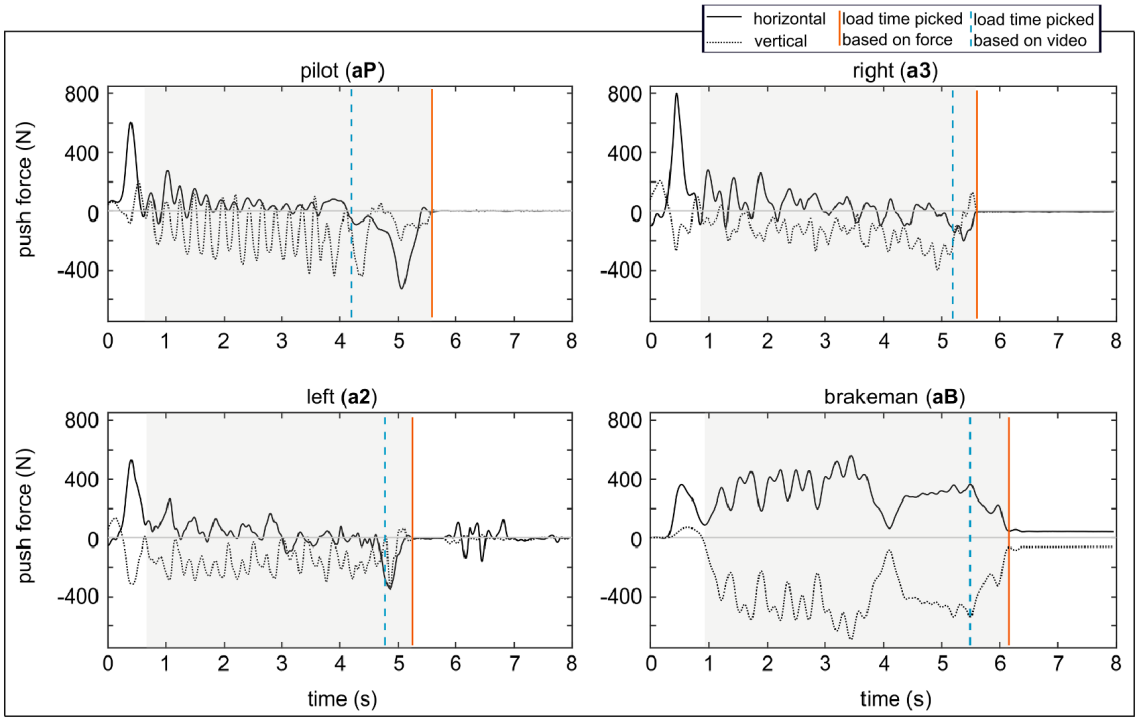

Figure 2.10: Horizontal and Vertical loads applied during the push-off phase in a 4-man bobsleigh, adapted from [26].

Despite so far only having focused on the static loads acting on the bobsleigh's structure, important loads come from dynamic loading. Dabnichki [27], in an attempt to propose ergonomic modifications to improve performance, from vibration measurements taken on running sleds, found that the predominant vibrations are up to 15 Hz. As a result of the vibrations, the researcher suggests the use of appropriate materials to improve the overall comfort of the crew, as active dampening is not permitted.

On the other hand, Лубяко et al., to better understand the origin of some injuries, re-

ported that on the Sanki track, vibration frequencies on bobsleighs with top speeds of 111.32 km/h reach values up to 23.72 Hz with vertical accelerations up to 7.32 g and lateral accelerations of up to 2.13 g. The vibrations are a result of irregularities and shocks on the track and, at a speed v, can be estimated from the following equation [28]:

$$f = 0.76v - 16.78\,[\text{Hz}], \quad R^2 = 0.78 \quad (2.1)$$

Concerning the development of the structure of bobsleighs, throughout the years, most of it has been made based on feedback from athletes. With this in mind, Sabbioni et al. developed a model for a simulator, as a tool to provide guidelines for the designers. This model was then validated by comparison with experimental data on the Cesana-Pariol track. On this model, the variation of run time with a variation of center of gravity height and longitudinal position was tested, as shown in Figures 2.11 and 2.12 [3].

As can be easily proved, increasing the center of gravity height increases the moment of inertia of the bobsleigh around the rotation axis. Higher moments of inertia, require higher tangential forces (and dissipation) in order to change the bobsleigh roll angle during transitions at the beginning and at the end of curves. These changes result in lower speeds through the turns, resulting in worse final times, as seen in Figure 2.11. Additionally, an increase in center of gravity height may also affect roll-over risk [3].

In Figure 2.12, it is shown that the most rear positions resulted in faster runs through this track. However, no direct conclusion can be made from this figure. In fact, changing the longitudinal position of the center of gravity mostly influences the distribution of normal loads between the front and rear axle optimizing understeer/oversteer response. As a result, the optimal value of this parameter was found to depend on the mean slope of the track. Furthermore, this response of understeer/oversteer can also depend on the driver and their type of runs [3].

Both obtained results accentuate the importance of achieving the lowest structure weight possible, since the minimum required bobsleigh's mass can be achieved through ballast weight. Thus, the position of the center of gravity can be adjusted, allowing for the best performance, even in tracks that require completely different center of gravity positions.

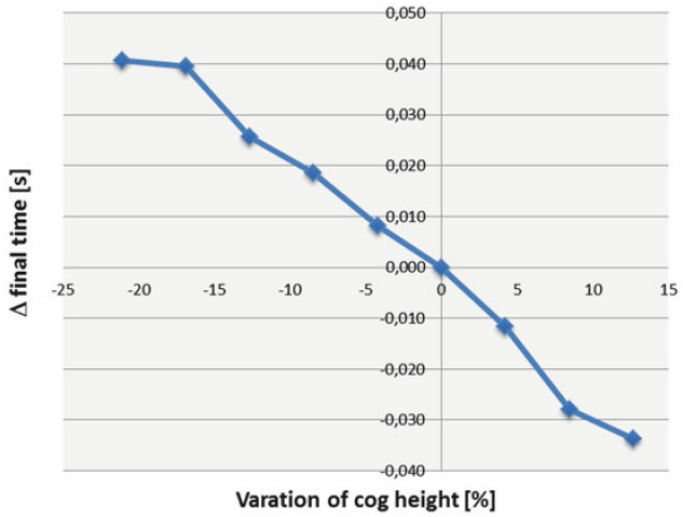

Figure 2.11: Variation of estimated final time with the change of center of gravity (cog) height with respect to nominal configuration in the Cesana-Pariol track, adapted from [3].

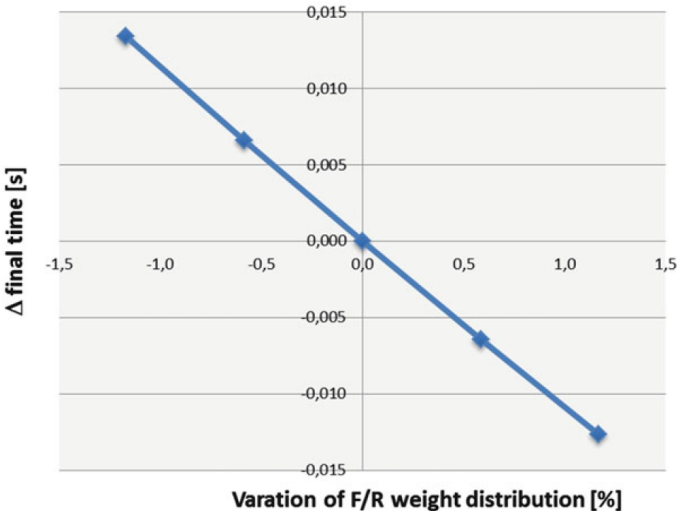

Figure 2.12: Variation of the estimated final time with the change of forward/rear (F/R) weight distribution with respect to nominal configuration in the Cesana-Pariol track, adapted from [3].

As seen in the graphics in Figures 2.1 through 2.7 of accelerations on different tracks, each track has its distinctive signature in terms of dynamic interactions between sleds and track as a result of different turns' layouts. Dabnichki collected dynamic data on different tracks and recorded dynamic accelerations of up to 10 g. Using this result, with the help of finite element analysis, Dabnichki simulated the dynamic response of the structure under these high dynamic loads, as illustrated in Figures 2.13 and 2.14. Despite presenting the results of the simulation, the boundary conditions used are unknown, making it hard to replicate [6].

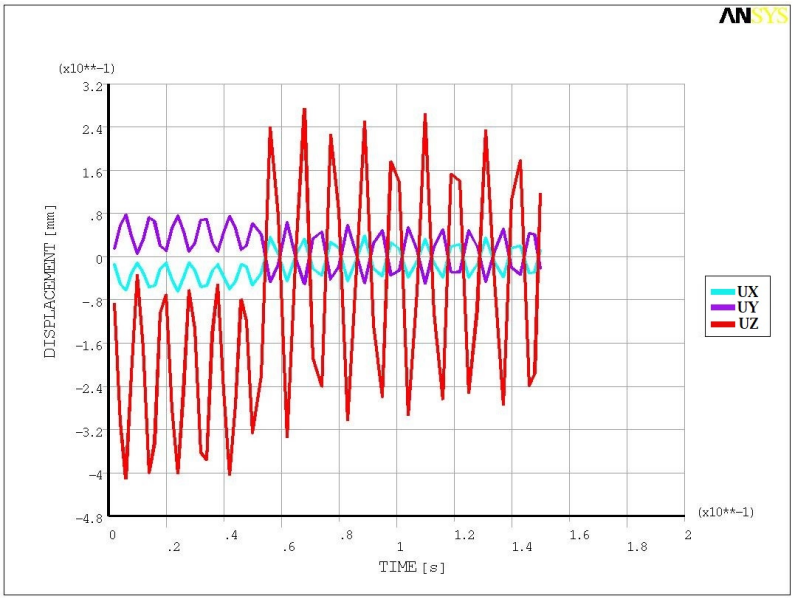

Figure 2.13: FEA model demonstrating the dynamic node oscillations of the bumper, adapted from [6].

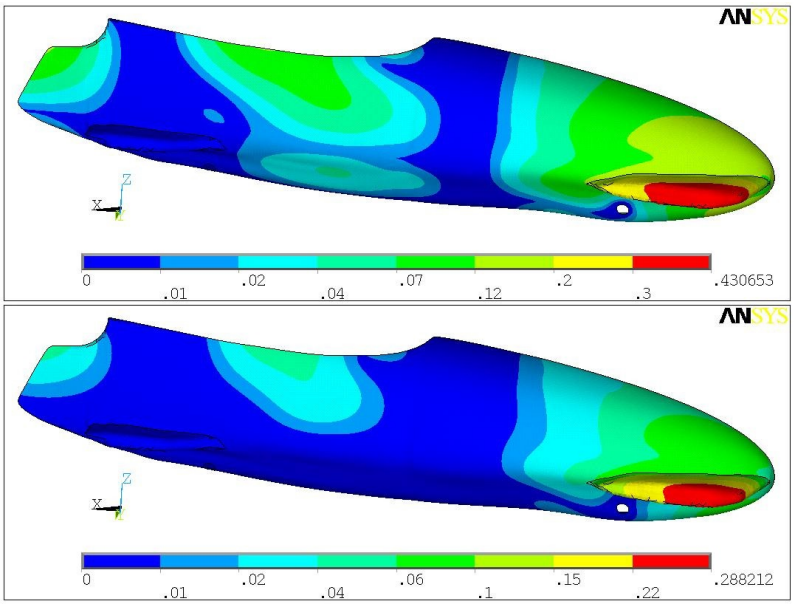

Figure 2.14: FEA simulation of the sled deformation under high g loads by Dabnichki [6].

The limited amount of published research on the structural development of bobsleighs using finite element analysis underscores the significance of this literature review. As a result, it is valuable to explore similar sports and examine their approaches. For instance, motorsport competitions can provide useful insights. In this type of competition, cars are often built with a monocoque structure, similar to bobsleighs. Additionally, these cars experience loads comparable to those experienced in bobsleighs. By examining the design strategies used in motorsport, we can gain valuable insights that can inform the development of bobsleigh structures.

To begin with, Kamble et al., intending to develop a methodology to design lightweight composite monocoques, developed the structure of a sports car designed to pass the static load tests laid down by the International Automobile Federation for Formula 3. To do this research, they resorted to an FEA, using the program *Ansys*. In it, the researchers used the Material Design tool to assess the properties of the composite they were using. Moreover, they also used the tool Spaceclaim to convert the structure into a shell body. To perform the finite element analysis, Kamble et al. used the tool Static Structural [29].

Regarding the boundary conditions, it is crucial to understand that, despite there being three different load cases to analyze, all represented similar boundary conditions, as shown in Figure 2.15. Thus, in all the analyzed load cases, one of the used conditions was symmetry. This condition results from the symmetry not only of the loads applied but also of the monocoque body. Furthermore, another constraint applied intends to simulate the suspension mountings. To do so, the zones where they are mounted were remotely constrained, fixing the vertical direction translation and rotation about two different directions. The forces applied and their application locations varied in the three cases, being applied in the point mentioned in the Formula 3 static loads conditions. However, in all of them, the required force is applied as a remote force. The remote force is applied using deformable loading/remote load methodology, which is a multi-point constraint, with one master node and several slave nodes. Irrespective of the location of the slave nodes from the master node, flexible loading methodology distributes the force using the weighted average method using the centroid of the slave nodes [29].

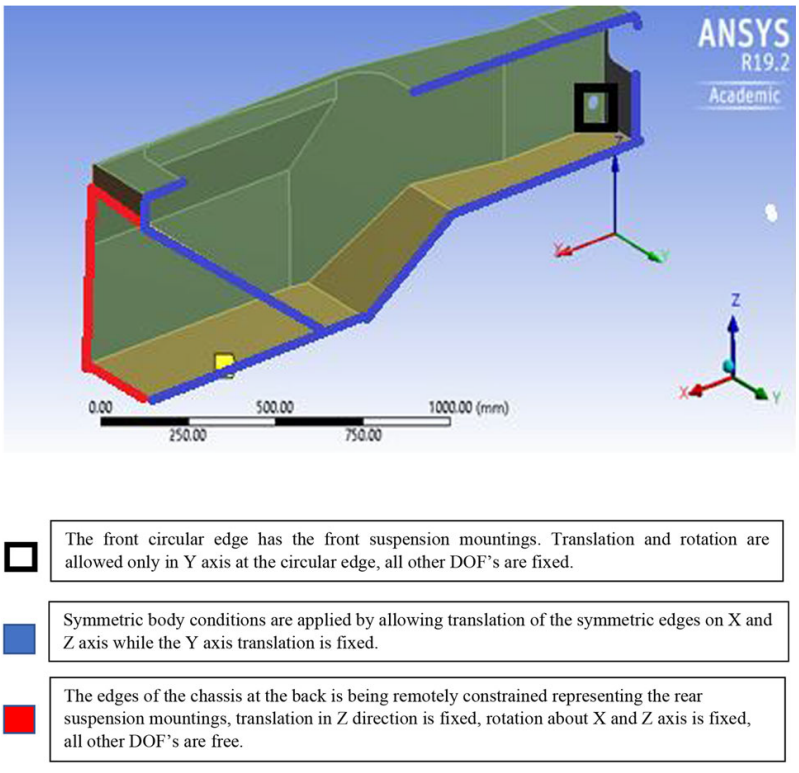

Figure 2.15: Boundary conditions used in the FEA model by Kamble et al. [29].

Finally, to choose the layup of the composites to be used, several analyses had to be carried out. In order to do so, it was important to define what composite failure criteria to consider. Considering that composites behave as orthotropic material, the criteria chosen were Tsai–Wu and maximum stress failure. According to the researchers, it is possible that a certain section of the lamina performs well under one criterion but fails under the other. Thus, a combination of two criteria helps to get more comprehensive and precise results [29].

Another example of finite element usage to develop monocoque structures comes from the *SHELL* eco-marathon. Singh et al. carried out a comparison between the spaceframe, semi-monocoque, and monocoque chassis of a three-wheeler using finite element simulations. The process used was similar to the previous one, using, once again, a surface mesh to represent the structure. To analyze the bending characteristics of the monocoque structure, the mounting brackets of the wheel were identified as the fixed points, fixing not only the translation in each of the three directions but also the rotation in all axis. Finally, to assess the natural frequencies of each of the developed chassis, a modal analysis was carried out in *Ansys* [30].

Finite element models have also been applied to the development of Formula Student cars. In order to evaluate the stiffness of a vehicle for this competition, Eimon et al. constructed a model using *Ansys* 17.1. To help with constructing the laminate in the finite element model, the ACP (*Ansys* Composite PrePost) was used. ACP, as a plugin, has two components: a preprocessor, used to define materials and laminates over desired geometry, and a postprocessor responsible for manipulating and displaying solver outputs to evaluate stresses and strains in each ply [31].

To develop the model, two dimensional surfaces were used to represent the monocoque and one dimensional beam elements to represent the suspension links. These are considered valid assumptions, as in composite layups, length and width are much greater than thickness of the laminate, and in suspension links, length is much greater than either width dimension. Furthermore, this type of simulation allows for better capacity of iterations, since parameters like number of plys or tube thicknesses can be changed without having to update any geometry. The boundary conditions used were selected to mirror that of the torsion test fixture. The rear uprights were fully fixed in translation, but were allowed to rotate about the y-axis. The left upright was only fixed in translation in the z-direction to mimic the vertical support of the test, and the right upright, where load was applied, was left free [31].

2.2 Materials

Regarding the materials used in the development of the structure of the cowling, it has been reported that several inefficiencies of the sleds can be avoided with an appropriate

choice of materials [32]. As a result, most cowling structures are built of fiberglass, carbon fiber, or a mixture of both [7, 9, 33].

In a pursuit to increase the performance of bobsleighs, many different materials have been tested in the development of structures. According to the CITIUS project, all standard elastomeric materials are inadequate to the demands of the sport. Furthermore, many tested adhesives proved not strong enough under the mechanical and thermal stresses of the bobsled racing. To address this issue, the research team created elastomeric damping materials specifically for the CITIUS, while also developing a composite hull strengthened with long-fiber reinforcement [32].

Another example of materials used to increase performance is Versarien, in partnership with Bromley Technologies, launching graphene-enhanced sleds, resulting in a strong performance improvement of their products in the International Bobsleigh and Skeleton Federation World Cup race 2016. They incorporated graphene-enhanced carbon fiber into the skeleton sleds of Bromley. Utilizing these sleds, the athletes managed to set the fastest speed record [34]. With the vast similarities between these two sports, it becomes clear that this might be a possibility to incorporate into the structure of bobsleighs. Furthermore, this case opens the door for a possible use of other particles to increase the mechanical properties of the materials used.

One way carbon fiber composites can be enhanced with graphene is through the incorporation of graphene nanoplatelets into the epoxy. Aluko et al. studied the effect of this incorporation by studying the variation of the elastic modulus with different contents of graphene nanoplatelets in the hybrid composite. The results showed an improvement of up to 10% in the axial elastic modulus, whereas, in the transverse direction, the elastic modulus improved by a value of up to 42% [35].

A second example of enhancing carbon fiber composites with graphene is the use of graphene oxide incorporated into the epoxy matrix. Pathak et al. studied the effect of different weight percentages of graphene oxide on flexural strength and modulus. The results showed that the ratio that improved these characteristics the most was 0.3 %, increasing by 66% the composite flexural strength and increasing by 72% the flexural modulus [36].

Zhang et al., on the other hand, studied the improvement of the tensile performance of graphene-enhanced composites by introducing different content of graphene oxide sheets to the interfacial regions. The results showed that the tensile strength of composites with 5% content of graphene oxide was 34.2% higher than that with no content of graphene oxide [37].

Furthermore, the use of graphene oxide is proven to improve the damping properties of composites. For instance, Gong et al. deposited graphene oxide sheets on the surface of carbon fiber, creating a hybrid composite, and studied its properties. The results show that the deposition can enhance the damping properties of Carbon Fiber Reinforced Polymers (CFRPs) in a wide range of temperature, frequency, and strain domains. Quite sig-

nificantly, the damping loss factor increases by 113% at a frequency of 1 Hz [38].

Finally, another way of enhancing the properties of composites is with the reinforcement of the carbon fiber with carbon nanotubes. Taş and Soykok compared the properties of a hybrid composite with different contents of carbon nanotubes and verified an improvement of Young's modulus by a value of 28.2% in both the main and transverse directions. Moreover, the values of shear modulus G_{12}, G_{31} and G_{23} also increased respectively by 29.9%, 197.6%, and 301.6%, when the content of carbon nanotubes was 0.5%. Furthermore, Taş and Soykok also developed a theoretical model to predict the properties of the hybrid composite and compared them with the results obtained experimentally. In the end, these presented a maximum percentage relative error of up to 9.1%, and the percentage relative error decreased as the carbon nanotube volume fraction increased [39].

Carbon nanotubes have also been proven to enhance damping properties. Khan et al. studied the vibration damping characteristics of carbon fiber reinforced polymer composites containing multiwall carbon nanotubes using the free and forced vibration tests. The damping ratio of the hybrid composites is enhanced with the addition of carbon nanotubes, which is attributed to sliding at the interfaces. In this research, increases of damping up to 24% and 46% for the content of 0.5% and 1% of carbon nanotubes have been recorded [40].

Regarding the tensile strength, studies have shown that the use of carbon nanotubes as a reinforcement of CFRPs can improve these properties. To begin with, Kim et al., by using catalytic growth of carbon nanotubes onto the surface of carbon fiber, achieved increased tensile strength by more than 14% [41]. Furthermore, Lee et al. recorded an increase of tensile strength by 20% on unidirectional carbon fibers and by 30% on woven fabrics [42].

2.3 Regulations

Besides the rules regarding the weight of the bobsleighs, plenty of rules are set to limit the geometry and construction of bobsleighs. These are there to promote the safety of the athletes participating in training and competition and of those present at International Bobsleigh & Skeleton Federation (IBSF) events and to uphold fair and honest competition and are present on the International Bobsleigh Rules in chapter 12 [4]. Next, there is a compendium of some important rules that are needed to comply in the process of developing the cowling structure, extracted from the International Bobsleigh Rules [4].

To begin with, there are some general principles that must be obeyed. These include:

- Bobs must be cowled within the guidelines specified by these rules;
- The rear part of the bobs must be open;

- The bob manufacturers are responsible for the construction of sleds that can withstand, without damage, the stress of repeated heats on the bob tracks;
- For building bobs, it is forbidden to use transparent material, or any material that may shatter as a result of an impact;
- For the purpose of the IBSF, the terms rubber and/or rubber-like material mean a resilient material showing a hardness of less than Shore-D 100 on the ASTM D2240 Durometer test.

Following the general principles, there are some general cowling stipulations that must be followed. Their purpose is to promote the safety of the athletes competing in IBSF events by attempting to ensure that the cowling of a bobsleigh will provide sufficient protection in case of crashes. Furthermore, these aim to promote a competition without unfair aerodynamic advantages. The general stipulations are:

- The brake cut-out must be open;
- No attempt may be made to reduce the area of the cut-out with any material;
- Any unusual additions to the shape that are clearly vortex generators are not allowed;
- Additional holes that may give an improved aerodynamic effect are also not allowed;
- The cowling provides adequate protection for the athletes.

With the purpose of controlling the amount of suspension that can be achieved in the connections between cowling and frame, there are also rules regarding this connection. In this thesis, we will, however, focus just on the regulations regarding the location points of mounting of cowling to frame, which state:

- The cowling must be attached to the frame by means of at least four mounting brackets to restrict the vertical movement of the cowling relative to the frame;
- Two of these four mounting brackets must be positioned symmetrically relative to the plane of symmetry of the bob, in a vertical plane that is perpendicular to the plane of symmetry of the bobsleigh and within 100 mm of most forward part of the rear part of the frame excluding the articulation bolt;
- Two of the four mounting brackets must be positioned symmetrically relative to the plane of symmetry of the bob and must be mounted on or to the outside of the longitudinal frame member.

Chapter 3

Methodology

The current chapter presents a comprehensive approach to the development of the cowling structure, which is divided into four sections: Structure Presentation, Material Database, Loads and Boundary conditions, Models, and Comparison of the Weighting Methods. The first section provides an overview of the whole structure of the bobsleigh, including reinforcements used and the connections between the frame and cowling. The second one serves as a database of all materials used in the cowling development, along with their mechanical properties. In the third section, as a result of the literature review, there is a summary of all the loads the structure needs to withstand and how these will be tested in *Ansys*. In the fourth section, the methods used to generate the mesh, the definition of the materials, and to simulate the loads and boundary conditions are presented. Finally, in the last section, we present the stipulation of a comparison method developed in order to compare the different solutions studied and help select the one that is most suited.

3.1 Geometry Presentation

As previously mentioned, the geometry used in the current thesis was achieved through CFD development by Vasconcelos [21]. Therefore, the current section serves the purpose of presenting the used geometry. Furthermore, in it, the connection points between the cowling and the interior frame will be presented. As presented in Chapter 1, the cowling is divided transversely and has a front part and a rear part, as will be divided the current section: one for subsection the front part and another for the rear part, respectively. The complete geometry of the final bobsleigh is presented in Figure 3.1.

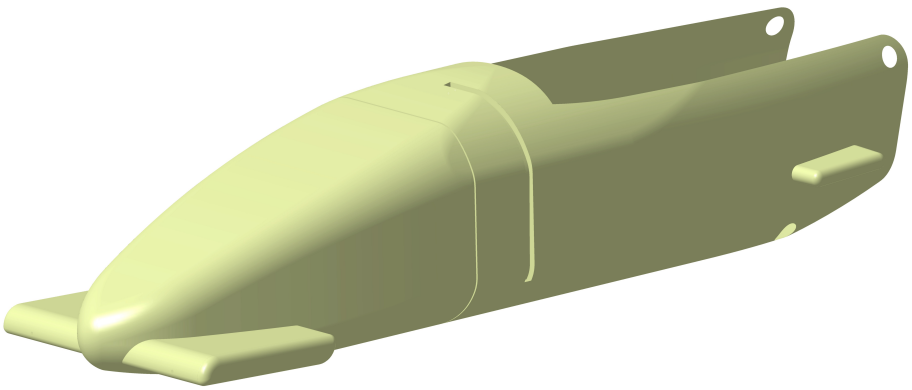

Figure 3.1: Complete Bobsleigh geometry obtained through iterative CFD testing [21].

3.1.1 Front Part

Starting with the front part, it extends from the nose of the bobsleigh until the transversal cut-out at the distance of 1160 mm from the nose. In this part, the main components are the front bumpers, the fuselage, and the spar, as presented in Figure 3.2.

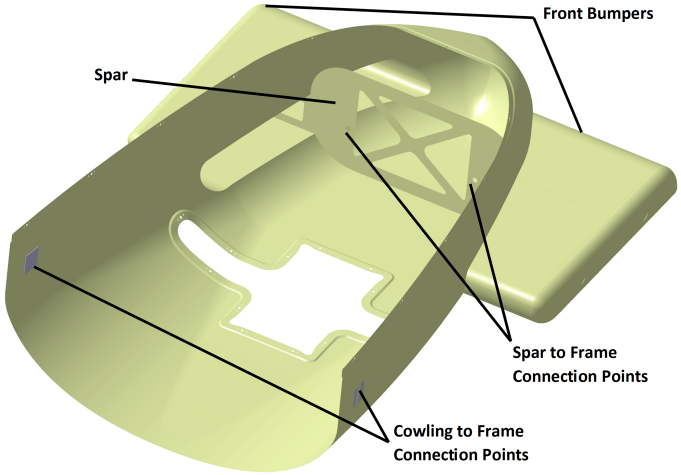

Figure 3.2: Bobsleigh front part structure.

Regarding the bumpers, these serve different purposes. On the one hand, these serve as inverted wings, generating down force. This down force allows for faster turns and for better race lines. On the other hand, bumpers also have the function of absorbing impact loads when the bobsleigh hits the walls of the track [15]. Due to these impacts, the side of the bumpers some times have to be substituted. Therefore, at the very end of each side's bumper there are bumper pads. These also help reduce friction, aiding in maintaining the sled's speed and stability. The bumper pads are attached to bumpers through a bolted connection. In the final geometry, the leading edge of the bumpers are at a distance of 60 mm from the nose, have a mean chord of 500 mm and have a span of 860 mm.

With regards to the fuselage, it has two openings: one top opening and one bottom opening. These help adjusting the mechanical parts inside, both the driving pullers and the runners mounting structure. For the top opening, there has to be a cover with an easy to open connection. For it, we considered a bolted connection with platenuts fixed to the cowling. On the other hand, the cover for the bottom opening has to be partially made out of an elastomeric material, allowing for the upward movement of the runner carriers during the race, partially made out of composite material. For this connection, a bolted connection with platenuts fixed to the cowling will also be used.

In order to carry out the structure development, the worst case scenario was considered, i.e., without the covers attached to the cowling. This assumption tends to oversize the structure, but allows to cover all the possible scenarios. Furthermore, it simplifies the analyses, as *Ansys* tends to have problems simulating bolted connections, leading to unrealistic results.

Finally, regarding the spar, it serves as a connection between the cowling and the interior steel frame structure, using two bolts. Its geometry is also important to assure the structure's low weight and resistance to the loads that it will be subject to. Therefore, the spar's geometry has to be achieved through testing, but it has its position fixed, due to the internal frame structure, and is 865 mm in front of the cowling division.

3.1.2 Rear Part

On the other hand, the rear part extends from the transversal division until the end of the bobsleigh. In it, the main components are: the fuselage, the rear bumpers, the push bar and the push handles, as presented in Figure 3.3.

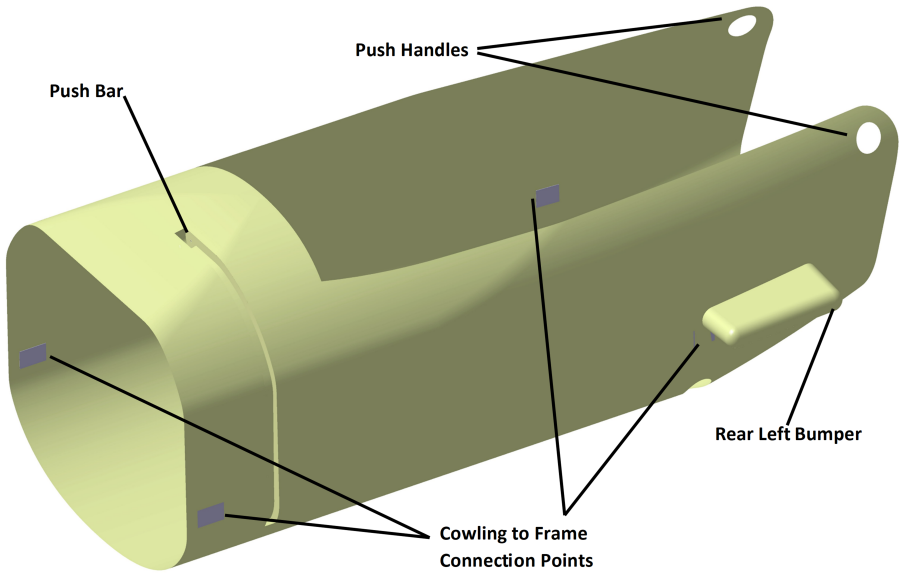

Figure 3.3: Bobsleigh rear part geometry obtained through iterative CFD testing.

Firstly, the fuselage extends from the cowling division through to the rear end of the bobsleigh, with a maximum length of 1680 mm. The fuselage is open on the front, top, and rear of the bobsleigh, as shown in Figure 3.3. Besides these openings, there are also three other openings in the fuselage. The first one is the brake cut out, which has a width of 240 mm, a length of 45 mm, and is at a distance of 1100 mm from the cowling division. The other two openings are the rear runner carriers' cut out, which have a width of 60 mm and are at a distance of 1200 mm from the cowling division, as presented in Figure 3.4. Contrary to what happened in the front part, none of these openings are covered, so as to allow the free movement of the runner carriers and of the brake. The rear part of fuselage has four connection points to the interior frame structure. Two of the connection points are at the front, near the cowling division, and two are at the back, near the runner carrier's connection to the frame, as shown in Figure 3.3.

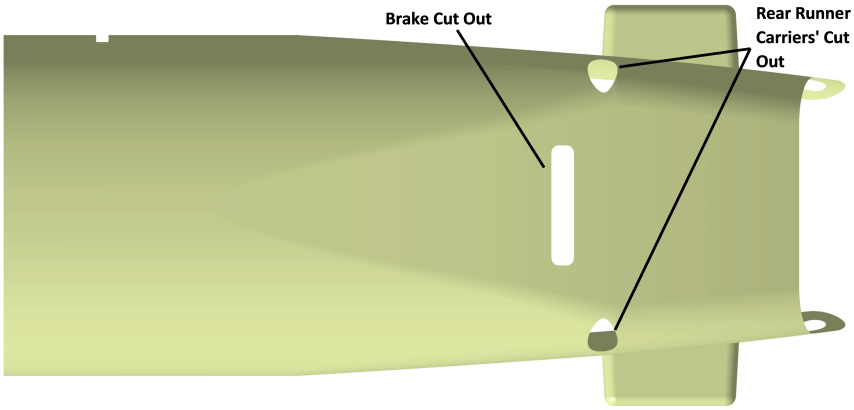

Figure 3.4: Bobsleigh rear part geometry seen from below.

Similarly to the front bumpers, rear bumpers have aerodynamic and structural purposes, generating down force and absorbing impact forces, respectively. However, these do not have bumper pads. This is a result of the harder contacts of the bobsleigh with the walls being with the front bumpers. These rear bumpers have a span of 800 mm, from the tip of the right bumper to the tip of the left one, and a mean chord of 270 mm. Furthermore, these are at a distance of 1195 mm from the cowling division.

With regards to the push bar, there is a cut out on the fuselage with the size and format of the push bar. The dimensions considered for the development of the push bar structure were based on the design presented by Onasch et al. [26]. Therefore, the push bar has a width of 25 mm and is located 185 mm behind the cowling division.

Regarding the push handles, there is a cut out on the surface with a geometry that allows for the brakeman to push the bobsleigh. This component is part of the fuselage and is located at its very end. Its geometry was inspired by the one presented in the IBSF's Regulations [4].

3.2 Material Database

As aforementioned, the choice of the right materials for the cowling is paramount and should be made carefully, as the incorrect choice of materials can lead to inefficiencies. Therefore, several different materials have considered for the development of the structure: five different types of epoxy reinforced with carbon fiber and four different core materials. In addition to these different materials, there was also a study to understand the impact of various manufacturing processes not only to the properties of the aforementioned materials, but also to the structure itself and its behavior.

To begin with, the considered five carbon fibers were selected so as to evaluate the effect that different values Young Modulus of the carbon fiber can have, guiding us towards the most suited type. The tested carbon fibers reinforced polymers, in order from lower

modulus to higher modulus, are as follows: T700S [43], Hexply M47 [44], T1100G [45], M35J [46], and M60J [47]. The first two materials can be considered standard-modulus carbon fibers, the third one intermediate modulus and the last two can be considered high-modulus carbon fibers.

While the T700S, T1100G, M35J, and M60J are to be used with infusion manufacturing, the Hexply M47 is a prepreg. This, allied to the fact that the carbon fibers used in the latter have similar properties to those that make up the T700S, allows it not only to guide us toward determining the correct carbon fiber modulus but also to help identify the appropriate manufacturing process. The mechanical properties of these materials can be found in Tables 3.1 and 3.2.

As mentioned in Section 2.2, in sports similar to bobsleigh, some teams have been exploring the introduction of particles to increase carbon fibers' mechanical properties. As was mentioned then, this introduction of these particles results in increases in the mechanical properties, which, as a result, leads to lighter and more competitive structures. Furthermore, it is also expected that this material leads to a bigger vibration absorption. As a result, in the current thesis, we will analyze the introduction of CNTs into the structure to understand how it affects it.

In order to simulate the insertion of CNTs to the carbon fiber, we applied the improvements verified and presented in Section 2.2 to the mechanical properties of the carbon fibers studied. These new mechanical properties do not allow us to do a full development and definition of the bobsleigh's structure, but allow us to have a better understanding of the impact that these have on the structure. Moreover, these increases allow us to study whether the introduction of CNTs is a viable path and one that needs further investigation. The mechanical properties obtained are presented in the Tables 3.3 and 3.4.

As already mentioned, one of the goals of studying the different materials available is also to understand the impact of different manufacturing processes. To do so, we decided to implement a study on the use of hand-layup manufacturing. This type of manufacturing is the most accessible to us but results in big losses to the mechanical properties. To do this simulation, we decided to implement a reduction of 50% in the mechanical properties of the carbon fibers being studied. This reduction is applied both to elastic and strength properties and is derived from previous research made. The mechanical properties obtained are presented in the Tables 3.5 and 3.6.

The choice for the core materials were made so as to understand the effects of the cores' Young Modulus, densities, and structure. To achieve this, we studied the use of three foams: Airex C70.75[48], Rohacell 110 IG-F[49, 50], and Gurit 250 [51, 52]; and one honeycomb core: Aramid Honeycomb with a density of 48 kg/m^3 [53]. The properties of the different core materials are presented in Table 3.7.

Table 3.1: Carbon fibers' mechanical properties obtained through infusion/Autoclave manufacturing process, accordingly.

	ρ [g/cm^3]	t [mm]	E_1 [GPa]	E_2 [GPa]	E_3 [GPa]	ν_1	ν_2	ν_3	G_{12} [GPa]	G_{23} [GPa]	G_{31} [GPa]
T700 S	1.572	0.093	134	7.5	7.5	0.3	0.1	0.3	4.75	3	4.75
Hexply M47	1.24	0.086	140	7.78	7.78	0.27	0.42	0.27	5	3.08	5
T1100G	1.61	0.093	185	10	10	0.3	0.1	0.3	6.6	2.65	6.6
M35J	1.642	0.092	202	20	20	0.3	0.1	0.3	7.5	2	7.5
M60J	1.539	0.086	360	35	35	0.3	0.1	0.3	13	3.5	13

Table 3.2: Carbon fibers' mechanical properties obtained through infusion/Autoclave manufacturing process, accordingly (Continuation).

	σ_{1tens} [MPa]	σ_{1comp} [MPa]	σ_{2tens} [MPa]	σ_{2comp} [MPa]	σ_{3tens} [MPa]	σ_{3comp} [MPa]	σ_{12} [MPa]	σ_{23} [MPa]	σ_{31} [MPa]
T700 S	2860	-1450	81	-400	81	-400	136	90	136
Hexply M47	2750	-1450	34	-250	34	-250	80	55	80
T1100G	3460	-1870	80	-400	80	-400	160	100	160
M35J	2690	-1400	34	-180	34	-180	55	34	55
M60J	2010	-790	68	-100	68	-100	131	80	131

Table 3.3: Carbon fibers' mechanical properties obtained with the introduction of CNTs.

	ρ [g/cm^3]	t [mm]	E_1 [GPa]	E_2 [GPa]	E_3 [GPa]	ν_1	ν_2	ν_3	G_{12} [GPa]	G_{23} [GPa]	G_{31} [GPa]
T700 S	1.575	0.093	171.52	9.60	9.60	0.3	0.1	0.3	6.17	9.03	9.39
Hexply M47	1.245	0.086	179.20	9.96	9.96	0.27	0.42	0.27	6.50	9.21	9.88
T1100G	1.613	0.093	236.80	12.80	12.80	0.3	0.1	0.3	8.57	7.98	13.04
M35J	1.645	0.092	258.56	25.60	25.60	0.3	0.1	0.3	9.74	6.02	14.82
M60J	1.543	0.086	460.80	44.80	44.80	0.3	0.1	0.3	16.89	10.54	25.69

Table 3.4: Carbon fibers' mechanical properties obtained with the introduction of CNTs (Continuation).

	σ_{1tens} [MPa]	σ_{1comp} [MPa]	σ_{2tens} [MPa]	σ_{2comp} [MPa]	σ_{3tens} [MPa]	σ_{3comp} [MPa]	σ_{12} [MPa]	σ_{23} [MPa]	σ_{31} [MPa]
T700 S	3432	-1740	97.2	-480	97.2	-480	163.2	108	163.2
Hexply M47	3300	-1740	40.8	-300	40.8	-300	96	66	96
T1100G	4152	-2244	96	-480	96	-480	192	120	192
M35J	3228	-1680	40.8	-216	40.8	-216	66	40.8	66
M60J	2412	-948	81.6	-120	81.6	-120	157.2	96	157.2

Table 3.5: Carbon fibers' mechanical properties obtained through hand-layup manufacturing process.

	ρ [g/cm^3]	t [mm]	E_1 [GPa]	E_2 [GPa]	E_3 [GPa]	ν_1	ν_2	ν_3	G_{12} [GPa]	G_{23} [GPa]	G_{31} [GPa]
T700 S	1.572	0.093	67	3.75	3.75	0.3	0.1	0.3	2.375	1.5	2.375
Hexply UD	1.24	0.086	70	3.89	3.89	0.27	0.42	0.27	2.5	1.54	2.5
T1100G	1.61	0.093	92.5	5	5	0.3	0.1	0.3	3.3	1.325	3.3
M35J	1.642	0.092	101	10	10	0.3	0.1	0.3	3.75	1	3.75
M60J	1.539	0.086	180	17.5	17.5	0.3	0.1	0.3	6.5	1.75	6.5

Table 3.6: Carbon fibers' mechanical properties obtained through hand-layup manufacturing process (Continuation).

	σ_{1tens} [MPa]	σ_{1comp} [MPa]	σ_{2tens} [MPa]	σ_{2comp} [MPa]	σ_{3tens} [MPa]	σ_{3comp} [MPa]	σ_{12} [MPa]	σ_{23} [MPa]	σ_{31} [MPa]
T700 S	1430	-725	40.5	-200	40.5	-200	68	45	68
Hexply UD	1375	-725	17	-125	17	-125	40	27.5	40
T1100G	1730	-935	40	-200	40	-200	80	50	80
M35J	1345	-700	17	-90	17	-90	27.5	17	27.5
M60J	1005	-395	34	-50	34	-50	65.5	40	65.5

Table 3.7: Core materials' mechanical properties.

	Airex C70.75	Rohacell 110 IG-F	Gurit 250	Aramid Honeycomb 48
ρ [kg/m^3]	80	110	250	48
Compressive Strength [MPa]	1.45	3	6.88	0.75
Compressive Modulus [MPa]	104	120	296	25
Tensile Strength [MPa]	2	3.5	7.14	0.0015
Tensile Modulus [MPa]	66	160	439	0.5
Shear Strength Width [MPa]	1.2	2.4	4.37	0.3
Shear Modulus Width [MPa]	30	50	98	11
Shear Strength Length [MPa]	1.2	2.4	4.37	0.45
Shear Modulus Length [MPa]	30	50	98	15
Thickness [mm]	1.2 / 2 / 3 / 4 / 5	1 / 2 / 3 / 4 / 5	3 / 4 / 5	2 / 3

3.3 Loads and Boundary Conditions

Based on the literature review presented in Chapter 2, it is possible to infer that during a normal run, the bobsleigh can face several different loading conditions. These different loads and the way they will be evaluated in *Ansys* are presented in the following subsections: g-loads, impact loads, pushing loads, and vibrations.

3.3.1 High Accelerations

As presented previously, when the bobsleigh makes turns at high speeds, the g forces increase drastically as a result of the centrifugal forces. The maximum loads vary from track to track and depend on the turning radius, roll angle, and speed. From the results presented in Chapter 2, acceleration on the bobsleigh's vertical direction can achieve a maximum value of up to 10 g, according to Dabnichki [6]. However, using this result alone would mean no loads in any other direction would be considered, since there is no record of these accelerations.

To overcome this absence of values, considering that acceleration on different directions can be inferred with the value of roll angle, the accelerations on the longitudinal and lateral directions will be obtained with the help of results from other authors. Therefore, according to Braghin et al., the acceleration in the longitudinal direction is around 6% of the vertical acceleration [24]. Furthermore, according to the results presented in Chapter 2, the lateral acceleration can be up to around 30%, as obtained by Лубяко et al. [28]. With these relations in mind, accelerations on the lateral and longitudinal directions were

obtained for the case with 10 g's of vertical acceleration and are shown in Table 3.8.

Table 3.8: Maximum accelerations on the different directions, adapted from [6, 24, 28].

Acceleration [g]		
Longitudinal	Lateral	Vertical
0.6	3.0	10.0

To analyze the structure when subjected to these loads, we considered a static structural analysis, with fixed support in the frame to cowling connections. Furthermore, the maximum accelerations are applied to the cowling structure, including not only the fuselage, but also the remaining parts of the structure. To account for the mass of the cowling top cover on the front part and the brakeman's mass, point masses are used and connected to their respective place, as depicted in Figures 3.5 and 3.6.

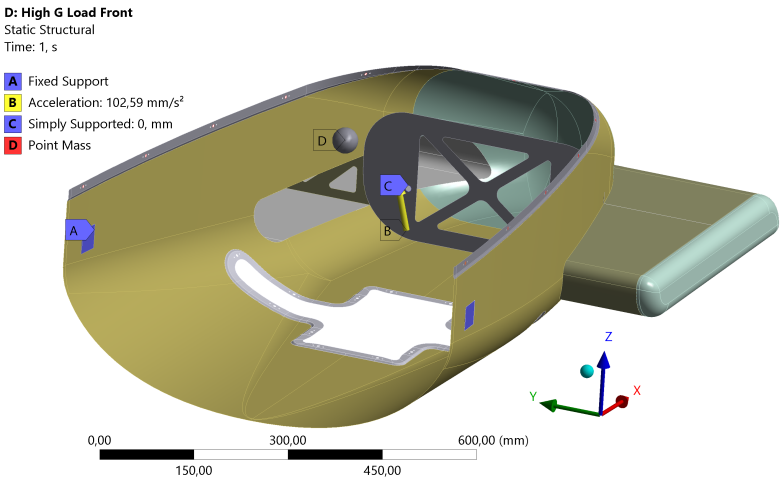

Figure 3.5: Boundary conditions applied to the cowling structure in the High Accelerations loading case on the Front Part.

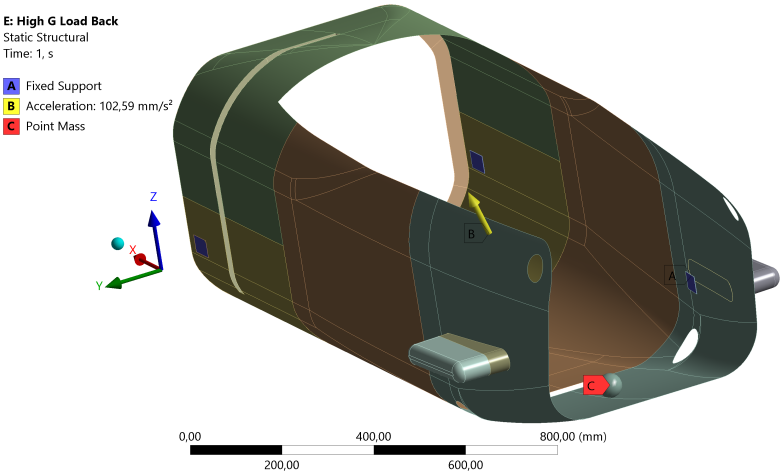

Figure 3.6: Boundary conditions applied to the cowling structure in the High Accelerations loading case on the Rear Part.

3.3.2 Impact Loads

During runs, it is usual to see bobsleighs hitting the walls of the tracks. These impacts result in high loads acting on the bumpers, as seen in Figure 2.2 [22]. When these impacts occur, they tend to happen majorly on the front bumpers. As a result, the force tends to be much larger on the front bumper than on the rear one.

To analyze the structure when subject to these impact loads, there must be a distribution of the impact loads over the two bumpers on the same side. To represent the asymmetry between the front and rear bumpers mentioned in the previous paragraph, it will be considered that the front bumper will withstand the whole impact load recorded in Figure 2.2, whereas the rear bumper will withstand just 30% of it. The resulting loads' distribution is registered in Table 3.9.

Table 3.9: Impact loads' distribution over the two bumpers, adapted from [22].

Impact Loads [N]	
Front Bumper	Rear Bumper
5750	1725

To simulate the loading conditions presented throughout this section, the forces present in Table 3.9 will be applied as Remote Forces in the side faces of the bumpers, as these will be the faces that will be hitting the walls. Regarding boundary conditions, it will be considered that there will be fixed supports on the frame to cowling connections, as presented in figures 3.7 and 3.8.

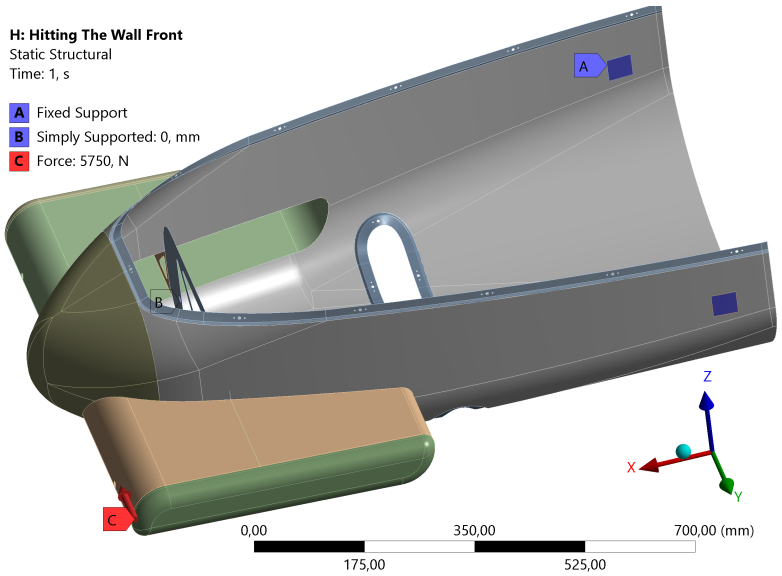

Figure 3.7: Boundary conditions applied to the front part of the cowling structure in the Wall Impact loading case.

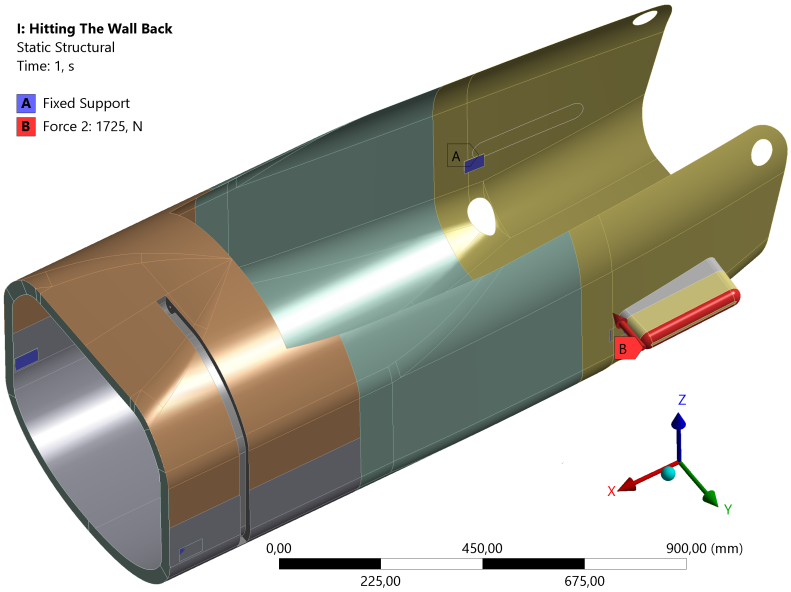

Figure 3.8: Boundary conditions applied to the rear part of the cowling structure in the Wall Impact loading case.

3.3.3 Pushing Loads

During the first phase of the run, athletes push the bobsleigh, applying forces on the bobsleigh's push bar and handles. These resulting forces were presented in Figures 2.8 and 2.9, and are summed up in the Table 3.10.

Table 3.10: Forces applied by the driver and the brakeman during the push-off phase, adapted from [25] and [26].

Push-off phase forces [N]			
Driver x-direction	Driver z-direction	Brakeman x-direction	Brakeman z-direction
860	800	2600	-700

In order to evaluate the structure when subject to the loads characteristic of this phase, these will be applied at the same time. To do so, the Driver's forces will be applied in the push bar-cowling connection, whereas the Brakeman's forces will be applied to the bobsleigh's handles. Regarding supports for the analysis, a fixed support was considered on the cowling to frame connections, as presented in Figure 3.9.

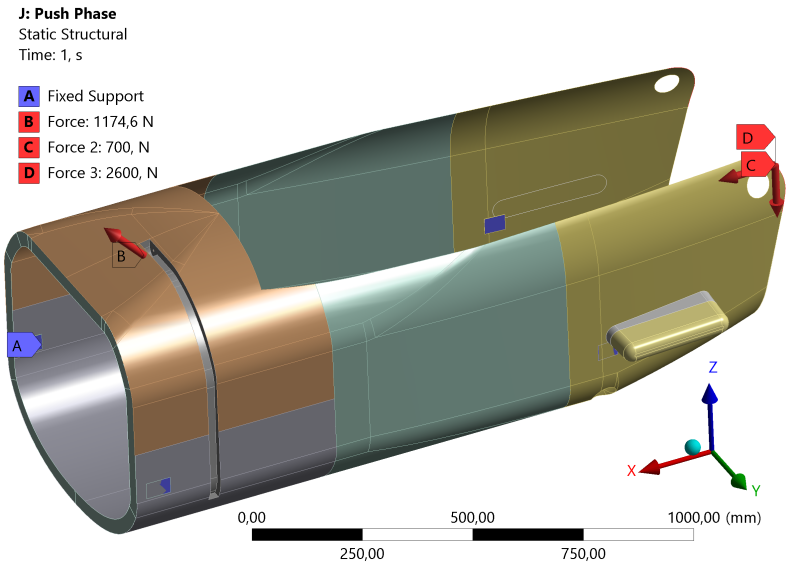

Figure 3.9: Boundary conditions applied to the cowling structure in the Push-off Phase loading case.

3.3.4 Vibrations

As presented previously, during a run, the bobsleigh faces several vibrations, due to irregularities and shocks on the track, in a range of frequencies of up to 23.72 Hz. These vibrations can cause damage to the structure, resulting in a need to evaluate their impact. To do so, using modal analysis, we will calculate the natural frequencies of the structure. The bobsleigh's structure will then be reinforced so that none of the natural frequencies are in the range of frequencies that the bobsleigh can find during runs.

To make this analysis, we considered the use of fixed support on the cowling to frame connection, analyzing just the natural frequencies of the cowling structure. No force was applied, so that the results obtained are the structure's natural frequencies, as presented in Figures 3.10 and 3.11.

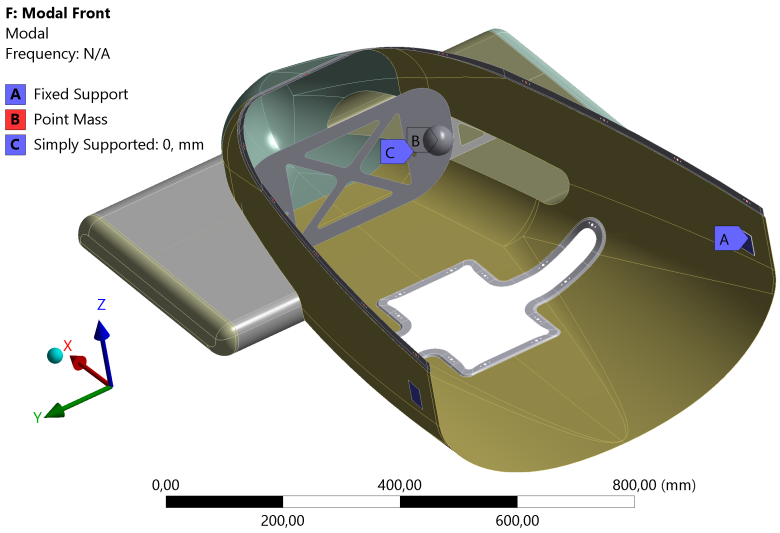

Figure 3.10: Boundary conditions applied to the front part of the cowling structure in the Modal Analysis.

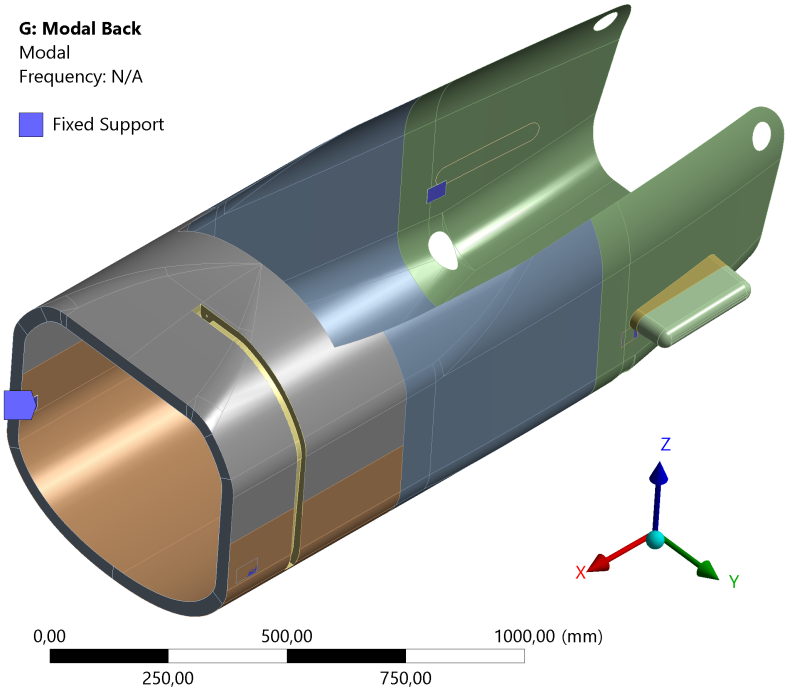

Figure 3.11: Boundary conditions applied to the rear part of the cowling structure in the Modal Analysis.

3.3.5 Deformation Limits and Failure Analysis

In order to carry out the analyses of the structure, we need to define the tolerable deformation values under the different loading cases. To do so, we have to understand how the different conditions affect performance and how often they occur.

To begin with, we have the g-loads loading case. This particular condition, though ex-

treme, tends to occur in every run as a result of the turns at high speed. Considering that, in this case, big deformations would result in a big increase in drag, and consequently in worse performance, it is important that when testing g-loads the maximum deformation is kept at a minimum. Therefore, the deformation limit assumed to this loading condition is of 2 mm.

Similarly, push loads occur in the beginning of every race. Therefore, the deformation should also be kept at a minimum, as the higher the deformation, the higher the bobsleigh's drag, reducing the maximum speed achieved during the push phase. As a result, the deformation limit assumed is of 2 mm.

On the other hand, impact loads do not occur as often as the other loading cases. Moreover, being a result of hitting the walls, impact loads are also associated with the loss of energy and the reduction of speed. As a result, the increase of bobsleigh's drag due to deformation, in the case of impact loading condition, has a lower effect than in other loading conditions. Consequently, in the current case, the deformation limit assumed is of 5 mm.

Regarding the analysis of composite failure, different criteria are available, each with different pros and cons. In order to guarantee the most accurate results, a combination of different criteria would be ideal. However, considering the absence of material constants in the material properties, the choices were limited. Consequently, the failure criteria used were the Tsai-Hill criterion and the maximum stress criterion. The failure analysis will be applied to every loading case, with exception of the vibration loading case, where only the natural frequencies range will be evaluated.

In order to account for imperfections in the manufacturing, and for unpredictable loads, a safety factor has to be taken into consideration. To do so, there was a safety factor used with a value of 1.25. This safety factor will just be used with stresses, not with deformations. This low safety factor was selected bearing in mind that the bobsleigh's structures can be repaired or even substituted in between heats in case of an accident. As a result, considering the higher the safety factor, the heavier the structure, a low safety factor implies a more competitive bobsleigh, but has the disadvantage of having to keep a spare bobsleigh and spare parts in case of an accident. So as to apply the current safety factor, in *Ansys*, the composite analyses, through the Composite Failure Tool, was set to Safety Factor.

3.4 Models

To be able to use *Ansys* correctly and achieve the desired results, it is important that we understand how it works and what can be done in it. To achieve this goal, in this section the different modules available in *Ansys* and the different boundary conditions available that have to be taken into consideration, including how they are simulated, are presented.

3.4.1 Composite Modeling

In order to simulate the composite structures, the *Ansys*' ACP module has been used. In this module, we were able to define the different laminate stack-ups for the different regions of the bobsleigh. In order to do this modeling, *Ansys* uses the Classical Laminate Theory, which provides useful information about the mechanical behavior of a composite structure. To use this model, some assumptions have to be made [54]:

- Layers are perfectly bonded together;
- The material properties of each layer are constant through the thickness;
- Linear-elastic strain-stress behavior;
- Lines originally straight and normal to the mid-plane remain straight and normal in extension and bending;
- Plane stress state;
- In-plane strains and curvature are small compared to all other dimensions.

These assumptions are fulfilled in a relatively thin or moderate thick laminate where the thickness is small compared to the in-plane extensions (length and width), just like the current case of the bobsleigh structure [54].

3.4.1.1 Laminate Stiffness and Compliance Matrices

The laminate stiffness matrix is an 8×8 matrix that contains the **ABD** matrix (6×6), as well as the **C** matrix (2×2), as shown in Equation 3.1. Using this matrix and equation, it is possible to correlate the in-plane forces ($\{N\}$), the moments ($\{M\}$) and the out-of-plane shear ($\{Q\}$) with the laminate's midplane strains ($\{\varepsilon\}$), the laminate curvatures ($\{\kappa\}$), and the transverse shear strain ($\{\gamma\}$) [54, 55, 56].

$$\begin{bmatrix} \{N\} \\ \{M\} \\ \{Q\} \end{bmatrix} = \begin{bmatrix} [A] & [B] & [0] \\ [B] & [D] & [0] \\ [0] & [0] & [C] \end{bmatrix} \begin{bmatrix} \{\varepsilon\} \\ \{\kappa\} \\ \{\gamma\} \end{bmatrix} \quad (3.1)$$

On the one hand, the **ABD** matrix is the stiffness matrix of the laminate. **A** is the in-plane stiffness matrix, **B** describes the coupling between in-plane forces and bending moments and **D** is the flexural stiffness matrix [54].

On the other hand, the **C** matrix is the shear matrix of the laminate and can be represented in the form [54]:

$$\begin{bmatrix} C_{44} & C_{45} \\ C_{54} & C_{55} \end{bmatrix} \quad (3.2)$$

In this matrix, C_{44} and C_{55} represent the G_{23} and G_{31} stiffness, respectively [54].

The compliance matrix is an 8×8 matrix that contains the inverse of the ABD and C matrices [54].

3.4.1.2 ABD Matrix calculation

As previously mentioned, the **ABD** matrix represents the stiffness matrix of the laminate. In order to calculate it, we have to begin by calculating reduced stiffness matrix $\mathbf{Q_{ij}}$ for each material used in the laminate. This matrix describes the elastic behavior of each material in plane loading [56].

$$Q_{ij} = \begin{bmatrix} Q_{11} & Q_{12} & 0 \\ Q_{21} & Q_{22} & 0 \\ 0 & 0 & Q_{66} \end{bmatrix} = \begin{bmatrix} \frac{E_{11}^2}{E_{11}-\nu E_{22}} & \frac{\nu E_{11} E_{22}}{E_{11}-\nu E_{22}} & 0 \\ \frac{\nu E_{11} E_{22}}{E_{11-\nu E_{22}}} & \frac{E_{11}^2}{E_{11}-\nu E_{22}} & 0 \\ 0 & 0 & G_{12} \end{bmatrix} \quad (3.3)$$

To account for the rotation of each ply relative to the principal directions of the laminate, we need to calculate the transformed reduced stiffness matrix $\overline{\mathbf{Q_{ij}}}$. To do so, we need to use the values from the reduced stiffness matrix and the fiber angle (θ) [56]:

$$\overline{Q_{ij}} = \begin{bmatrix} \overline{Q_{11}} & \overline{Q_{12}} & \overline{Q_{16}} \\ \overline{Q_{21}} & \overline{Q_{22}} & \overline{Q_{26}} \\ \overline{Q_{61}} & \overline{Q_{62}} & \overline{Q_{66}} \end{bmatrix} \quad (3.4)$$

Where

$$\overline{Q_{11}} = Q_{11}\cos(\theta)^4 + 2(Q_{12} + 2Q_{66})\cos(\theta)^2\sin(\theta)^2 + Q_{22}\sin(\theta)^4 \quad (3.5)$$

$$\overline{Q_{12}} = \overline{Q_{21}} = Q_{12}(\cos(\theta)^4 + \sin(\theta)^4) + (Q_{11} + Q_{22} - 4Q_{66})\cos(\theta)^2\sin(\theta)^2 \quad (3.6)$$

$$\overline{Q_{16}} = \overline{Q_{61}} = (Q_{11} - Q_{12} - 2Q_{66})\cos(\theta)^3\sin(\theta) - (Q_{22} - Q_{12} - 2Q_{66})\cos(\theta)\sin(\theta)^3 \quad (3.7)$$

$$\overline{Q_{22}} = Q_{11}\sin(\theta)^4 + 2(Q_{12} + 2Q_{66})\cos(\theta)^2\sin(\theta)^2 + Q_{22}\cos(\theta)^4 \quad (3.8)$$

$$\overline{Q_{26}} = \overline{Q_{62}} = (Q_{11} - Q_{12} - 2Q_{66})\cos(\theta)\sin(\theta)^3 - (Q_{22} - Q_{12} - 2Q_{66})\cos(\theta)^3\sin(\theta) \quad (3.9)$$

$$\overline{Q_{66}} = (Q_{11} + Q_{22} - 2Q_{12} - 2Q_{66})\cos(\theta)^2\sin(\theta)^2 + Q_{66}(\cos(\theta)^4 + \sin(\theta)^4) \quad (3.10)$$

Having calculated the transformed reduced stiffness matrix, the **A**, **B** and **D** matrices can be obtained with the following equations [56]:

$$A_{ij} = \sum_{k=1}^{n} \{\overline{Q_{ij}}\}(z_k - z_{k-1}) \tag{3.11}$$

$$B_{ij} = \sum_{k=1}^{n} \{\overline{Q_{ij}}\}(z_k^2 - z_{k-1}^2) \tag{3.12}$$

$$D_{ij} = \sum_{k=1}^{n} \{\overline{Q_{ij}}\}(z_k^3 - z_{k-1}^3) \tag{3.13}$$

In these equations, z represents the vertical position in the ply from the midplane measured in meters [56].

3.4.2 Element Choice in ACP

The underlying principle of ACP is that a composite lay-up is defined on a shell geometry. However, the model of the lay-up that is passed from the ACP preprocessor to the solver can be a shell element mesh, a solid or a solid shell element mesh, where the solid model mesh is an extrusion of the shell element input mesh. The choice of what element type is best suited for the analysis is ultimately dictated by the geometry and loading of the engineering problem [54].

Shell elements are suited for modeling thin-walled to moderately thick-walled structures. Shell elements are compliant in bending and give good deformation results while being computationally inexpensive [54].

Solid elements are aimed at modeling thick walled structures. As laminate thicknesses increase, out-of-plane stresses become more significant, which solid elements are better at approximating. Furthermore, layered solid elements allow the incorporation of composite parts in larger solid model assemblies [54].

Solid-shell elements cover the spectrum between shell and solid elements and are best suited for modeling thin to moderately thick structures. Thin solid-shell elements do not undergo locking and are able to give good results for out-of-plane stresses and strains [54].

Considering the geometry of a typical bobsleigh, it is clear that it has a thin wall structure. As a result, shell elements are suited to the development of the analyses. Furthermore, considering that these elements are compliant with the types of loads that will be tested and that this is achieved while being computationally inexpensive, it becomes clear that shell elements are the most suited for the development of this study.

3.4.3 Mesh Generation

As stated in the previous subsection, for the definition of the mesh, shell elements have been used. To do so, the geometry was imported as shell components only, through an IGES file.

Regarding the sizing, the selection of the size of elements has to be done assuring that it leads to mesh independent results, but still within the computational limits at hand. To achieve this, constantly smaller mesh element sizes were tested in order to guarantee this independence, as will be presented later.

Concerning the geometry of the shell elements, after several tests, it was concluded that the default quadrilateral elements were not suitable for the front bumpers on the preliminary geometry as these led to divergence of the results when testing smaller mesh sizes. Therefore, for these components, it was needed to use **Face Meshing** to define the use of the mesh elements for these. On the final geometry, however, it was seen that this was no longer a problem. As a result, the default geometry was considered for the complete structure, resulting no considerable problems of results convergence. In general, the element types used were SHELL 181.

SHELL181 is a four-node element with six degrees of freedom at each node: translations in the x, y, and z directions, and rotations about the x, y, and z-axes. In general, this element is well-suited for linear, large rotation, and/or large strain nonlinear applications as is the case of analyzing thin to moderately-thick shell structures. In the element domain, both full and reduced integration schemes are supported, accounting for follower (load stiffness) effects of distributed pressures. SHELL181 can be used for layered applications for modeling composite shells or sandwich construction [57].

3.4.4 Boundary Conditions

As shown previously, to simulate the different loading conditions, several boundary conditions have been used. These boundary conditions, often called ”loads” or ”supports”, constrain or act upon the model by exerting forces, rotations, or by fixing the model in such a way that it cannot deform [58].

3.4.4.1 Acceleration

The first boundary condition presented is the **Acceleration** boundary condition and defines a linear acceleration of a structure in each of the global Cartesian axis directions [58].

If desired, acceleration can be used to simulate gravity by accelerating a structure in the direction opposite of gravity. That is, accelerating a structure vertically upwards (+Y)

at 9.80665 m/s^2, applies a force on the structure in the opposite direction (-Y) inducing gravity (pushing the structure back towards earth). Units are length/time^2 [58].

This type of boundary conditions will be used to simulate the accelerations to which the structure is subject in a normal run down the track, as mentioned earlier.

3.4.4.2 Remote Force

A **Remote Force** is equivalent to a regular force load on a face or an edge. A remote force can be applied to a face, vertex, element face, or node of a 3D model, or to an edge, vertex, or node of a 2D model [58].

A Remote Force can be used as an alternative to building a rigid part and applying a force load to it. The advantage of using a remote force load is that one can directly specify the location in space from which the force originates [58].

In the current case study, this type of boundary condition will be used to simulate the loads from hitting the wall and the push-off phase.

3.4.4.3 Fixed Support

The **Fixed Support** boundary condition prevents a selected geometric or mesh entity from moving or deforming, preventing rotation and displacements. It can be applied to 2D and 3D models to support bodies, faces, edges, and vertices. Though it is possible to fix both edges and vertices, these tend to be not realistic, as it leads to singular stresses, i.e., stresses that approach infinity near the fixed edges or vertices [58].

This support will be used to simulate connections between the frame and the cowling structures, where there is no rotation nor displacement.

3.4.4.4 Simply Supported

The **Simply Supported** boundary condition prevents one or more straight or curved edges or a vertex or vertices from moving or deforming. This type of support differentiates itself from fixed support by allowing the rotation of the structure around the supported edges os vertices [58].

It is available for Surface/Shell faces, Wire/Line/Beam bodies, Edges and Vertices. Just like the previous boundary condition, this one is also not suitable for vertex support, as it leads to unrealistic singular stresses [58].

This boundary condition will be used to simulate connections between the frame and the cowling structures, where there is no displacement, but can exist rotation of the structure.

3.4.5 Types of Analysis

Considering the different loads to be analyzed, it is of paramount importance to understand what different analyses existing in *Ansys* are most suited to each of the different loading conditions.

3.4.5.1 Modal Analysis

A modal analysis determines the vibration characteristics (natural frequencies and mode shapes) of a structure or a machine component. It can also serve as a starting point for another, more detailed, dynamic analysis, such as a transient dynamic analysis, a harmonic analysis, or a spectrum analysis. The natural frequencies and mode shapes are important parameters in the design of a structure for dynamic loading conditions. One can also perform a modal analysis on a pre-stressed structure, such as a spinning turbine blade [58].

If there is damping in the structure or machine component, the system becomes a damped modal analysis. For a damped modal system, the natural frequencies and mode shapes become complex [58].

This analysis, as explained earlier, was used in the current case study to evaluate the natural frequencies of the structure and, as a result, making sure that none of the natural frequencies are in the vibrations' frequencies range of a normal descent.

3.4.5.2 Static Structural

A static structural analysis determines the displacements, stresses, strains, and forces in structures or components caused by loads that do not induce significant inertia and damping effects. Steady loading and response conditions are assumed; that is, the loads and the structure's response are assumed to vary slowly with respect to time. A static structural load can be performed using *Ansys*, Samcef, or ABAQUS solvers. The types of loading that can be applied in a static analysis include [58]:

- Externally applied forces and pressures;
- Steady-state inertial forces (such as gravity or rotational velocity);
- Imposed (nonzero) displacements
- Temperatures (for thermal strain)

Static structural analysis can be either linear or nonlinear. All types of nonlinearities are allowed - large deformations, plasticity, stress stiffening, contact (gap) elements, hyperelasticity, and so on [58]. Despite this, only linear analyses have been performed.

This analysis type was used for all of the structural analyses, apart from those to calculate the natural frequencies. From these analyses, it was possible to obtain results for parameters such as deflections and composite failure.

3.5 Comparison of the Weighting Methods

In order to be able to select the most suitable combination of materials for the problem at hand, several different structures were designed combining the available materials. As a consequence, there will be a set of results that must be treated in order to compare the different solutions and find the most suitable one. To facilitate this process, a systematic method for assigning weights to different important criteria was developed. This required defining the crucial criteria for evaluation, establishing their relative significance, and determining how the different cases relate to each criterion.

Hence, this comparison began with the establishment of the evaluation criteria. Given the limited budget available to manufacture the bobsleigh, especially in comparison to other teams, the price of materials and manufacturing accessibility emerged as two paramount criteria for the comparative analysis.

In addition to these two criteria, the influence of each studied solution on the bobsleigh's performance is of vital importance, considering the goal is to build a competitive bobsleigh. To assess this impact, we had to consider both the mass of the structure and its natural frequencies. The mass of the structure was chosen as a criterion due to its direct correlation with the potential use of additional ballast weight, allowing for center of gravity adjustments and thereby enhancing the bobsleigh's performance, as mentioned previously. Moreover, natural frequencies offer a means to evaluate a structure's capacity to dampen vibrations. Higher natural frequencies indicate greater vibration absorption within the structure, resulting in smoother bobsleigh performance.

Considering these criteria, and attaching more importance to the budget related criteria, the weights for the different criteria are divided as presented in Table 3.11.

Table 3.11: Distribution of the criteria weights.

Criterion	**Weight**
Cost	5
Manufacturing Accessibility	6
Total Mass	6
Natural Frequencies	3
Total	20

For each criteria, each studied case (i) will receive a non-dimensional value between 0 and 1 (ND_{cost_i} for the Cost criterion, ND_{acc_i} for the Manufacturing Accessibility criterion, ND_{mass_i} for the Total Mass criterion, and ND_{NF_i} for the Natural Frequencies criterion), that will be multiplied by the criterion weight (W_{cost}, W_{acc}, W_{mass}, W_{NF}). The sum of the

values for the different criteria will result in the final value attributed to the case studied, as a result of a merit function (MF_i) shown in Equation 3.14.

$$MF_i = ND_{cost_i} \times W_{cost} + ND_{acc_i} \times W_{acc} + ND_{mass_i} \times W_{mass} + ND_{NF_i} \times W_{NF} \quad (3.14)$$

3.5.1 Cost Criterion

As previously mentioned, there was a need to evaluate the different solutions and evaluate the costs of each solution. To achieve this goal, instead of calculating the price of the whole structure, to simplify, we divided this criterion into two criteria: the price of the fiber and the cost of the core. In order to apply this simplification, we had to divide the total weight of the criterion into two, accounting for the higher total cost of the fiber, compared to the cost of the core material. As a result, the weight given to the cost of the fiber is 3, whereas the weight given to the cost of the core is 2.

With this simplification made, the non-dimensional value given to the different materials are shown in Tables 3.12 and 3.13.

Table 3.12: Non-dimensional values attributed to the cost of the different fibers studied.

HexplyM47	1
T1100G	0.8
T700S	0.8
M35J	0.75
M60J	0.7

Table 3.13: Non-dimensional values attributed to the cost of the different core materials studied.

Airex	1
Rohacell	0.6
Gurit 250	0.55
Aramid Honeycomb	0.5

3.5.2 Manufacturing Accessibility Criterion

Unlike every other criterion, this one is a more subjective one. It encompasses not only the cost of the different manufacturing process, but also how easy and accessible the manufacturing processes is. As a result, it was decided that a constant step distribution of the non-dimensional values, with the highest value of 1 being attributed to the easiest and most accessible manufacturing process would be used. The value attributed to the other manufacturing processes will be obtained through the use of a constant step reduction. The constant step considered was of 0.25.

To begin with, the most accessible manufacturing process is, undoubtedly, the hand-layup process. This process usually ends up with worse properties, but is the one that is most accessible and with the least technological requirements. Therefore, the non-dimensional value of 1 was attributed to this manufacturing process.

On the opposite side of the spectrum, the deposition of CNTs to the carbon fiber is the one that is more expensive and least accessible. This is a result of the complex techniques used in order to guarantee a good dispersion of CNTs and an avoidance of agglomerates that lead to reductions of the mechanical properties of the material. Consequently, this is the manufacturing process with the lowest non-dimensional value. Considering the constant step of 0.25, this process will end up with a non-dimensional value of 0.25.

In between these two previously mentioned manufacturing processes, we have the infusion manufacturing process and the Autoclave manufacturing process. Both of these present big difficulties and have their own problems. On the one hand, in Autoclave manufacturing the layup is cured in an autoclave due to the simultaneous application of heat and pressure, and can be seen as the easier process as it does not require the handling and mixing of resins [59]. However, this process is associated with higher tooling and fabric costs [60], and can have its size limited by the size of the autoclave [59]. Regarding the infusion manufacturing process, in scenarios with low expertise on the matter, it can also lead to problems removing all the air from the composite, reducing the composite quality [61].

Analyzing the means available and bearing in mind the expertise in infusion manufacturing available and the higher costs associated with using Autoclave manufacturing, it was possible to conclude that, out of these two, the most accessible one is infusion manufacturing. Thus, to this manufacturing process will be attributed a non-dimensional value of 0.75, whereas the Autoclave manufacturing process will be attributed a non-dimensional value of 0.5.

Bearing these considerations in mind, the final distribution is the one presented in Table 3.14.

Table 3.14: Non-dimensional values attributed to the different manufacturing processes.

Hand-layup	1
Infusion	0.75
Autoclave	0.5
CNTs Deposition	0.25

3.5.3 Total Mass

As previously stated, as a rule of thumb, we can consider that, with every other parameter the same, the lower the mass of the structure, the better the performance of the bobsleigh. Thus, we considered that the non-dimensional value of a generic case i (ND_{cost_i}) could

be calculated by dividing the lowest total mass achieved out of all the cases (m_{min}) by the total mass of the case studied (m_i), as presented in Equation 3.15.

$$ND_{mass_i} = \frac{m_{min}}{m_i} \quad (3.15)$$

As a result of this attribution of non-dimensional value, the lower the mass of a case, the higher the value, as intended. Furthermore, the case with the lowest mass will receive a non-dimensional value of 1.

3.5.4 Natural Frequencies

As mentioned previously, higher natural frequencies in a structure indicate better vibration absorption. Consequently, when assigning values to the non-dimensional values, it is imperative to account for the relationship that higher natural frequencies should correspond to higher non-dimensional values. To achieve these non-dimensional values, the natural frequencies of the studied case (NF_i) will be divided by the highest attained natural frequency value (NF_{max}), as presented in Equation 3.16.

$$ND_{NF_i} = \frac{NF_i}{NF_{max}} \quad (3.16)$$

Considering that, in order to simplify the analysis, we had to study the front and rear parts of the bobsleigh separately, the weight for the natural frequencies' criterion will be divided into two: the front part natural frequencies and the rear part natural frequencies, both with the same weight.

3.6 Design Process

As previously stated, *Ansys* was used to analyze the cowling structure. In order to understand the process used to analyze the structure, it is important to know that *Ansys* functions in the form of a project schematic, where every component used is arranged in the form of a tree in the Workbench.

To begin with, we started the project schematic by using the **Engineering Data** component. Here, the material properties presented in Section 3.2 were defined and made available for the following components. Beyond the properties presented, there was a need to define the Ply Type of each material. This property assures the correct failure mode is evaluated and has several different options available. For the tested carbon fibers, con-

sidering they are all unidirectional, the option selected was ”Regular”, as it is the ply type used to simulate unidirectional materials. For the foams used as core materials, we selected the option adapted to isotropic core materials, i.e., ”Isotropic Homogeneous Core”. Finally, for the Aramid Honeycomb core, we selected the ”Honeycomb Core” ply type.

The second component used was the **Geometry** one, responsible for the creation of the geometry of the structure. Considering that the structure was designed in CATIA V5, this component serves just to import the geometry with an IGES file, as previously mentioned, and to verify there was no problem while importing the geometry.

The geometry and material properties defined were, then, passed on to the following component: the **ACP** component. In it, we started by defining the **Model**, with the creation of the mesh and with the definition of contacts between the different parts of the structure. Furthermore, in the Model, it is also necessary to create named selections of elements, faces, and edges.

Having finished the Model definition, we start with the creation of the **Setup**. Here, there is the definition of the fabrics that are going to be used, based on the materials created in the Engineering Data component; the definition of the Rosettes; and the definition of the Oriented Selection Sets, representing each part of the structure, and the creation of the Modeling Plies. This last part is responsible for defining what laminate will be used in each of the Oriented Selection Sets.

The output of the ACP component is subsequently passed on to the respective analysis components, namely the **Modal Analysis** or the **Static Structural** analysis components, as discussed in the previous section. Within these components, we establish the appropriate boundary conditions and solve the problem at hand. The results of these analyses give the desired results, namely the natural frequencies in the case of modal analysis or the deformations and inverse reserve factor for static structural analysis. To optimize computational resources, each loading case is divided into two distinct analyses, specifically addressing the front and rear sections of the structure, respectively. This analyses separation is viable considering the physical separation between front and rear parts through the transversal cowling division.

The results obtained from these analyses form the foundation of the structure design as they provide insights into the areas that require reinforcement and those that are currently oversized. With this in mind, the structure can be rectified through adjustments in either the laminate used or the overall geometry of the structure itself. To implement these corrections, changes can be made in the ACP component and Geometry, respectively. The goal of this process and of the changes made is to maximize the value of the Merit Function presented in Equation 3.14 by changing several project variables.

First of all, the first project variable to be tested is the amount of carbon fiber reinforced polymer layers used. Secondly, regarding the core of the sandwich used for the structure of the cowling, another project variable is the thickness of the material used. Then,

the carbon fiber reinforced polymer layers' orientations used are changed to be in accordance to the loads applied, as the correct orientation can help reduce the amount of carbon fiber reinforced polymer used and improve the structure performance. Another variable changed in every design process made is the change of the amount and dimensions of the laminate zones used within the cowling structure. Finally, the last variable to be tested is the width of the former used in the transversal division in the rear part of the cowling.

The design process presented in this section is represented schematically in Figure 3.12.

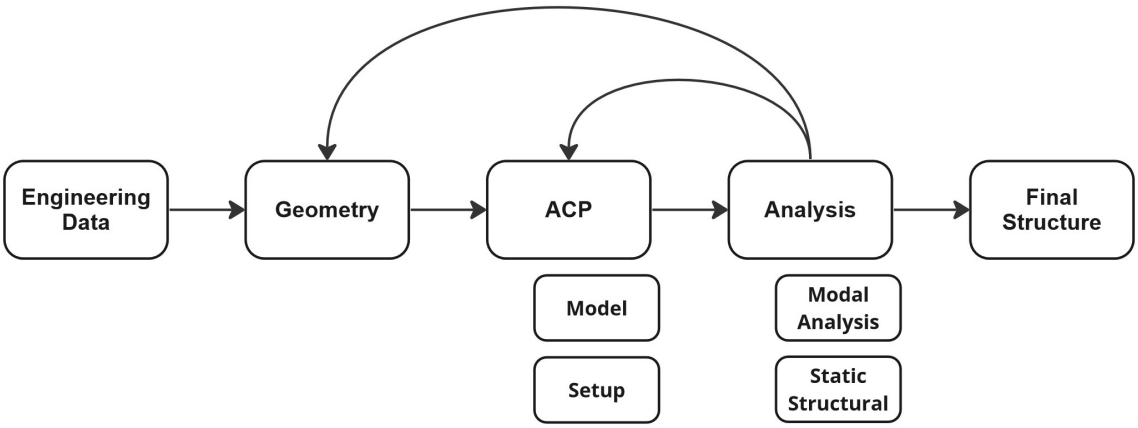

Figure 3.12: Schematic representation of the design process.

Chapter 4

Results

In this chapter, the bobsleigh's structure is developed, showing the results obtained until the final structure is selected. To achieve this goal, this chapter is divided into two parts. On the first part, some preliminary results are obtained, by carrying out tests and analyses on one of the first geometries of the bobsleigh, developing structures for each of the different available material combinations. With these results, the different materials are compared allowing a first selection of material combinations suitable for this application. On the second part, analyses are carried out on the most recent geometry with the materials selected, ending up with the final structure of the bobsleigh. At the end of the chapter, there is also the study of the mesh independence on it and the discussion of final structure configuration.

4.1 Preliminary Results

As mentioned in Chapter 1, in the current thesis a structure based on a geometry obtained through CFD design is being developed. As a result, while the current thesis was being developed, the geometry was constantly being tested and being iteratively improved. In order to advance with the structure development, some preliminary tests in *Ansys* were carried out using the first bobsleigh geometry. This consideration does not allow us to develop the final structure of the bobsleigh, but does allow us to have good notions of how different materials affect the structure and performance of bobsleigh.

Bearing in mind everything previously mentioned, the *Ansys* analyses were carried out on the first bobsleigh's geometry with the different combinations of carbon fibers, core materials and manufacturing processes aforementioned, having been developed and designed a total of 60 different structures, one for each material combination, in accordance to the Design Process presented in Section 3.6. In order to compare the different material combinations, the Weighting Methods comparison presented in Section 3.5 was used. These results were then registered in Tables 4.1 through 4.15, where, for every case and for each criterion, we have the nominal values (**N**), the non-dimensional values (**ND**) and the non-dimensional value multiplied by the criterion weight (**ND x W**). The sum of all the non-dimensional values multiplied by the criteria weights is presented as the total.

The results used were then compiled into Table 4.16. With this table, it is possible to more easily compare the different combinations of carbon fibers, core materials and manufacturing processes.

Table 4.1: Results of the *Ansys* analyses for the different combinations of the T700S carbon fiber with infusion manufacturing used for the weight method comparison.

	N	ND	ND x W	N	ND	ND x W	N	ND	ND x W	N	ND	ND x W
Carbon Fiber	T700S	0.8	2.4	T700S	0.8	2.4	T700S	0.8	2.4	T700S	0.8	2.4
Core Material	Airex	1.0	2.0	Rohacell	0.6	1.2	Gurit250	0.6	1.1	Aramid Honeycomb	0.5	1.0
Manufacturing Process	Infusion	0.8	4.5	Infusion	0.8	4.5	Infusion	0.8	4.5	Infusion	0.8	4.5
Total Mass	8.7301	0.5989	3.5935	10.0435	0.5206	3.1236	7.9259	0.6597	3.9581	7.9259	0.6597	3.9581
Front Natural Frequencies	72.8900	0.6795	1.0193	76.0970	0.7094	1.0641	73.2410	0.6828	1.0242	73.2410	0.6828	1.3510
Rear Natural Frequencies	97.4490	0.7873	1.1810	78.2090	0.6319	0.9478	94.3080	0.7620	1.1429	94.3080	0.7620	1.1429
		Total	14.6938		**Total**	13.2355		**Total**	14.1252		**Total**	14.0252

Table 4.2: Results of the *Ansys* analyses for the different combinations of the T700S carbon fiber with CNTs used for the weighting method comparison.

	N	ND	ND x W	N	ND	ND x W	N	ND	ND x W	N	ND	ND x W
Carbon Fiber	T700S	0.8	2.4	T700S	0.8	2.4	T700S	0.8	2.4	T700S	0.8	2.4
Core Material	Airex	1.0	2.0	Rohacell	0.6	1.2	Gurit250	0.6	1.1	Aramid Honeycomb	0.5	1.0
Manufacturing Process	CNTs	0.2500	1.5000	CNTs	0.2500	1.5000	CNTs	0.2500	1.5000	CNTs	0.2500	1.5000
Total Mass	8.6286	0.6060	3.5935	8.4668	0.6175	3.7052	9.1477	0.5716	3.4295	7.2053	0.7257	4.3540
Front Natural Frequencies	67.4260	0.6286	0.9428	65.5010	0.6106	0.9159	65.5010	0.6106	0.9159	66.7000	0.6218	0.9327
Rear Natural Frequencies	89.9060	0.7264	1.0896	79.8360	0.6450	0.9676	82.6660	0.6679	1.0019	99.0760	0.8005	1.2007
		Total	11.5259		**Total**	10.6887		**Total**	10.3472		**Total**	11.3874

Table 4.3: Results of the *Ansys* analyses for the different combinations of the T700S carbon fiber with hand-layup manufacturing used for the weighting method comparison.

	N	ND	ND x W	N	ND	ND x W	N	ND	ND x W	N	ND	ND x W
Carbon Fiber	T700S	0.8	2.4	T700S	0.8	2.4	T700S	0.8	2.4	T700S	0.8	2.4
Core Material	Airex	1.0	2.0	Rohacell	0.6	1.2	Gurit250	0.6	1.1	Aramid Honeycomb	0.5	1.0
Manufacturing Process	Hand-layup	1.0	6.0	Hand-layup	1.0	6.0	Hand-layup	1.0	6.0	Hand-layup	1.0	6.0
Total Mass	12.0414	0.4342	2.6053	12.5934	0.4152	2.4911	13.1634	0.3972	2.3832	11.5062	0.4544	2.7265
Front Natural Frequencies	72.9330	0.6799	1.0199	77.3710	0.7213	1.0819	77.3710	0.7213	1.0819	66.5730	0.6206	0.9309
Rear Natural Frequencies	79.4810	0.6422	0.9633	70.5960	0.5704	0.8556	63.2290	0.5109	0.7663	77.0060	0.6222	0.9333
		Total	14.9884		**Total**	14.0286		**Total**	13.7314		**Total**	13.9907

Table 4.4: Results of the *Ansys* analyses for the different combinations of the Hexply M47 carbon fiber with Autoclave manufacturing used for the weighting method comparison.

	N	ND	ND x W	N	ND	ND x W	N	ND	ND x W	N	ND	ND x W
Carbon Fiber	Hexply M47	1.0	3.0	Hexply M47	1.0	3.0	Hexply M47	1.0	3.0	Hexply M47	1.0	3.0
Core Material	Airex	1.0	2.0	Rohacell	0.6	1.2	Gurit250	0.6	1.1	Aramid Honeycomb	0.5	1.0
Manufacturing Process	Autoclave	0.5	3.0	Autoclave	0.5	3.0	Autoclave	0.5	3.0	Autoclave	0.5	3.0
Total Mass	10.7636	0.4858	2.9146	9.5586	0.5470	3.2820	10.1098	0.5172	3.1031	8.9210	0.5861	3.5166
Front Natural Frequencies	72.7640	0.6783	1.0175	89.7920	0.8371	1.2556	89.7920	0.8371	1.2556	89.2430	0.8319	1.2479
Rear Natural Frequencies	70.9530	0.5733	0.8599	86.9500	0.7025	1.0538	82.4500	0.6662	0.9992	90.0430	0.7275	1.0913
		Total	12.7920		**Total**	12.7914		**Total**	12.4579		**Total**	12.8558

Table 4.5: Results of the *Ansys* analyses for the different combinations of the Hexply M47 carbon fiber with CNTs manufacturing used for the weighting method comparison.

	N	ND	ND x W	N	ND	ND x W	N	ND	ND x W	N	ND	ND x W
Carbon Fiber	Hexply M47	1.0	3.0	Hexply M47	1.0	3.0	Hexply M47	1.0	3.0	Hexply M47	1.0	3.0
Core Material	Airex	1.0	2.0	Rohacell	0.6	1.2	Gurit250	0.6	1.1	Aramid Honeycomb	0.5	1.0
Manufacturing Process	CNTs	0.3	1.5	CNTs	0.3	1.5	CNTs	0.3	1.5	CNTs	0.3	1.5
Total Mass	9.2694	0.5641	3.3844	8.3564	0.6257	3.7542	10.0015	0.5228	3.1367	6.2540	0.8360	5.0162
Front Natural Frequencies	79.5010	0.7411	1.1117	95.4680	0.8900	1.3350	96.4510	0.8991	1.3487	82.3480	0.7677	1.1515
Rear Natural Frequencies	74.5400	0.6022	0.9034	92.4500	0.7469	1.1204	81.5460	0.6589	0.9883	103.1400	0.8333	1.2500
		Total	11.8995		**Total**	11.9096		**Total**	11.0737		**Total**	12.9177

Table 4.6: Results of the *Ansys* analyses for the different combinations of the Hexply M47 carbon fiber with hand-layup manufacturing used for the weighting method comparison.

	N	ND	ND x W	N	ND	ND x W	N	ND	ND x W	N	ND	ND x W
Carbon Fiber	Hexply M47	1.0	3.0	Hexply M47	1.0	3.0	Hexply M47	1.0	3.0	Hexply M47	1.0	3.0
Core Material	Airex	1.0	2.0	Rohacell	0.6	1.2	Gurit250	0.6	1.1	Aramid Honeycomb	0.5	1.0
Manufacturing Process	Hand-layup	0.5	3.0	Hand-layup	0.5	3.0	Hand-layup	0.5	3.0	Hand-layup	0.5	3.0
Total Mass	14.8985	0.3509	2.1057	12.4535	0.4198	2.5191	16.7904	0.3114	1.8684	12.9508	0.4037	2.4224
Front Natural Frequencies	72.4320	0.6752	1.0128	91.5400	0.8534	1.2800	94.4760	0.8807	1.3211	81.4520	0.7593	1.1390
Rear Natural Frequencies	57.8940	0.4678	0.7016	78.4870	0.6341	0.9512	55.2790	0.4466	0.6699	73.5420	0.5942	0.8913
		Total	14.8202		**Total**	14.9503		**Total**	13.9595		**Total**	14.4526

Table 4.7: Results of the *Ansys* analyses for the different combinations of the T1100G carbon fiber with infusion manufacturing used for the weighting method comparison.

	N	ND	ND x W	N	ND	ND x W	N	ND	ND x W	N	ND	ND x W
Carbon Fiber	T1100G	0.8	2.4	T1100G	0.8	2.4	T1100G	0.8	2.4	T1100G	0.8	2.4
Core Material	Airex	1.0	2.0	Rohacell	0.6	1.2	Gurit250	0.6	1.1	Aramid Honeycomb	0.5	1.0
Manufacturing Process	Infusion	0.8	4.5	Infusion	0.8	4.5	Infusion	0.8	4.5	Infusion	0.8	4.5
Total Mass	9.8949	0.5284	3.1705	9.4073	0.5558	3.3348	9.0657	0.5767	3.4605	7.9752	0.6556	3.9336
Front Natural Frequencies	62.5820	0.5834	0.8751	61.5920	0.5742	0.8613	61.5920	0.5742	0.8613	80.3550	0.7491	1.1236
Rear Natural Frequencies	76.5020	0.6181	0.9271	71.9450	0.5813	0.8719	76.5740	0.6187	0.9280	90.5710	0.7318	1.0977
		Total	13.8727		**Total**	13.1680		**Total**	13.2498		**Total**	14.0549

Table 4.8: Results of the *Ansys* analyses for the different combinations of the T1100G carbon fiber with CNTs manufacturing used for the weighting method comparison.

	N	ND	ND x W	N	ND	ND x W	N	ND	ND x W	N	ND	ND x W
Carbon Fiber	T1100G	0.8	2.4	T1100G	0.8	2.4	T1100G	0.8	2.4	T1100G	0.8	2.4
Core Material	Airex	1.0	2.0	Rohacell	0.6	1.2	Gurit250	0.6	1.1	Aramid Honeycomb	0.5	1.0
Manufacturing Process	CNTs	0.3	1.5	CNTs	0.3	1.5	CNTs	0.3	1.5	CNTs	0.3	1.5
Total Mass	8.9440	0.5846	3.5076	8.2051	0.6372	3.8234	8.0817	0.6470	3.8818	5.3449	0.9782	5.8694
Front Natural Frequencies	65.3280	0.6090	0.9135	64.3980	0.6003	0.9005	64.3980	0.6003	0.9005	74.3280	0.6929	1.0394
Rear Natural Frequencies	83.9790	0.6785	1.0178	77.9960	0.6302	0.9453	80.6740	0.6518	0.9777	120.6000	0.9744	1.4616
		Total	11.3388		**Total**	10.7692		**Total**	10.7600		**Total**	13.2704

Table 4.9: Results of the *Ansys* analyses for the different combinations of the T1100G carbon fiber with hand-layup manufacturing used for the weighting method comparison.

	N	ND	ND x W	N	ND	ND x W	N	ND	ND x W	N	ND	ND x W
Carbon Fiber	T1100G	0.8	2.4	T1100G	0.8	2.4	T1100G	0.8	2.4	T1100G	0.8	2.4
Core Material	Airex	1.0	2.0	Rohacell	0.6	1.2	Gurit250	0.6	1.1	Aramid Honeycomb	0.5	1.0
Manufacturing Process	Hand-layup	1.0	6.0	Hand-layup	1.0	6.0	Hand-layup	1.0	6.0	Hand-layup	1.0	6.0
Total Mass	13.4570	0.3885	2.3312	9.6553	0.5415	3.2492	11.7298	0.4458	2.6745	9.1300	0.5727	3.4361
Front Natural Frequencies	70.3590	0.6559	0.9839	81.7660	0.7622	1.1434	81.7660	0.7622	1.1434	81.7430	0.7620	1.1430
Rear Natural Frequencies	70.5070	0.5697	0.8545	82.2090	0.6642	0.9963	71.9960	0.5817	0.8725	88.4730	0.7148	1.0722
		Total	14.5696		**Total**	14.9888		**Total**	14.1904		**Total**	15.0514

Table 4.10: Results of the *Ansys* analyses for the different combinations of the M35J carbon fiber with infusion manufacturing used for the weighting method comparison.

	N	ND	ND x W	N	ND	ND x W	N	ND	ND x W	N	ND	ND x W
Carbon Fiber	M35J	0.8	2.3	M35J	0.8	2.3	M35J	0.8	2.3	M35J	0.8	2.3
Core Material	Airex	1.0	2.0	Rohacell	0.6	1.2	Gurit250	0.6	1.1	Aramid Honeycomb	0.5	1.0
Manufacturing Process	Infusion	0.8	4.5	Infusion	0.8	4.5	Infusion	0.8	4.5	Infusion	0.8	4.5
Total Mass	7.3694	0.7095	4.2570	6.6739	0.7834	4.7006	7.0271	0.7441	4.4644	6.2327	0.8389	5.0334
Front Natural Frequencies	77.3760	0.7213	1.0820	79.1330	0.7377	1.1065	79.1330	0.7377	1.1065	86.6080	0.8074	1.2111
Rear Natural Frequencies	105.4000	0.8516	1.2774	99.4400	0.8034	1.2051	89.8780	0.7262	1.0893	116.7100	0.9430	1.4144
		Total	15.3664		**Total**	14.9623		**Total**	14.5102		**Total**	15.4089

Table 4.11: Results of the *Ansys* analyses for the different combinations of the M35J carbon fiber with CNTs manufacturing used for the weighting method comparison.

	N	ND	ND x W	N	ND	ND x W	N	ND	ND x W	N	ND	ND x W
Carbon Fiber	M35J	0.8	2.3	M35J	0.8	2.3	M35J	0.8	2.3	M35J	0.8	2.3
Core Material	Airex	1.0	2.0	Rohacell	0.6	1.2	Gurit250	0.6	1.1	Aramid Honeycomb	0.5	1.0
Manufacturing Process	CNTs	0.3	1.5	CNTs	0.3	1.5	CNTs	0.3	1.5	CNTs	0.3	1.5
Total Mass	6.0074	0.8704	5.2222	6.0354	0.8663	5.1979	6.4841	0.8064	4.8382	5.2286	1.0000	6.0000
Front Natural Frequencies	94.2400	0.8785	1.3178	102.7900	0.9582	1.4374	102.7900	0.9582	1.4374	99.6270	0.9287	1.3931
Rear Natural Frequencies	123.7700	1.0000	1.5000	111.5000	0.9009	1.3513	95.9730	0.7754	1.1631	118.5500	0.9578	1.4367
		Total	13.7900		**Total**	12.9366		**Total**	12.2887		**Total**	13.5799

Table 4.12: Results of the *Ansys* analyses for the different combinations of the M35J carbon fiber with hand-layup manufacturing used for the weighting method comparison.

	N	ND	ND x W	N	ND	ND x W	N	ND	ND x W	N	ND	ND x W
Carbon Fiber	M35J	0.8	2.3	M35J	0.8	2.3	M35J	0.8	2.3	M35J	0.8	2.3
Core Material	Airex	1.0	2.0	Rohacell	0.6	1.2	Gurit250	0.6	1.1	Aramid Honeycomb	0.5	1.0
Manufacturing Process	Hand-layup	1.0	6.0	Hand-layup	1.0	6.0	Hand-layup	1.0	6.0	Hand-layup	1.0	6.0
Total Mass	10.3421	0.5056	3.0334	9.1934	0.5687	3.4124	9.7558	0.5359	3.2157	9.3779	0.5575	3.3453
Front Natural Frequencies	90.7780	0.8463	1.2694	81.0830	0.7559	1.1338	81.0830	0.7559	1.1338	95.8330	0.8934	1.3401
Rear Natural Frequencies	91.3350	0.7379	1.1069	82.2040	0.6642	0.9963	80.8480	0.6532	0.9798	79.5700	0.6429	0.9643
		Total	15.6597		**Total**	14.9925		**Total**	14.6793		**Total**	14.8997

Table 4.13: Results of the *Ansys* analyses for the different combinations of the M60J carbon fiber with infusion manufacturing used for the weighting method comparison.

	N	ND	ND x W	N	ND	ND x W	N	ND	ND x W	N	ND	ND x W
Carbon Fiber	M60J	0.7	2.1	M60J	0.7	2.1	M60J	0.7	2.1	M60J	0.7	2.1
Core Material	Airex	1.0	2.0	Rohacell	0.6	1.2	Gurit250	0.6	1.1	Aramid Honeycomb	0.5	1.0
Manufacturing Process	Infusion	0.8	4.5	Infusion	0.8	4.5	Infusion	0.8	4.5	Infusion	0.8	4.5
Total Mass	12.9971	0.4023	2.4137	11.2527	0.4647	2.7879	11.7737	0.4441	2.6645	13.9354	0.3752	2.2512
Front Natural Frequencies	107.2700	1.0000	1.5000	81.5300	0.7600	1.1401	81.5300	0.7600	1.1401	96.6150	0.9007	1.3510
Rear Natural Frequencies	70.0770	0.5662	0.8493	87.6840	0.7084	1.0627	100.9900	0.8159	1.2239	90.9650	0.7350	1.1024
		Total	13.3630		**Total**	12.7906		**Total**	12.7285		**Total**	12.3047

Table 4.14: Results of the *Ansys* analyses for the different combinations of the M60J carbon fiber with CNTs manufacturing used for the weighting method comparison.

	N	ND	ND x W	N	ND	ND x W	N	ND	ND x W	N	ND	ND x W
Carbon Fiber	M60J	0.7	2.1	M60J	0.7	2.1	M60J	0.7	2.1	M60J	0.7	2.1
Core Material	Airex	1.0	2.0	Rohacell	0.6	1.2	Gurit250	0.6	1.1	Aramid Honeycomb	0.5	1.0
Manufacturing Process	CNTs	0.3	1.5	CNTs	0.3	1.5	CNTs	0.3	1.5	CNTs	0.3	1.5
Total Mass	10.5539	0.4954	2.9725	9.8566	0.5305	3.1828	11.4569	0.4564	2.7382	9.4126	0.5555	3.3329
Front Natural Frequencies	105.0800	0.9796	1.4694	87.1057	0.8120	1.2180	88.0340	0.8207	1.2310	89.1670	0.8312	1.2469
Rear Natural Frequencies	75.2260	0.6078	0.9117	94.3350	0.7622	1.1433	100.9430	0.8156	1.2234	104.1840	0.8418	1.2626
		Total	10.9536		**Total**	10.3441		**Total**	9.8926		**Total**	10.4424

Table 4.15: Results of the *Ansys* analyses for the different combinations of the M60J carbon fiber with hand-layup manufacturing used for the weighting method comparison.

	N	ND	ND x W	N	ND	ND x W	N	ND	ND x W	N	ND	ND x W
Carbon Fiber	M60J	0.7	2.1	M60J	0.7	2.1	M60J	0.7	2.1	M60J	0.7	2.1
Core Material	Airex	1.0	2.0	Rohacell	0.6	1.2	Gurit250	0.6	1.1	Aramid Honeycomb	0.5	1.0
Manufacturing Process	Hand-layup	1.0	6.0	Hand-layup	1.0	6.0	Hand-layup	1.0	6.0	Hand-layup	1.0	6.0
Total Mass	17.9571	0.2912	1.7470	15.1258	0.3457	2.0740	16.1256	0.3242	1.9455	19.7890	0.2642	1.5853
Front Natural Frequencies	113.5800	1.0588	1.5882	83.4580	0.7780	1.1670	83.4500	0.7779	1.1669	106.0900	0.9890	1.4835
Rear Natural Frequencies	62.5700	0.5055	0.7583	72.5450	0.5861	0.8792	91.2100	0.7369	1.1054	62.0100	0.5010	0.7515
		Total	14.1936		**Total**	13.4203		**Total**	13.4178		**Total**	12.9203

Table 4.16: Results of the weighting methods comparison for the different carbon fibers and core materials combinations.

Fiber\Core	Airex	Rohacell	Gurit 250	Aramid Honeycomb
T700S	14.69	13.24	14.13	14.03
Hexply M47	12.79	12.79	12.46	12.86
T1100G	13.87	13.17	13.25	14.05
M35J	15.37	14.96	14.51	15.41
M60J	13.36	12.79	12.73	12.30
T700S CNTs	11.53	10.69	10.35	11.39
Hexply M47 CNTs	11.90	11.91	11.07	12.92
T1100G CNTs	11.34	10.77	10.76	13.27
M35J CNTs	13.79	12.94	12.29	13.58
M60J CNTs	10.95	10.34	9.89	10.44
T700S Hand-layup	14.99	14.03	13.73	13.99
Hexply M47 Hand-layup	14.82	14.95	13.96	14.45
T1100G Hand-layup	14.57	14.99	14.19	15.05
M35J Hand-layup	15.66	14.99	14.68	14.90
M60J Hand-layup	12.69	11.92	11.92	11.42

Analyzing the previous results, it is possible to conclude that the choice of carbon fiber, core material, and manufacturing process is paramount due to its effect on the behavior of the entire structure. Consequently, every result has to be analyzed carefully, in order to understand the pros and cons of every solution. Furthermore, during this process, it was possible to verify that different material combinations retrieve different structures with different amounts of carbon fiber layers, different core thicknesses, and different carbon fiber orientations as a result of the different properties associated with the different materials.

To begin with, when observing the effect of different carbon fibers on the obtained results for the various core material/manufacturing process combinations, it is clear that the M35J carbon fiber is the one that tends to yield the best results. This fact can be explained by a combination of factors.

On the one hand, as a result of the lower modulus, T700S, Hexply M47 and T1100G carbon fibers' structures tend to be limited by the deformations. Since these fibers also present higher strength, this limitation tends to lead to oversized structures strength-wise. Thus, it becomes evident that these carbon fibers are not the most suitable, and leads us to believe that the correct carbon fiber should have higher Young's Modulus. On the other hand, due to the lower strength, the M60J carbon fiber's structures are limited by the Tsai Hill values, resulting in oversizing in the deformations criteria. Therefore, it is clear that this is also not the most suitable carbon fiber due to having low strength.

The structures using the M35J carbon fibers, however, do not have a tendency on what limits its sizing, resulting in structures ideally sized in both deformations and stresses. Consequently, it becomes evident that this is the carbon fiber that strikes the best balance

between elasticity and strength, making it the most suitable for the current structure.

Moreover, when scrutinizing the different core materials, it becomes clear that the results depend not only on the core materials themselves but also on how they interact with different carbon fibers and manufacturing processes.

Starting by analyzing the effect of foam density on the results, it is important to bear in mind that, in general, the increase in density is associated with an increase in the mechanical properties related with strength and elasticity. Therefore, the core material that yields the best result is the one that makes the best balance between the density and those mechanical properties. In general, it is possible to see that though the increase in density from Airex to Rohacell tends to yield better performance results, the same does not happen from Rohacell to Gurit250. With this in mind, it is possible to see that performance-wise, the core material that tends to make the most suited one is the Rohacell.

This increase in performance, however, is accompanied by a huge increase in price, with the total cost of Airex being around 1.7 times less than the total cost of Rohacell. Comparing the final results, it is clear that the benefits in performance do not outweigh the drawbacks in cost. Therefore, and considering that Rohacell and Gurit250 have similar costs, Airex seems to be the overall best foam solution.

Upon analyzing the results obtained using Aramid Honeycomb as the core material, it is possible to see that the results obtained in performance are consistently better than those obtained with other core materials, independently of the manufacturing process and of carbon fiber. To understand these results we have to compare the mechanical properties of the Aramid Honeycomb to the ones of foams. Firstly, it is clear to see that Aramid Honeycomb is the one with the lower density. However, regarding the elasticity and strength, the foams tend to present better properties. Thus, in order to achieve better performance results, Aramid Honeycomb has to present better balance of density, strength and elasticity.

On the other hand, when comparing the final comparison results, structures with Aramid Honeycomb as the core material, not always present better results than the structures with Airex. These results can be explained by the higher total cost of Aramid Honeycomb compared to the foams.

Upon analyzing the overall results, it is possible to conclude that in every combination of carbon fiber and manufacturing process, the one that yields the best total results is either Airex or Aramid Honeycomb. Just as aforementioned, the superiority of Airex results is easily understandable, due to it being the most cost-effective material, outweighing the performance disadvantages. The results obtained using Aramid Honeycomb, on the other hand, can be explained by the performance advantages that are sufficiently superior, compensating for the higher cost disadvantage.

Finally, it is possible to conclude that the choice of the manufacturing process has a ma-

jor impact on both the mass and the natural frequencies of the structure. Concerning the mass criterion, in most cases, the introduction of CNTs into the structure leads to a reduction in mass that can reach values of up to 32.5% compared to the values obtained with infusion/Autoclave manufacturing. This huge reduction can be especially seen on carbon fibers that tend to have higher safety factors in either deformation and strength, as a result of the increase in of the mechanical properties. This tends to result in a bigger balance of strength and elasticity, reducing the safety aforementioned factors.

Regarding the variations in natural frequencies, it is noticeable that these vary significantly from case to case, with substantial increases in some cases and slight decreases in others. These variations, considering they are not consistent, cannot be considered neither an advantage nor a disadvantage and will have to be considered individually.

Combining the effects on performance with the increased complexity of the manufacturing process leads to a scenario where the benefits in performance do not outweigh the drawbacks in manufacturing complexity of this choice. Therefore, for the current case, it is clear that there is no need for further investigation using this manufacturing process. This conclusion, however, could be completely different if the manufacturing complexity was not a major concern, as it leads to big performances increases.

On the other hand, the use of hand-layup as the manufacturing process tends to yield opposite results: in general, the mass of the structure experiences a slight increase, while the natural frequencies tend to decrease. As expected, the significant reduction in mechanical properties, even if only slightly, results in a bobsleigh with inferior performance. However, this performance decline is counterbalanced by a substantial reduction in the complexity of the manufacturing process.

When considering both the pros and cons of the hand-layup manufacturing process, it becomes evident that the final results used for comparison tend to be similar to those obtained from the infusion and Autoclave manufacturing processes, and in some cases, even better. Therefore, this manufacturing process has to be considered for future analyses.

When comparing the infusion process with the Autoclave process, even though they are based on similar carbon fibers, it is evident that they result in different structures and in different results. On the one hand, when comparing masses (except in the case where Rohacell is used as the core material), the infusion manufacturing process leads to smaller masses, thereby achieving better results on this particular criterion. On the other hand, when examining the results obtained for natural frequencies, it becomes apparent that while Autoclave tends to yield better results for the rear part, it is the infusion process that leads to higher natural frequencies in the front part. Considering these results and taking into account the more complex manufacturing process, it appears that Autoclave manufacturing is a less effective process.

In conclusion, after analyzing the results presented in Table 4.16, it becomes evident that the three combinations yielding the best results are as follows: M35J/Airex/Hand-layup;

M35J/Aramid Honeycomb/Infusion; and M35J/Airex/Infusion. Consequently, for the next geometries, these are the combinations that will be studied.

4.2 Final Results

Bearing the results presented in Section 4.1 in mind, the final geometry, presented in Section 3.1, was imported to *Ansys*. There, the best material combinations were tested and the respective structures were developed, and, using the method presented in Subsection 3.6, iteratively optimized. In this Section the obtained results are presented and discussed.

4.2.1 Comparison Results

The process of developing the structure started by analyzing the different material combinations and comparing the results obtained for each combination. In order to compare these, the comparison of the weighting methods, presented in Section 3.5, was once again used. In it, to turn the Natural Frequencies and Total Mass results into non-dimensional values, only the results attained with the final geometry were considered, as different geometries have different structural characteristics. The obtained results were compiled into Tables 4.17 and 4.18.

Table 4.17: Results of the *Ansys* analyses for the final combinations used for the weighting method comparison.

	N	ND	ND x W	N	ND	ND x W
Carbon Fiber	M35J	0.75	2.25	M35J	0.75	2.25
Core Material	Airex	1	2	Aramid Honeycomb	0.5	1
Manufacturing Process	Infusion	0.75	4.5	Infusion	0.75	4.5
Total Mass	14.6744	0.8412	5.0472	12.3442	1.0000	6.0000
Front Natural Frequencies	42.3680	1.0000	1.5000	42.0130	0.9916	1.4874
Rear Natural Frequencies	77.9580	0.8963	1.3444	86.9790	1.0000	1.5000
		Total	16.6417		**Total**	16.7374

Table 4.18: Results of the *Ansys* analyses for the final combinations used for the weighting method comparison (Continuation).

	N	ND	ND x W
Carbon Fiber	M35J	0.75	2.25
Core Material	Airex	1	2
Manufacturing Process	Handlayup	1	6
Total Mass	19.8980	0.6204	3.7222
Front Natural Frequencies	33.9340	0.8009	1.2014
Rear Natural Frequencies	65.3960	0.7519	1.1278
		Total	16.3014

In order to evaluate the presented results, it is important to divide them into two: the results regarding accessibility to the materials and manufacturing processes, and the results related to the performance.

On the one hand, the results regarding exclusively the material choice are the same as the ones presented in Section 4.1. Therefore, it is clear that the combination of materials that is the most accessible is the one with hand-layup manufacturing and Airex core material, as a result of using the most accessible core material and manufacturing process. On the other end of the scale, the one that is the least accessible is the one containing Aramid Honeycomb core and infusion manufacturing, as a result of the less accessible manufacturing process and more expensive core material.

On the other hand, the results related to the performance of the bobsleigh, i.e., the Natural Frequencies and the Total Mass, depend on the developed structure and how the selected materials perform on it. Therefore, it is clear that these are not the same as the ones presented in Section 4.1. Thus, these must be analyzed carefully.

To begin with, when comparing the current performance-related results to the preliminary ones, it is possible to see that these have worsened, by increasing the Total Mass and reducing the Natural Frequencies. This fact can be easily explained by the new bobsleigh geometry. When comparing the two geometries, it was possible to conclude that the newer one had a 30% larger wetted area, by increasing the section area in the transversal division region. Furthermore, the newer geometry presented a different bumper and rear part geometries.

On the one hand, the increase in wetted area is clearly one of the reasons behind the increase in mass, as a result of more material used. Furthermore, increasing the section area in the transversal division region led to a reduction in geometric rigidity. Therefore, it is predictable that the structure had to be more reinforced than the preliminary one. The combination of reducing the geometric rigidity and increasing the mass has led to a reduction of the natural frequencies range.

On the other hand, the bumpers on the new geometry presented a larger span, but a smaller mean chord, when compared to the ones from the preliminary geometry. This combination has resulted in a smaller geometric rigidity, being, most likely, the reason behind the bigger reduction in natural frequencies in the front part than in the rear part.

For the particular case of the rear end geometry, in an attempt to produce a more teardrop-like shape, the final geometry presented a more tapered rear-end design. As a result, the loads applied during the push-off phase, on the push handles, were no longer aligned with the cowling. This resulted in a need to reinforce more the rear part of the structure in order to withstand these loads. This bigger structural reinforcement and the wetted area increase, consequently, led to a higher mass and a reduction in natural frequencies of the rear part.

Analyzing the previous changes in geometry, and consequent changes in performance-related results, arises the question of whether or not these have changed to a point where the materials selected are no longer the most suited ones. With this in mind, it becomes paramount to compare the ratios between results using different material and manufac-

turing process combinations.

To begin with, when comparing the preliminary results with Airex core material and Infusion manufacturing to the ones with Aramid Honeycomb core material and Infusion manufacturing, on the preliminary geometry, the former presented a Total Mass 18.24% higher, Front Natural Frequencies 10.66% lower and Rear Natural Frequencies 9.69% lower than the latter. On the new geometry, however, the structure containing Airex core material and Infusion manufacturing presented a Total Mass 18.88% higher, Front Natural Frequencies 0.84% higher, and Rear Natural Frequencies 10.37% lower than the latter. Observing these results, it is clear that the ratios between Rear Natural Frequencies and Total Mass are quite similar.

The results on Front Natural Frequencies, however, are not similar. This change can be explained by a combination of factors. To begin with, on the newer geometry, the limiting sizing factor was the stress, not the deformations, as will be seen in Subsection 4.2.2. With this in mind, the structure with Airex core material and Infusion manufacturing had to have a bigger reinforcement than the one with Aramid Honeycomb core. This bigger reinforcement, most likely, led to the higher Front Natural Frequencies.

On the other hand, when comparing the preliminary results with Airex core material and Hand-layup manufacturing to the ones with Aramid Honeycomb core material and Infusion manufacturing on the preliminary geometry, the former presented a Total Mass 65.93% higher, Front Natural Frequencies 4.81% higher and Rear Natural Frequencies 21.74% lower than the latter. On the new geometry, however, the structure containing Airex core material and Hand-layup manufacturing presented a Total Mass 61.19% higher, Front Natural Frequencies 19.23% lower, and Rear Natural Frequencies 24.81% lower than the latter. Observing these results, it is clear that the ratios between Rear Natural Frequencies and Total Mass are quite similar, just as has happened in the previous comparison.

However, the results on Front natural frequencies are not similar, yielding a ratio below the one achieved during the preliminary tests. This fact could be associated with two different reasons. Firstly, during the development using the Hand-layup combination, unlike the other combinations, there was a need to reinforce the structure close to the bumpers' caps. This reinforcement leads to an increase in inertia that could be responsible for this reduction. Another reason behind this decrease in ratio could be the new geometry, where the materials' strength is more important than the stiffness. Considering the front part of the structure had its sizing limited by its strength, not stiffness, the front part of the structure on the new geometry was lighter than the old one. Therefore, it can be supposed that increasing the strength of the front part would result in higher natural frequencies, but also, higher mass.

Bearing these previous results and discussion in mind, it is possible to conclude that, overall, regarding the Total Mass and the rear part Natural Frequencies results, the materials

selected as the most suitable in the preliminary tests, continue to be suitable for the newer geometry. This, however, cannot be said for the results regarding the front part, as the ratios between Natural Frequencies of the different combinations completely changed with the introduction of the newer geometry. As mentioned, and as will be seen in Subsection 4.2.2, the limiting factor in the sizing of the front part was the strength of the materials, not the stiffness. Therefore, it raises the question of whether the use of materials with higher strength and lower Young's Modulus would yield better performance results.

When combining the results regarding accessibility to the materials and manufacturing processes and the results related to the performance, it becomes evident that the combination that retrieves the best comparison results is the one with Aramid Honeycomb and Infusion manufacturing. Considering that this combination is the one with the worst results regarding accessibility, it is clear that the performance advantages outweigh the disadvantages in accessibility. On the other hand, considering that the one with hand-layup manufacturing and Airex core material is the most accessible, it is clear that the accessibility advantages do not outweigh the performance disadvantages.

In conclusion, after analyzing the results presented in Table 4.18, out of the tested combinations, the one consisting of M35J/Aramid Honeycomb/Infusion manufacturing is the most suitable for the structure being developed, as it was the one yielding the best comparison results. Therefore, this material and manufacturing combination is the selected one and is the one that will be presented in detail for the rest of this thesis.

4.2.2 *Ansys* Results

Bearing in mind the conclusions reached previously, in the current Subsection, the results obtained in *Ansys* for the final material combination and for the different loading conditions are presented. For each loading condition, the results for the deformation and safety factors are presented, as these are the two design constraints that the structure has to comply with.

To begin with, we start by analyzing the results for the high accelerations loading case, presented in Figures 4.1 through 4.4. Contrary to what could be thought, the current loading condition is not a critical one, presenting low deformations and high safety factors on the final structure.

Starting by analyzing the results achieved for the rear part, in Figures 4.1 and 4.2, it is clear that these are not close to the limits imposed in Subsection 3.3.5. Regarding the deformations, the maximum value is of 0.014 mm, in a point right behind the brake cut-out. This location can be easily explained by the placement of a point mass in this area to simulate the mass distribution of the brakeman that during the race sits in this region. The remaining structure has negligible deformations due to this not being a critical loading scenario and due to the fixed supports applied to the structure. Regarding the stress

distribution over the rear part, as could be expected, the lower safety factors are seen near the region where the point mass is located, with safety factors in the remaining structure tending towards infinity, due to the low-existent stress.

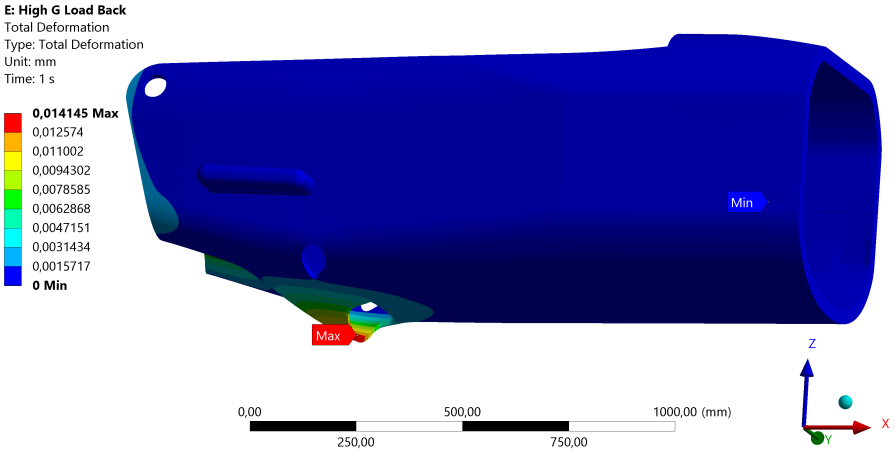

Figure 4.1: Deformation analysis results of the rear part's structure under high accelerations on *Ansys*.

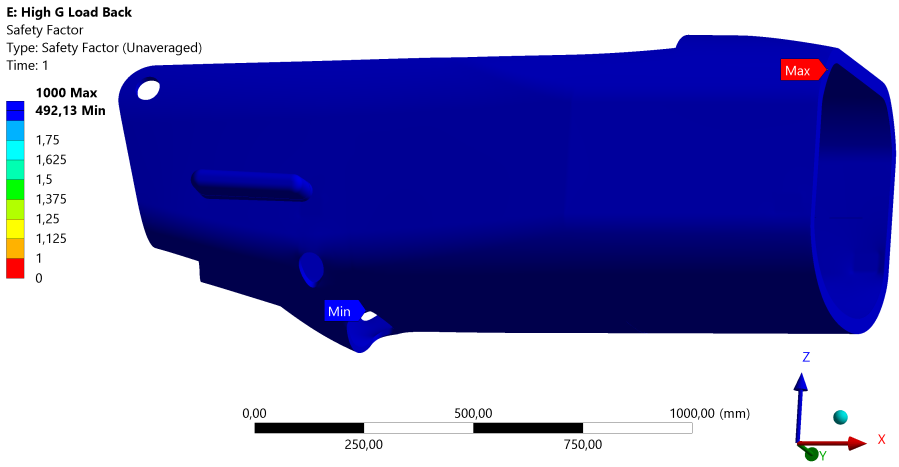

Figure 4.2: Safety factor analysis results of the rear part's structure under high accelerations on *Ansys*.

Regarding the front part, presented in Figures 4.3 and 4.4, it is clear that the conclusions inferred for the rear part are still applicable, as the values achieved in this analysis are not close to the established limits. Starting by examining the values of deformation, it is possible to see that the maximum value is 0.0016 mm and is achieved in the top cover support. The deformations in this region are a result of the mass point applied, in order to simulate the front cover. Despite what was expected, it is possible to see that the maximum deformation is not downward-directed but upwards. This fact can be explained by the combination of the acceleration in the different directions. With regards to the stress result, it is possible to see that the minimum safety factor has a value of 969.37 and is reached also in the connection between the cowling and the top cover. This fact is, once again, a result of the distribution of the forces from the point mass applied in this region.

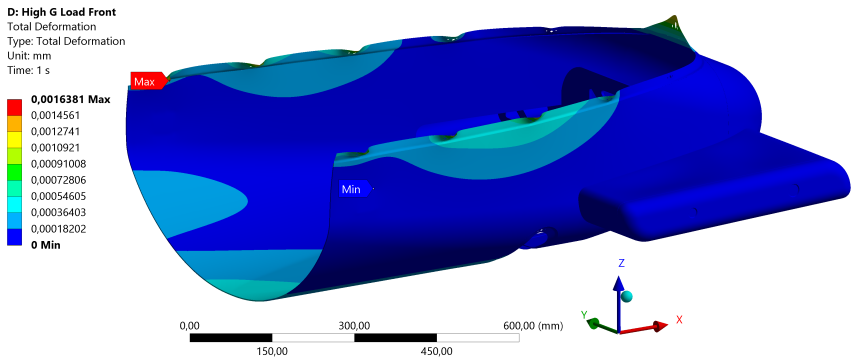

Figure 4.3: Deformation analysis results of the front part's structure under high accelerations on *Ansys*.

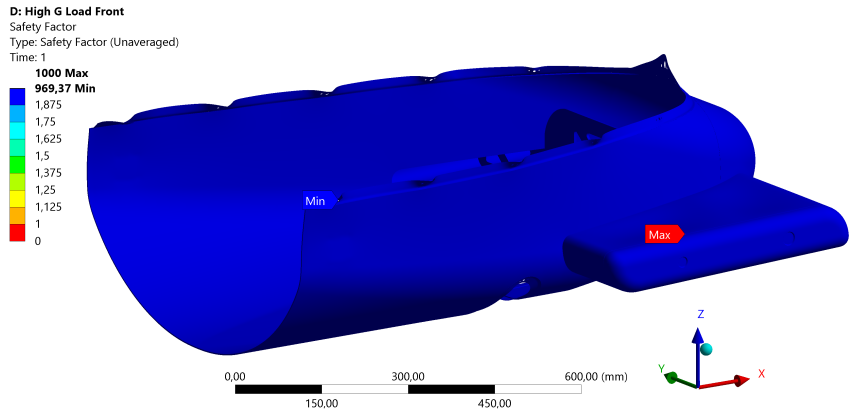

Figure 4.4: Safety factor analysis results of the front part's structure under high accelerations on *Ansys*.

Passing on to the loading case related to the push-off phase, presented in Figures 4.5 and 4.6, it is clear that this is a critical condition for the rear part, as it limits the laminate used in this region. It is important to note that this loading condition is not, however, critical for the front part as the loads applied during this push phase are all applied in the rear part, and, due to the transversal cowling division, no load is applied directly to the front part's cowling. As a result, no result will be presented regarding the front part under this loading condition.

Regarding the deformations, shown in Figure 4.5, as a result of applying loads in the push handles and in the push bar, it is clear that these are the two regions where the deformations achieve the maximum values. In the region where the push bar connects to the cowling, there is a deformation mainly in the vertical z direction and the longitudinal x direction, as a result of the loads applied, which are in these two directions. In the region of the push handles, however, it is possible to see that the structure deforms mainly in the transversal y direction, despite having no load applied in this direction. This fact is a consequence of the newer geometry, where the rear end of the rear part tappers in a tear-shaped design, having the forces not lined up with the cowling's walls. This newer geometry, under the current loading conditions, results in the buckling of the cowling.

In order to comply with the established deformation limits of 2 mm, this region had to present a major reinforcement.

Concerning the results of safety factors, presented in Figure 4.6, once again it limits the sizing of the rear part structure. However, in this case, it only limits the sizing in the region of the connection between the push bar and the cowling, where the safety factor is close to the imposed limit, with a value of 1.2622. On the remaining structure, the safety factor is higher and the limiting factor is not the strength, but the elasticity of the material. This can be especially seen in the rear end of the structure where the deformations are close to the imposed deformation limit, but are not close to the safety factor limit.

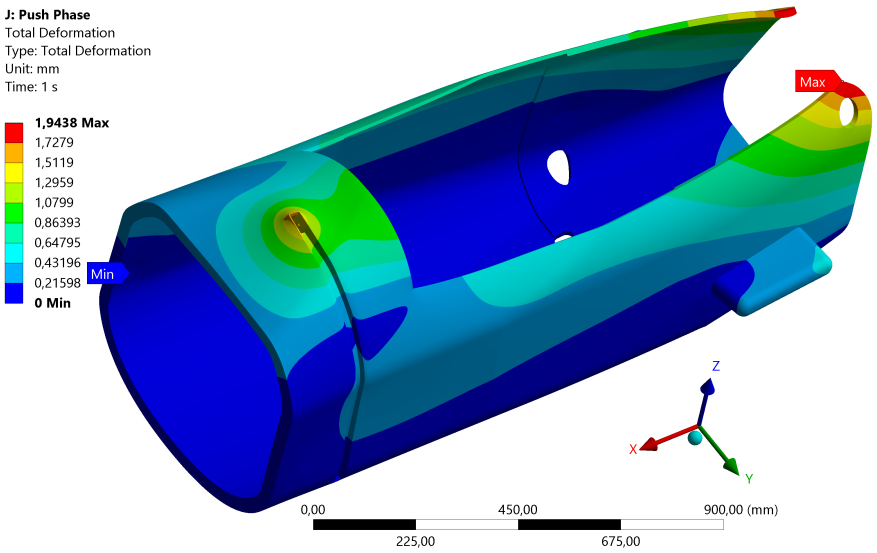

Figure 4.5: Deformation analysis results of the rear part's structure under push loads on *Ansys*.

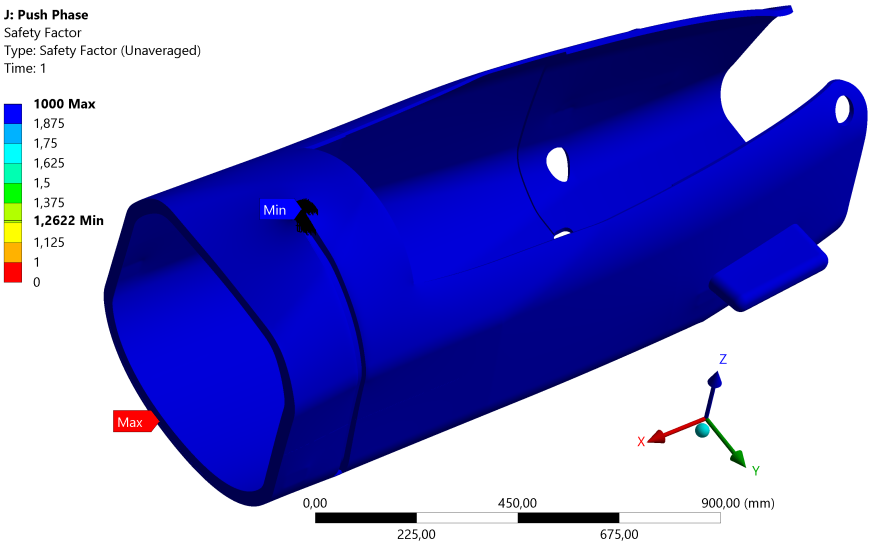

Figure 4.6: Safety factor analysis results of the rear part's structure under push loads on *Ansys*.

Proceeding to the impact loading conditions, represented in Figures 4.7 through 4.10, this is, in fact, a critical condition, limiting the sizing of the structure. This fact can be seen by the results regarding the safety factor, where the values reached are close to the limits imposed in Subsection 3.3.5.

Starting by analyzing the results obtained for the rear part, in Figure 4.9, the maximum deformation reached has a value of 1.8241 mm. With this in mind, it is clear that the reinforcement used in order to comply with the deformation limit in the push loading case has resulted in an oversized structure with regard to the impact loading case, yielding a total deformation much lower than the limit established for this loading condition.

In relation to the safety factor, as seen in Figure 4.10, it is important to note that the lower safety factor is 1.2695 in the bumpers. On the remaining structure, the safety factor is much bigger than the aforementioned value. Bearing this in mind, we can conclude that, on the current geometry, this analysis serves as a way to size the bumpers and their connection to the cowling, but has no effect on the remaining structure's sizing.

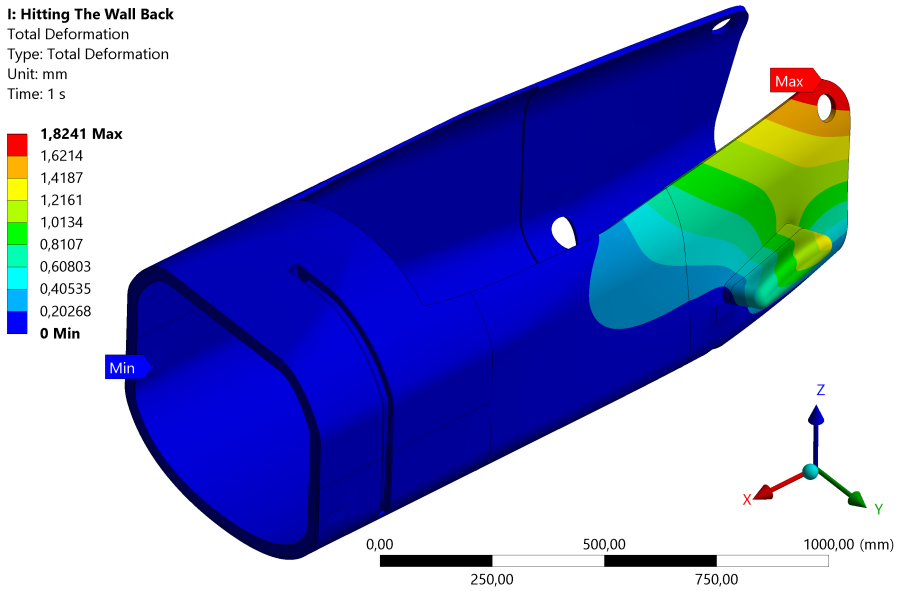

Figure 4.7: Deformation analysis results of the rear part's structure under impact loads on *Ansys*.

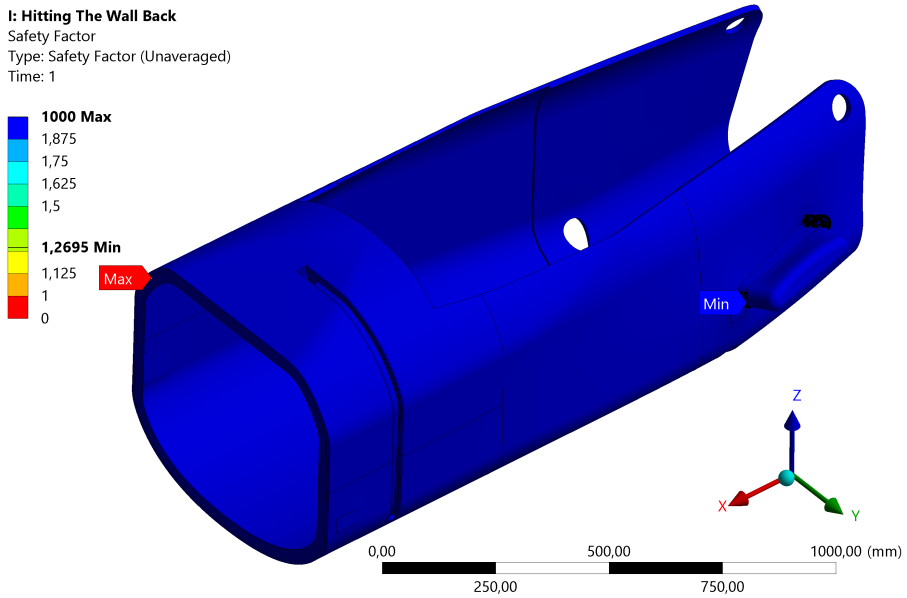

Figure 4.8: Safety factor analysis results of the rear part's structure under impact loads on *Ansys*.

Analyzing the results obtained for the front part, presented in Figures 4.9 and 4.10, it is clear that this loading case is critical in the sizing of this part of the structure, yielding values of deformation of up to 0.87243 mm and a minimum safety factor of 1.2529. Starting with the results of deformation, it is noted that the highest deformation reached is in the bottom cover support, as a result of the opening in the structure, reducing the rigidity of the structure in this area. However, it is paramount to note that the maximum deformation is not close to the limit established, as a consequence of the fact that this part is not being sized in accordance with the elasticity of the material, but to its strength.

In relation to the safety factor distribution over the structure, as mentioned, this is the sizing limit. Thus, the presented values are closer to the established limit in the bumpers and in the spar. Throughout the front part cowling, the values of the safety factor tend to be bigger than the limits established this part had to be sized in order to increase the Natural Frequencies of the front part, so as to withstand the vibrations it will face during a normal run.

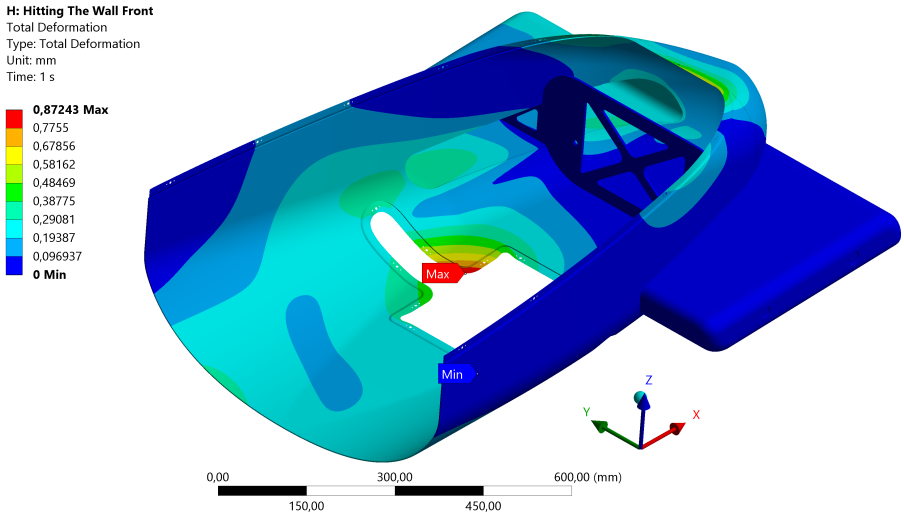

Figure 4.9: Deformation analysis results of the front part's structure under impact loads on *Ansys*.

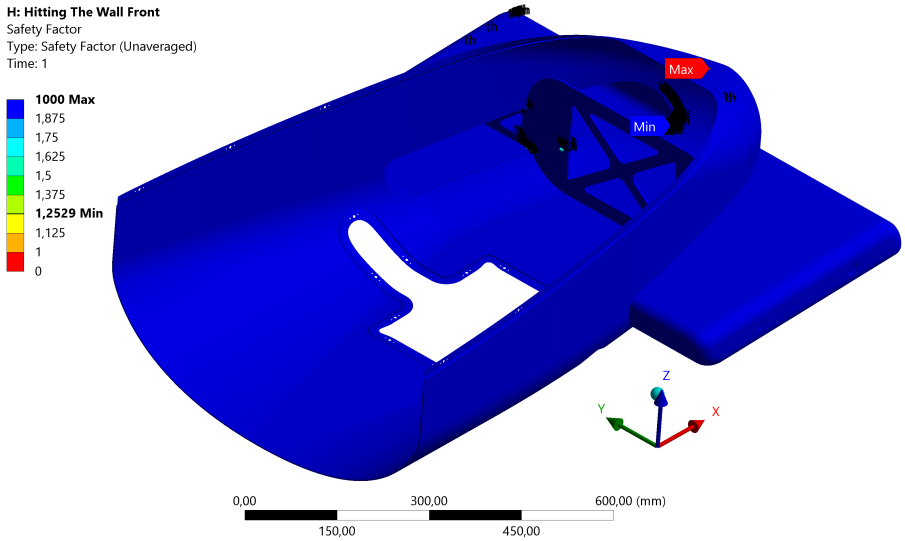

Figure 4.10: Safety factor analysis results of the front part's structure under impact loads on *Ansys*.

Finally, in *Ansys*, the natural frequencies were also evaluated, due to the importance of vibration absorption to the bobsleigh performance. To do so, using Modal Analyses the lower six natural frequencies were obtained for both the front and rear parts and the obtained results are shown in Table 4.19. Considering the lower natural frequencies obtained are out of the range of frequencies the bobsleigh will face during a normal run, we can ensure the safety of the bobsleigh in all phases. In order to evaluate the impact these have on the performance of the bobsleigh, only the lowest value was analyzed in Subsection 4.2.1, as it gives an insight into how the structure is able to deal with the vibrations it might face.

Table 4.19: Natural Frequencies analysis results for the front and rear parts of the structure obtained in *Ansys*.

Front Part [Hz]	Rear Part [Hz]
42.013	86.979
61.336	91.142
79.484	100.44
84.314	143.29
114.97	155.90
115.03	202.22

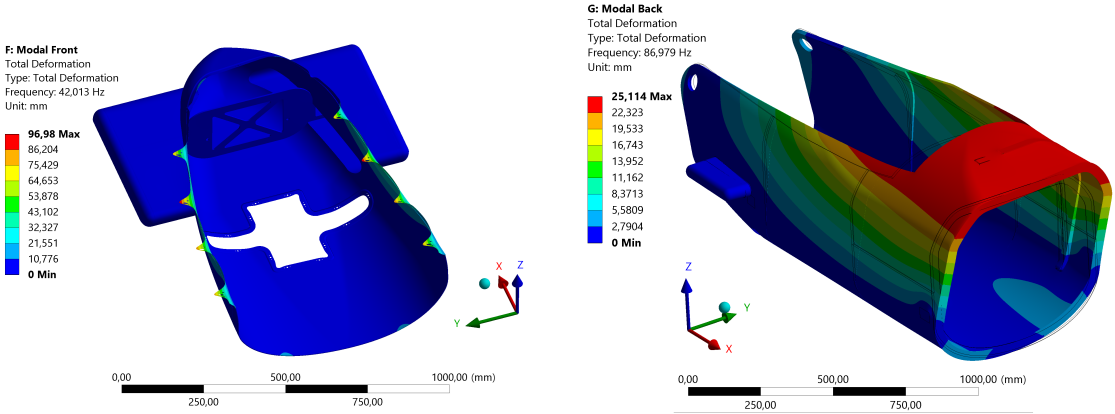

(a) Front Part First Vibration Mode. (b) Rear Part First Vibration Mode.

Figure 4.11: Front and Rear Parts' First Vibration Mode.

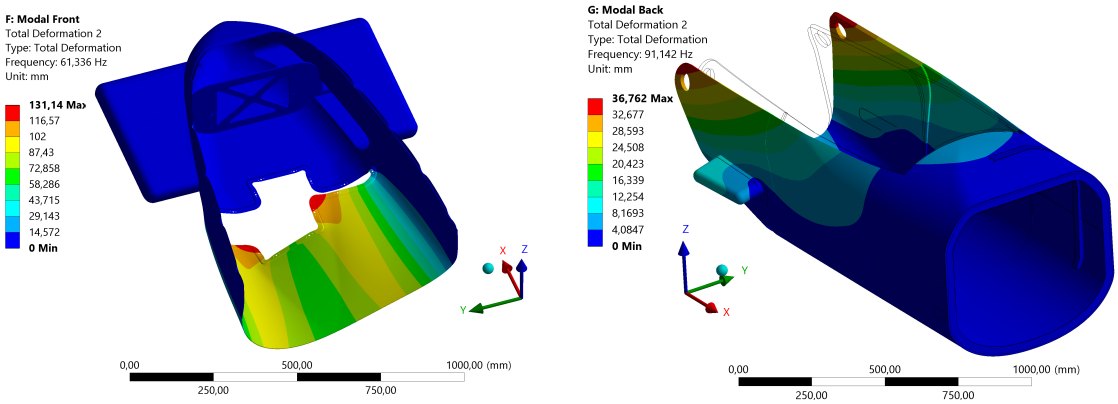

(a) Front Part Second Vibration Mode. (b) Rear Part Second Vibration Mode.

Figure 4.12: Front and Rear Parts' Second Vibration Mode.

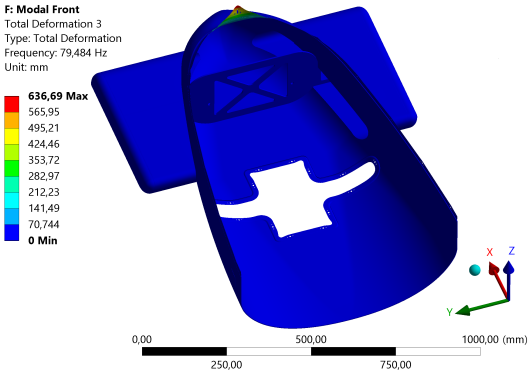

(a) Front Part Third Vibration Mode.

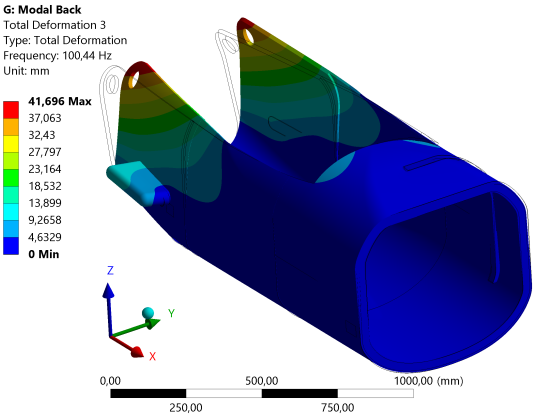

(b) Rear Part Third Vibration Mode.

Figure 4.13: Front and Rear Parts' Third Vibration Mode.

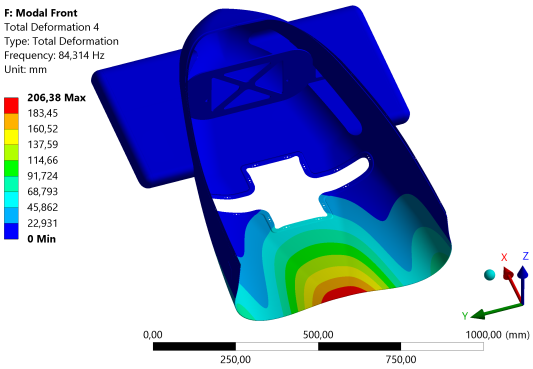

(a) Front Part Fourth Vibration Mode.

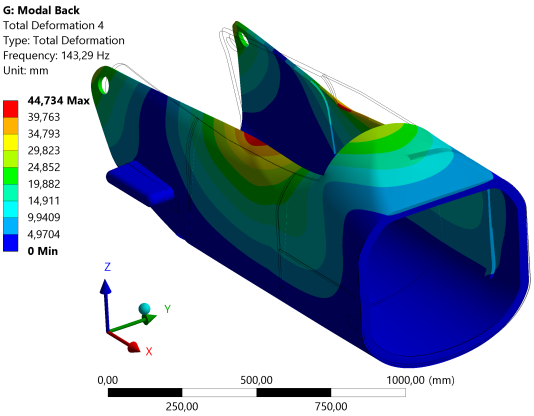

(b) Rear Part Fourth Vibration Mode.

Figure 4.14: Front and Rear Parts' Fourth Vibration Mode.

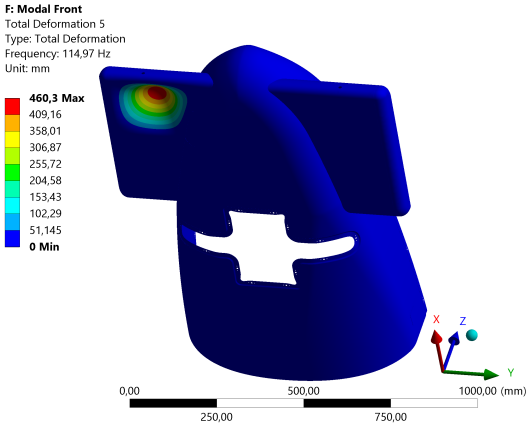

(a) Front Part Fifth Vibration Mode.

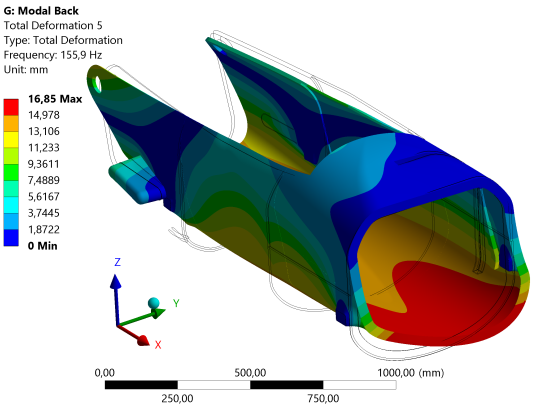

(b) Rear Part Fifth Vibration Mode.

Figure 4.15: Front and Rear Parts' Fifth Vibration Mode.

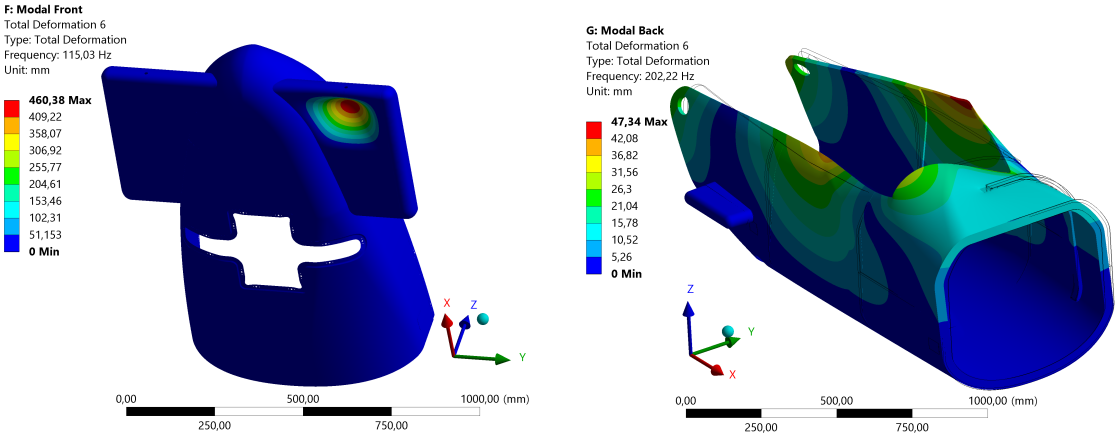

(a) Front Part Sixth Vibration Mode.

(b) Rear Part Sixth Vibration Mode.

Figure 4.16: Front and Rear Parts' Sixth Vibration Mode.

4.2.3 Mesh Independence

In order to verify the validity of the previous results, it is important to understand whether the results obtained are mesh independent or not, i.e., whether the use of a more refined mesh would yield different results or not. To do so, the developed structure was tested with different meshes, with different mesh element sizes, and the results obtained were registered in Figures 4.17 through 4.19.

Firstly, analyzing the results presented in Figure 4.17 regarding the deformations, it is clear that the deformations results of the push phase and of the impact on the rear part analyses have converged. In fact, when comparing the results obtained with the last two meshes, it was possible to see there was a change of just 0.85% and 0.62%, respectively. As a result, these results can be considered as mesh independent, and can be considered for the structural development.

On the other hand, there is no clear convergence of results for the impact on the front part. Comparing the results for the two meshes with more elements, there is a change of around 3.72%. This change shows that this result might change if using a finer mesh. As a result, the value obtained cannot be considered as mesh independent. However, bearing in mind that for this analysis the deformation limit established was of 5 mm, we can infer that the limit will be complied regardless of the mesh used.

Analyzing the results obtained regarding the safety factor, in Figure 4.17, it looks as if they converged when using finer meshes. However, when comparing the results of the two finer meshes, it is possible to see that for the push phase results there was a change of 4.06%, for the impact loads on the front part there was a change of 1.68%, and for the impact loads on the rear part there was a change of 6.10%. These changes, specially the ones on the rear part, show that the results might have not converged and these results have to be taken carefully, and the use of a finer mesh would be advised. This, however,

was not possible as finer meshes consume higher computational resources than the ones available for the development of the current thesis. With this in mind, the results obtained for the finer mesh were the ones considered, as, in theory, this should be the ones closer to the real ones.

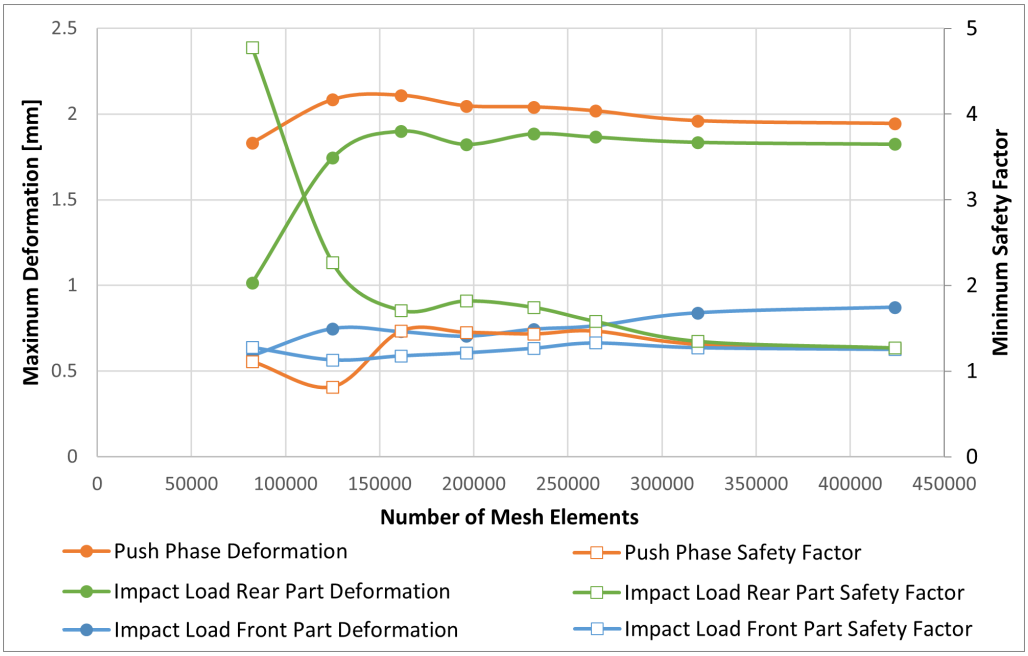

Figure 4.17: Safety factor and deformation results of the structure under push and impact loads obtained in *Ansys* for meshes with increasingly smaller elements.

Moving on to the analysis of the results regarding the high acceleration loads, as presented in Figure 4.18, it is clear that the deformation results, with the use of an increasingly finer mesh, do converge. In fact, when comparing the results obtained with the use of two the meshes with more elements, there was just a change of 0.93% on the front part, and a change of 0.57% on the rear part. With these values in mind, we can conclude that these results are mesh independent, and can be used for the sizing of the structure, as it will remain within the established limits, regardless of the mesh used.

However, when analyzing the results of safety factors for the different meshes, we can clearly see, there is no convergence of results. Indeed, the use of finer meshes tend to yield increasingly bigger safety factors. In light of this, these results can still be used, despite not being mesh independent, as the increase in safety factor ensures a higher margin of safety in our analyses. Furthermore, considering these results are not critical for the sizing of the structure, as explained in Subsection 4.2.2,the increasing safety factors do not, in any way, affect the structure.

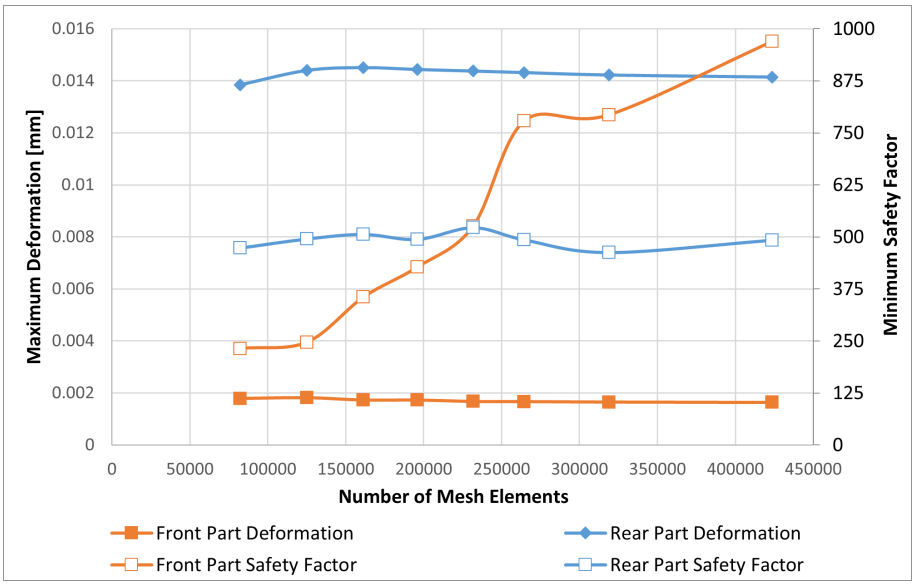

Figure 4.18: Safety factor and deformation results of the structure under high acceleration loads obtained in *Ansys* for meshes with increasingly smaller elements.

When analyzing the results obtained with regards to the lowest natural frequency of the structure, as presented in Figure 4.19, it is possible to conclude that these results do converge when using higher meshes. Essentially speaking, when comparing the two results obtained using the two finer meshes, for the front part there was just a change 0.03% and for the rear part there was a change of 0.85%. Considering these results can impact not only the performance and safety of the structure, but also the material choice, being part of the comparison criteria, this convergence of results is paramount for the current thesis.

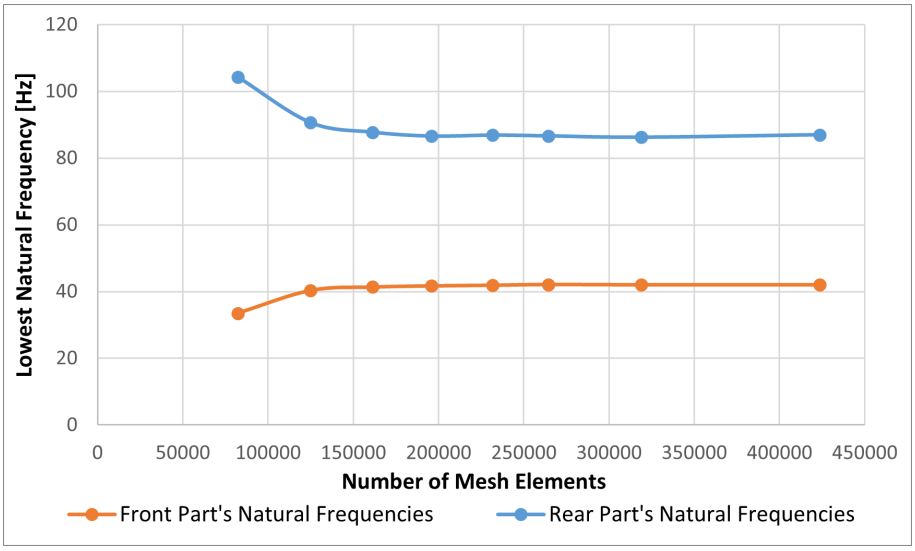

Figure 4.19: Structure's Natural Frequencies obtained in *Ansys* for meshes with increasingly smaller elements.

As a result of the computational power limitation, as already stated, there is a need to consider for further result analysis, the finer mesh obtained. This mesh has a total of 426990

nodes and 420626 elements. To evaluate the quality of the current mesh, three quality parameters have been used:the Aspect Ratio; the Orthogonal Quality and the Skewness.

The first parameter evaluates the ratio between the long side of an element to its short side, varying in value from 1 to infinity. In general, smaller values tend to represent better mesh quality, attaining more realistic results [62]. In this particular parameter, it was possible to see an average aspect ratio of 1.1196, with a minimum value of 1 and a maximum value of 9.3237.

The second parameter evaluates how close to ideal an element is. In the case of triangular elements how close they are to an equilateral triangle, and in the case of a quadrilateral element, how close it is to a square. This parameter varies in value from 0 to 1, where 0 represents and ideal equilateral element, and 1 represents a degenerate element. Therefore, the smaller the parameter value, the higher the quality [62]. The used mesh has presented a Skewness average of $9.115e^{-2}$.

Finally, the Orthogonal Quality parameter takes into consideration several mesh geometry parameters and returns a quality value in the 0 to 1 range, where values closer to 1 represent a higher overall quality of the elements used in the mesh [62]. In the particular case of the mesh used, it was attained an average of 0.98269 in Orthogonal Quality.

Bearing the previous results in mind, despite not having converged in all the results, it is possible to assume that the mesh used presents a good quality.

4.2.4 Final Laminate Layup

Having verified the mesh independence of the results presented, it is important to present the final structure, the laminates used, the interfaces between the different parts, and the important features of these different parts. Regarding the front part of the structure, the laminates used are presented in Figure 4.20 and Table 4.20, whereas the laminates used on the rear part are presented in Figure 4.21 and Table 4.21. As previously explained, the materials used are M35J carbon fiber and Aramid Honeycomb core. Therefore, the final layups are presented using only the orientations and total core thickness, not the materials.

Starting by analyzing the laminate used in the Front Part structure, is divided into 7 different parts: **Front Part 1**, the most forward part of the fuselage; **Front Part 2**, the remaining part of the fuselage; the **Top & Bottom Cover Support**, the connection parts between the fuselage and the top and bottom covers; the **Front Bumpers**; the **Front Bumper Caps**; **Spar 1**, the central part of the Spar; and **Spar 2**, the remaining spar structure.

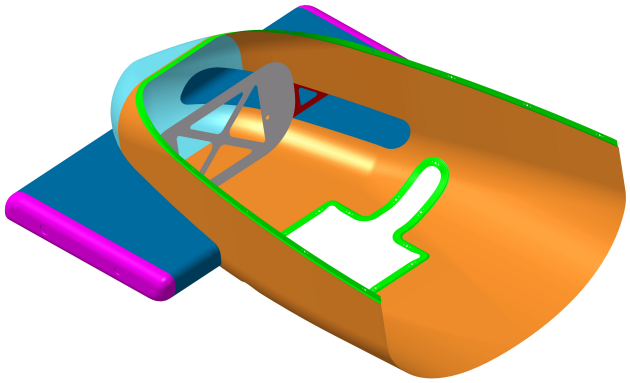

Figure 4.20: Visualization of different laminate zones with distinct colours for each part, highlighting the composite material arrangements on the front part structure.

Table 4.20: Specification of composite material orientations, layer counts, and core total thickness for each laminate zone on the front part structure.

Part	**Colour**	**Top Layer**	**Core Total Thickness [mm]**	**Bottom Layer**
Front Part 1	Light Blue	(0/90/0)	-	-
Front Part 2	Orange	(90/0)	2	(0)
Top & Bottom Cover Support	Green	(90/0)	-	-
Front Bumpers	Dark Blue	$(0/90)_S$	-	-
Front Bumper Caps	Pink	$(0/90)_S$	-	-
Spar 1	White	$(0/90)_{18}$	-	-
Spar 2	Red	$(0/90)_8$	-	-

Bearing this structure division in mind, it is important to discuss the laminates used. When analyzing the laminates used in the fuselage structure, it is paramount to note that the laminate used in Front Part 1 coincides with the laminate of Front Part 2, without the Aramid Honeycomb core. Considering the introduction of the core was done in order to increase the natural frequencies, it could be supposed it should be applied to the whole fuselage. However, the curvature in the Front Part 1 does not allow a correct placement of the core, justifying the its absence in this part. To account for this fact, Front Part 1 extends until a section 180 mm from the nose of the bobsleigh.

As for the Top & Bottom Cover Support, it serves the function of connecting the top and bottom covers to the fuselage, having a curvature that accounts for their placement without introducing unevenness to the geometry, so as to not affect the aerodynamic performance of the bobsleigh. With regards to the laminate used, it is clear that it is the same as the Top Layer of Front Part 2. Bearing the previous considerations in mind, we can conclude that these previous three different parts, i.e., Front Part 1, Front Part 2, and Top & Bottom Cover Support, can be built together as a continuous part. The connection between the covers and the fuselage is made through a bolted connection using a two lug platenut fixed to the Top & Bottom Cover Support and AN3 steel bolts.

With respect to the Front Bumpers, these also present the same laminate as the Top Layer of Front Part 2. As a result, these can also be considered as a continuation of the fuselage structure, as the laminate is the same. The Bumper Caps then connect to the Front Bumpers through bolted connections. These bolted connection are made through the use of AN4 steel bolts.

Finally, the spar structure is divided into two, where the Spar 2, the most outward part of the spar, is the foundation for the spar laminate. The Spar 1 structure, the most central part, takes this foundation to the next level by reinforcing it with additional layers. These extra layers serve to enhance the structural integrity, in order to withstand the loads applied to this structure. The connection of the spar to the bumpers and to the fuselage structure will be made through the use of an adhesive interface with Epoxy.

Proceeding to analyze the rear part of the structure, is divided into 8 parts: the **Former** located in the transversal cowling division; the **Push Bar**, located on the left side of the structure; **Rear Part 1**, the top part of the most forward part of the structure; **Rear Part 2**, below Rear Part 1; **Rear Part 3**, the middle part of the fuselage structure; **Rear Part 4**, located at the rear end part of the structure; **Rear Bumper Root**, the part of the bumper that connects to the fuselage; **Rear Bumper Tip**, the tip portion of the bumper structure.

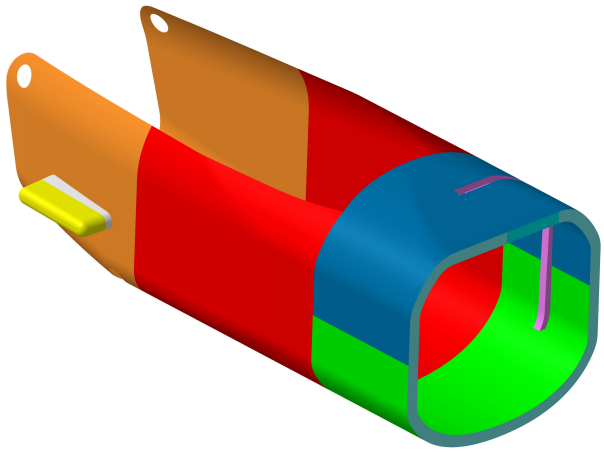

Figure 4.21: Visualization of different laminate zones with distinct colours for each part, highlighting the composite material arrangements on the rear part structure.

Table 4.21: Specification of composite material orientations, layer counts, and core total thickness for each laminate zone on the front part structure.

Part	Colour	Top Layer	Core Total Thickness [mm]	Bottom Layer
Former	Light Blue	$(0/90)_8$	-	-
Push Bar	Pink	$(0/90)_{15}$	-	-
Rear Part 1	Dark Blue	$(0/90)_5$	8	$(0/90)_4$
Rear Part 2	Green	$(0/90)_4$	6	$(0/90)_4$
Rear Part 3	Red	$(0/90)_4$	6	$(0/90)_4$
Rear Part 4	Orange	$(0/90)_{11}$	10	$(0/90)_{11}$
Rear Bumper Root	White	$(0/90)_{11}$	-	-
Rear Bumper Tip	Yellow	$(0/90)_5$	-	-

Firstly, the use of a Former had the purpose of maintaining the shape of the structure. Has seen in Subsection 4.2.2, the loads applied during the push-off phase, result in big structure deformations. The use of the Former allowed to increase the rigidity without big mass increases. Analyzing the laminate used in this part, it is the same as the one used in Front Part 2, but without the Aramid Honeycomb core. This fact allows for the Former to be a continuation of the laminate of this part. Regarding the geometry of the Former, various widths of the Former were tested to determine the optimal geometry. Ultimately, a width of 25 mm yielded the best results. Larger thicknesses were found to increase mass having little to no impact on the total deformation, making them less favorable.

Moving on to the analysis of the laminates used in Rear Part 2 and Rear Part 3, it is clear that they are the same. These laminates serve as the foundations for the ones used on the remaining fuselage structure, where there is an introduction of more plies and core material in order to withstand the loads applied, respecting the established limits of safety factors and deformations.

Bearing this in mind, Rear Part 1 uses a laminate based on the previous foundation, using another (0/90) ply and another 2 mm Aramid Honeycomb core layer. These extra layers allow for an enhancement of the structural integrity, in order to withstand the loads applied especially during the push-off phase in the push-bar connection.

Similarly, on the Rear Part 4, the foundation is reinforced with 14 (0/90) layers and 4 mm of Aramid Honeycomb core. This reinforcement is a consequence of the loads applied on the push handles in order to comply with the limits of deformation. During the structural development, this part of the structure was tested to be divided into two parts, but the results showed that this was not beneficial and would not yield better performance results, i.e., Total Mass and Natural Frequencies.

Regarding the Push Bar part, the laminate has the foundation of Rear Part 2 and Rear Part 3, without the Aramid core, reinforcing it accordingly. It is important to note that this reinforcement had the goal of increasing the structural rigidity of the bobsleigh, in a

similar way to the Former, to reduce the deformations and to increase the safety factors.

Finally, the rear bumpers have their structures divided into two parts: one closer to the root of the bumpers and one closer to the tip. This division has the goal of reducing the mass of the bumpers while respecting the established limits. The laminate used in the Rear Bumper Tip serves as the foundation for the laminate of the complete bumpers. On the Rear Bumper Root part, this foundation is reinforced in order to withstand the reduction of safety factors closer to the fuselage.

The use of the presented laminates is a result of the design process presented in Subsection 3.6. However, there are a couple of questions that arise from these results. On the one hand, in the final laminates only 0° and 90° plies were used. These laminate orientations might seem odd at first, but they are related to the geometry and loads at hand. Considering the main loads that are critical for the sizing of the structure are in a direction normal to the surface, these combinations of orientations of the laminates were the ones that yielded the biggest reduction of the amount of plies used.

On the other hand, when analyzing the different parts used in the final laminates, it is clear that these could be divided into more parts. However, this was not done as that did not yield better results. Considering the limiting factors on the rear part was the deformation, did not allow for a reduction of the Total Mass of the structure. On the front part, however, the limiting factor was the strength of the materials on the spar and the Natural Frequencies. With this in mind, it was not possible to reduce the number of plies used as that way it would not be possible to comply with the established limits.

Chapter 5

Conclusions and Future Work

5.1 Conclusion

From a global point of view, all the objectives proposed for this thesis were achieved, with the creation of the cowling structure for a competitive and high-performing vehicle for the sport of bobsleigh, through the use of FEA, bearing the accessibility limits at hand in mind. In order to achieve this goal, there was a need to divide this thesis into a series of meticulously planned sub-tasks.

To begin with, we initiated the process by researching the loads that act on a bobsleigh, how they affect the structure, and how they can be used in the structural development of the bobsleigh. This task was followed by the construction of a materials database, taking inspiration not only from the materials traditionally used in bobsleighs but also from those employed in similar sports. This foundation laid the groundwork for the subsequent phases of our research, as different materials affect the structure in different ways. In order to carry on with the structural development, there was a need to understand how the geometry could be tested using FEA. This led to a need for research on the boundary conditions available, and how these are simulated in *Ansys*.

Bearing all the attained knowledge in mind, the geometry obtained through CFD analysis was carried out into the FEA analysis, where all the different materials were tested and all the loads applied. The results obtained showed the influence different materials have on the final structure and how these can impact the performance of a bobsleigh. In order to be able to analyze the set of different results yielded, there was a need to resort to a comparison of the weighting methods. This comparison helped select three material combinations that yielded the best overall result on a preliminary geometry and helped select a final material combination on the final geometry.

On the preliminary geometry, the carbon fibers characterized by a lower Young's Modulus and higher strength had their structural development limited by the deformations. Being limited by its stiffness, resulted in oversized structures strength-wise. On the other hand, the carbon fiber tested with the higher Young's Modulus had its sizing limited by its strength. As a result, the use of this carbon fiber yielded oversized structures stiffness-wise. Therefore, they were not good options for the final structure, as they were not the most suited for the characteristics of geometry and loads applied. With regards to the core materials, it was clear that the ones that had the combination of stiffness and strength most suited to this case were Airex and Aramid Honeycomb. Finally, regarding the man-

ufacturing process, it was clear that different manufacturing processes had a major impact on performance results. Furthermore, these also presented a major impact on its accessibility, as more technologically advanced techniques require resources that might not be available. Therefore, in some cases is more beneficial to choose manufacturing processes that have easier accessibility at the expense of worse performance results. The material and manufacturing combination that was selected as the final one was the M35J/Aramid Honeycomb/Infusion combination.

These results were validated through investigation of mesh independence. To do so, the developed structure was tested using different meshes, and the results obtained were registered. When analyzing these results, it was seen that not all the results had converged and were limited by the computational power available. Therefore, these results have to be taken into consideration carefully, as they might not correspond to the reality.

5.2 Future Work

Considering the results and conclusions, as well as the issues found during the development of this thesis, it is clear that there is room for improvement, and further investigation to be done. The following topics highlight problems found and changes that might be implemented in further investigations in this area.

To begin with, regarding the structural development, it was clear that there was a computational power limitation. Therefore, in further research, it is clear that this is a problem to address, using computers with more computational power, allowing for finer meshes, so as to confirm the existence of mesh convergence in the results.

Secondly, it is clear that the changes in geometry, yield different structural characteristics. As a result, different geometries have different material combinations as the most suited ones. Therefore, it is important to note that in the final geometry, the final material combination might not be the best one. Thus, it is necessary, in further iterations, to carry out research similar to the one done on the preliminary geometry. Furthermore, if in the future more changes are made to the bobsleigh geometry, the structure development has to be carried out once again.

Thirdly, a major point that needs further investigation is the manufacturing process. This research should delve into the intricacies of the production methods, time consumption, available personnel, costs associated with the production methods, and quality control measures to ensure the efficient and cost-effective fabrication of the final bobsleigh cowling structure. This research would help to better structure the comparison of the weighting methods, retrieving more realistic results. These results could completely change the final manufacturing and material combinations, and help better understand the different material combinations.

Finally, in the current dissertation, apart from the Modal Analysis, only Static Structural Analysis were carried out. While these analyses are able to simulate quite well most real loading conditions scenarios, the loads applied in a real race are, in fact, dynamic in nature. Therefore, for future investigations, we recommend incorporating Dynamic Analyses, particularly when examining impact loads and high acceleration scenarios. In the context of impact loads, it is crucial to recognize that the application of loads in real-life racing scenarios is inherently dynamic, leading to higher internal loads and deformations than those predicted by static analyses. Consequently, incorporating dynamic analyses will provide a more accurate representation of the structural response under such conditions. Similarly, when considering high acceleration loads, the combined effects of accelerations during turns and vibrations can result in a more critical scenario than the one presented in this dissertation. Therefore, a comprehensive analysis involving Dynamic Analyses is recommended to investigate the complex interactions from these dynamic loading conditions.

Bibliography

[1] F. Braghin, F. Cheli, M. Donzelli, S. Melzi, and E. Sabbioni, "Multi-body model of a bobsleigh: comparison with experimental data," *Multibody System Dynamics*, vol. 25, no. 2, pp. 185–201, aug 2010. doi: 10.1007/s11044-010-9218-7 1, 4

[2] L. Poirier, "Ice Friction in the Sport of Bobsleigh," Ph.D. thesis, 01 2011. 1, 2, 3, 4

[3] E. Sabbioni, S. Melzi, F. Cheli, and F. Braghin, "Bobsleigh and Skeleton," in *The Engineering Approach to Winter Sports*. Springer New York, 2016, pp. 183–276. 1, 14, 15

[4] IBSF, "International Bobsleigh Rules 2022," September 2022, (available at https://www.ibsf.org). 1, 2, 3, 20, 26

[5] ——, "IBSF Track Rules 2019," October 2019, (available at https://www.ibsf.org). 1

[6] P. Dabnichki, "Bobsleigh performance characteristics for winning design," *Procedia Engineering*, vol. 112, pp. 436–442, 2015. doi: 10.1016/j.proeng.2015.07.221 1, 3, 4, 15, 16, 30, 31

[7] C. Hainzlmaier, "A new tribologically optimized bobsleigh runner," Ph.D. thesis, Technische Universität München, 2005. 2, 4, 19

[8] S. Leithwood, "Dual-sport brock athlete named to national bobsleigh team," Dec 2020. [Online]. Available: https://brocku.ca/brock-news/2020/12/dual-sport-brock-athlete-named-to-national-bobsleigh-team/ 2

[9] H.-S. Shim, Y.-N. Lee, and K.-Y. Kim, "Optimization of bobsleigh bumper shape to reduce aerodynamic drag," *Journal of Wind Engineering and Industrial Aerodynamics*, vol. 164, pp. 108–118, may 2017. doi: 10.1016/j.jweia.2017.02.012 2, 4, 19

[10] A. R. Nunes, "A participação de Portugal nos Jogos Olímpicos: De 1912 às perspetivas para 2012," in *Congresso de História e Desporto. Olimpismo 2012: Universidade Nova de Lisboa 31 de maio 1 de junho 2012*. Grupo História e Desporto, 2012, pp. 157–163. 3

[11] I. O. Comittee, "Calgary 1988 Four-man Men Results - Olympic Bobsleigh." [Online]. Available: https://olympics.com/en/olympic-games/calgary-1988/results/bobsleigh/four-man-men 3

[12] ——, "Calgary 1988 Two-man Men Results - Olympic Bobsleigh." [Online]. Available: https://olympics.com/en/olympic-games/calgary-1988/results/bobsleigh/two-man-men 3

[13] F. Motallebi, P. Dabnichki, and D. Luck, "Advanced bobsleigh design. Part 2: Aerodynamic modifications to a two-man bobsleigh," *Proceedings of the Institution of*

Mechanical Engineers, Part L: Journal of Materials: Design and Applications, vol. 218, no. 2, pp. 139–144, apr 2004. doi: 10.1177/146442070421800207 4

[14] P. Dabnichki and E. Avital, "Influence of the postion of crew members on aerodynamics performance of two-man bobsleigh," *Journal of Biomechanics*, vol. 39, no. 15, pp. 2733–2742, jan 2006. doi: 10.1016/j.jbiomech.2005.10.011 4

[15] H. H. Ubbens, R. P. Dwight, A. Sciacchitano, and N. Timmer, "Some results on bobsleigh aerodynamics," *Procedia Engineering*, vol. 147, pp. 92–97, 2016. doi: 10.1016/j.proeng.2016.06.195 4, 24

[16] M. Dumm, C. Hainzlmaier, S. Boerboom, and E. Wintermantel, "The effect of pressure on friction of steel and ice and implementation to bobsleigh runners," in *The Engineering of Sport 6*. Springer New York, 2006, pp. 103–106. 4

[17] B. A. Marmo, J. R. Blackford, and C. E. Jeffree, "Ice friction, wear features and their dependence on sliding velocity and temperature," *Journal of Glaciology*, vol. 51, no. 174, pp. 391–398, 2005. doi: 10.3189/172756505781829304 4

[18] L. Poirier, E. P. Lozowski, S. Maw, D. J. Stefanyshyn, and R. I. Thompson, "Experimental analysis of ice friction in the sport of bobsleigh," *Sports Engineering*, vol. 14, no. 2-4, pp. 67–72, nov 2011. doi: 10.1007/s12283-011-0077-0 4

[19] M. Scherge, R. Böttcher, A. Spagni, and D. Marchetto, "High-speed measurements of steel–ice friction: Experiment vs. calculation," *Lubricants*, vol. 6, no. 1, p. 26, mar 2018. doi: 10.3390/lubricants6010026 4

[20] M. F. Zaeh and P. Gebhard, "Manufacturing of bobsled runners," in *The Engineering of Sport 6*. Springer New York, 2006, pp. 119–122. 4

[21] M. Vasconcelos, "Estudo Aerodinâmico Preliminar de um Bobsled de 2 Lugares," mathesis, Universidade da Beira Interior, 2023. 4, 23

[22] J. von Schleinitz, L. Wörle, M. Graf, and A. Schröder, "Modeling ice friction for vehicle dynamics of a bobsled with application in driver evaluation and driving simulation," *Tribology International*, vol. 165, p. 107344, Oct. 2021. doi: 10.1016/j.triboint.2021.107344 7, 8, 32

[23] F. Braghin, M. Donzelli, S. Melzi, and E. Sabbioni, "A driver model of a two-man bobsleigh," *Sports Engineering*, vol. 13, no. 4, pp. 181–193, jun 2011. doi: 10.1007/s12283-011-0066-3 8, 9

[24] F. Braghin, F. Cheli, S. Melzi, and E. Sabbioni, "Experimental assessment of bobsleigh dynamics and ice-skate contact forces," in *Topics in Modal Analysis II, Volume 6: Proceedings of the 30th IMAC, A Conference on Structural Dynamics, 2012*. Springer, 2012. doi: https://doi.org/10.1007/978-1-4614-2419-2_50 pp. 487–498. 9, 10, 11, 30, 31

[25] S. Lee, T. Kim, S. Lee, S. Kil, and S. Hong, "Development of force measurement system of bobsled for practice of push-off phase," *Proceedings of the Institution of Mechanical Engineers, Part P: Journal of Sports Engineering and Technology*, vol. 229, no. 3, pp. 192–198, jan 2015. doi: 10.1177/1754337114565383 11, 12, 33

[26] F. Onasch, A. Sawatsky, A. Stano, and W. Herzog, "Development of the instrumentation of a 4-man bobsled," *Journal of Biomechanics*, vol. 152, p. 111578, may 2023. doi: 10.1016/j.jbiomech.2023.111578 12, 13, 26, 33

[27] P. Dabnichki, F. Motallebi, and E. Avital, "Advanced bobsleigh design. part 1: Body protection, injury prevention and performance improvement," *Proceedings of the Institution of Mechanical Engineers, Part L: Journal of Materials: Design and Applications*, vol. 218, no. 2, pp. 129–137, apr 2004. doi: 10.1177/146442070421800206 13

[28] Лубяко, А. А., Русия, А. Г., Соловьева, Е. М., and Толстов, Ю. С., "Вибрационная нагрузка в скоростных видах зимнего спорта (скоростной спуск, ски-кросс, бобслей) [Vibration Loading In High-Speed Winter Sports (Alpine Skiing, Ski-Cross, Bobsled)]," *Russia: Медицина экстремальных ситуаций*, no. 2 (52), pp. 44–51, 2015. 14, 30, 31

[29] M. Kamble, T. Shakfeh, R. Moheimani, and H. Dalir, "Optimization of a Composite Monocoque Chassis for Structural Performance: A Comprehensive Approach," *Journal of Failure Analysis and Prevention*, vol. 19, no. 5, pp. 1252–1263, sep 2019. doi: 10.1007/s11668-019-00711-0 17, 18

[30] R. N. Singh, S. Rudraksh, and M. Sachidhanandam, "Design, development and analysis of a three-wheeler vehicle chassis," *International Journal of Vehicle Structures and Systems*, vol. 14, no. 1, jan 2022. doi: 10.4273/ijvss.14.1.13 18

[31] F. Eimon, M. Gonzalez, M. Kramarz, N. Powell, and K. Ziemann, "Carbon Fiber Monocoque Chassis Platform for Formula SAE and Formula SAE Electric Race Cars," 2017. 18

[32] L. Robinson, "Advanced materials are a game changer in the winter olympics," *JOM*, vol. 62, no. 2, pp. 17–19, feb 2010. doi: 10.1007/s11837-010-0024-8 19

[33] B. Rizk, H. Brat, and T. Pirrello, "Injuries in Skating and Sledding Winter Sports: Patterns and Imaging Findings," *Seminars in Musculoskeletal Radiology*, vol. 26, no. 01, pp. 082–090, feb 2022. doi: 10.1055/s-0041-1731421 19

[34] R. K. Guduru and A. A. Gupta, "Consumer Applications of Graphene and Its Composites," in *Handbook of Consumer Nanoproducts*. Springer Nature Singapore, 2022, pp. 471–500. 19

[35] O. Aluko, S. Gowtham, and G. Odegard, "Multiscale modeling and analysis of graphene nanoplatelet/carbon fiber/epoxy hybrid composite," *Composites Part B:*

Engineering, vol. 131, pp. 82–90, dec 2017. doi: 10.1016/j.compositesb.2017.07.075 19

[36] A. K. Pathak, M. Borah, A. Gupta, T. Yokozeki, and S. R. Dhakate, "Improved mechanical properties of carbon fiber/graphene oxide-epoxy hybrid composites," *Composites Science and Technology*, vol. 135, pp. 28–38, oct 2016. doi: 10.1016/j.compscitech.2016.09.007 19

[37] X. Zhang, X. Fan, C. Yan, H. Li, Y. Zhu, X. Li, and L. Yu, "Interfacial Microstructure and Properties of Carbon Fiber Composites Modified with Graphene Oxide," *ACS Applied Materials & Interfaces*, vol. 4, no. 3, pp. 1543–1552, mar 2012. doi: 10.1021/am201757v 19

[38] L. Gong, F. Zhang, X. Peng, F. Scarpa, Z. Huang, G. Tao, H. Liu, H. Zhou, and H. Zhou, "Improving the damping properties of carbon fiber reinforced polymer composites by interfacial sliding of oriented multilayer graphene oxide," *Composites Science and Technology*, vol. 224, p. 109309, jun 2022. doi: 10.1016/j.compscitech.2022.109309 20

[39] H. Taş and I. F. Soykok, "Effects of carbon nanotube inclusion into the carbon fiber reinforced laminated composites on flexural stiffness: A numerical and theoretical study," *Composites Part B: Engineering*, vol. 159, pp. 44–52, feb 2019. doi: 10.1016/j.compositesb.2018.09.055 20

[40] S. U. Khan, C. Y. Li, N. A. Siddiqui, and J.-K. Kim, "Vibration damping characteristics of carbon fiber-reinforced composites containing multi-walled carbon nanotubes," *Composites Science and Technology*, vol. 71, no. 12, pp. 1486–1494, aug 2011. doi: 10.1016/j.compscitech.2011.03.022 20

[41] K. J. Kim, J. Kim, W. R. Yu, J. H. Youk, and J. Lee, "Improved tensile strength of carbon fibers undergoing catalytic growth of carbon nanotubes on their surface," *Carbon*, vol. 54, pp. 258–267, apr 2013. doi: 10.1016/j.carbon.2012.11.037 20

[42] G. Lee, M. Sung, J. H. Youk, J. Lee, and W.-R. Yu, "Improved tensile strength of carbon nanotube-grafted carbon fiber reinforced composites," *Composite Structures*, vol. 220, pp. 580–591, jul 2019. doi: 10.1016/j.compstruct.2019.04.037 20

[43] Toray, "T700s – standard modulus carbon fiber." [Online]. Available: https://www.toraycma.com/wp-content/uploads/T700S-Technical-Data-Sheet-1.pdf.pdf 27

[44] Hexcel, "Hexcel | composite materials and structures." [Online]. Available: https://www.hexcel.com/user_area/content_media/raw/HexPly_M47_eu_DataSheet.pdf 27

[45] Toray, "T1100g – intermediate modulus carbon fiber." [Online]. Available: https://www.toraycma.com/wp-content/uploads/T1100G-Technical-Data-Sheet-1.pdf.pdf 27

[46] ——, “M35j – high modulus carbon fiber.” [Online]. Available: https://www.toraycma.com/wp-content/uploads/M35J-Technical-Data-Sheet-1.pdf.pdf 27

[47] ——, “M60j – high modulus carbon fiber.” [Online]. Available: https://www.toraycma.com/wp-content/uploads/M60J-Technical-Data-Sheet-1.pdf.pdf 27

[48] A. C. Materials, “Airex - universal structural foam data sheet.” [Online]. Available: https://www.3accorematerials.com/uploads/documents/TDS-AIREX-C70-E_1106.pdf 27

[49] Media Easy Composites.eu, “Product information - rohacell® ig-f.” [Online]. Available: https://media.easycomposites.eu/datasheets/Rohacell-IG-F-TDS.pdf 27

[50] E. Industries, Jun 2022. [Online]. Available: https://performance-foams.evonik.com/en/products-and-solutions/rohacell/rohacell-ig-f-170038.html 27

[51] Gurit, “Gurit: Product overview - core materials.” [Online]. Available: https://gurit.com/wp-content/uploads/2022/11/Core_brochure-2.pdf 27

[52] ——, “Gurit pvc: Structural foam core.” [Online]. Available: https://www.gurit.com/wp-content/uploads/2023/06/PDS-GURIT-PVC-13-0623.pdf 27

[53] East Coast Fiberglass Supplies, “Cormaster c2: High performance lightweight material from schÜtz for industrial applications.” 27

[54] ANSYS, “ACP User’s Guide 2021 R2,” Jul 2021. 37, 38, 39

[55] P. Isaksson, A. Krusper, and P. Gradin, “Shear correction factors for corrugated core structures,” *Composite Structures*, vol. 80, no. 1, pp. 123–130, sep 2007. doi: 10.1016/j.compstruct.2006.04.066 37

[56] A. T. Nettles, “Basic Mechanics of Laminated Composite Plates,” *NASA. Marshall Space Flight Center*, Oct. 1994. 37, 38, 39

[57] ANSYS, “SHELL 181,” Jul 2017. [Online]. Available: https://www.mm.bme.hu/~gyebro/files/ans_help_v182/ans_elem/Hlp_E_SHELL181.html 40

[58] ——, “Mechanical User’s Guide 2021 R2,” Jul 2021. 40, 41, 42

[59] G. Eckold, *Manufacture*. Elsevier, 1994, pp. 251–304. 45

[60] M. Gupta, A. Jain, J. N. Kamineni, and R. G. Burela, *Advances and applications of biofiber-based polymer composites*. Elsevier, 2022, pp. 575–602. 45

[61] M. Afendi, W. Banks, and D. Kirkwood, “Bubble free resin for infusion process,” *Composites Part A: Applied Science and Manufacturing*, vol. 36, no. 6, pp. 739–746, Jun. 2005. doi: 10.1016/j.compositesa.2004.10.030 45

[62] W. Syed, “Ansys Mesh Metrics Explained,” Nov 2022. [Online]. Available: https://featips.com/2022/11/21/ansys-mesh-metrics-explained/ 73